AMORPHOUS METAL OXIDE THIN FILMS FROM AQUEOUS PRECURSORS: NEW ROUTES TO HIGH-*K* DIELECTRICS, IMPACT OF ANNEALING ATMOSPHERE HUMIDITY, AND ELUCIDATION OF NON-UNIFORM COMPOSITION PROFILES

by

KEENAN N. WOODS

A DISSERTATION

Presented to the Department of Chemistry and Biochemistry
and the Graduate School of the University of Oregon
in partial fulfillment of the requirements
for the degree of
Doctor of Philosophy

December 2017

DISSERTATION APPROVAL PAGE

Student: Keenan N. Woods

Title: Amorphous Metal Oxide Thin Films from Aqueous Precursors: New Routes to High-κ Dielectrics, Impact of Annealing Atmosphere Humidity, and Elucidation of Non-uniform Composition Profiles

This dissertation has been accepted and approved in partial fulfillment of the requirements for the Doctor of Philosophy degree in the Department of Chemistry and Biochemistry by:

Shannon W. Boettcher Chairperson
Catherine J. Page Advisor
James E. Hutchison Core Member
Benjamin J. McMorran Institutional Representative

and

Sara D. Hodges Interim Vice Provost and Dean of the Graduate School

Original approval signatures are on file with the University of Oregon Graduate School.

Degree awarded December 2017

© 2017 Keenan N. Woods

DISSERTATION ABSTRACT

Keenan N. Woods

Doctor of Philosophy

Department of Chemistry and Biochemistry

December 2017

Title: Amorphous Metal Oxide Thin Films from Aqueous Precursors: New Routes to High-κ Dielectrics, Impact of Annealing Atmosphere Humidity, and Non-uniform Composition Profiles

Metal oxide thin films serve as critical components in many modern technologies, including microelectronic devices. Industrial state-of-the-art production utilizes vapor-phase techniques to make high-quality (dense, smooth, uniform) thin film materials. However, vapor-phase techniques require large energy inputs and expensive equipment and precursors. Solution-phase routes to metal oxides have attracted great interest as cost-effective alternatives to vapor-phase methods and also offer the potential of large-area coverage, facile control of metal composition, and low-temperature processing.

Solution deposition has previously been dominated by sol-gel routes, which utilize organic ligands, additives, and/or solvents. However, sol-gel films are often porous and contain residual carbon impurities, which can negatively impact device properties. All-inorganic aqueous routes produce dense, ultrasmooth films without carbon impurities, but the mechanisms involved in converting aqueous precursors to metal oxides are virtually unexplored. Understanding these mechanisms and the parameters that influence them is critical for widespread use of aqueous approaches to prepare microelectronic components. Additionally, understanding (and controlling) density and composition inhomogeneities is

important for optimizing electronic properties. An overview of deposition approaches and the challenges facing aqueous routes are presented in Chapter I. A summary of thin film characterization techniques central to this work is given in Chapter II.

This dissertation contributes to the field of solution-phase deposition by focusing on three areas. First, an all-inorganic aqueous route to high-κ metal oxide dielectrics is developed for two ternary systems. Chapters III and IV detail the film formation chemistry and film properties of lanthanum zirconium oxide (LZO) and zirconium aluminum oxide (ZAO), respectively. The functionality of these dielectrics as device components is also demonstrated. Second, the impact of steam annealing on the evolution of aqueous-derived films is reported. Chapter V demonstrates that steam annealing lowers processing temperatures by effectively reducing residual counterion content, improving film stability with respect to water absorption, and enhancing dielectric properties of LZO films. Third, density and composition inhomogeneities in aqueous-derived films are investigated. Chapters VI and VII examine density inhomogeneities in single- and multi-metal component thin films, respectively, and show that these density inhomogeneities are related to inhomogeneous metal component distributions.

This dissertation includes previously published coauthored material.

CURRICULUM VITAE

NAME OF AUTHOR: Keenan N. Woods

GRADUATE AND UNDERGRADUATE SCHOOLS ATTENDED:

University of Oregon, Eugene, OR
California Lutheran University, Thousand Oaks, CA

DEGREES AWARDED:

Doctor of Philosophy, Chemistry, 2017, University of Oregon
Master of Science, Chemistry, 2015, University of Oregon
Bachelor of Science, Chemistry, 2013, California Lutheran University

AREAS OF SPECIAL INTEREST:

Materials Chemistry

PROFESSIONAL EXPERIENCE:

Research Assistant, Page Research Group, University of Oregon, 2013-2017

Research Assistant, Tannaci Research Group, California Lutheran University, 2009-2013

GRANTS, AWARDS, AND HONORS:

Informal Science Education Fellowship, University of Oregon, 2016, 2015, and 2014

National Science Foundation Scholar, American Chemical Society Green Chemistry Institute, 2015

Graduate Research Fellowship Program Honorable Mention, National Science Foundation, 2015

Science Communication Fellowship, Oregon Museum of Science and Industry, 2014

CFS Science Scholarship, California Lutheran University, 2012

Academic Excellence Award, California Lutheran University, 2012 and 2011

Swenson Summer Research Fellowship, California Lutheran University, 2011 and 2010

Presidential Scholarship, California Lutheran University, 2009

PUBLICATIONS:

Woods, K. N.; Hamann, D. M.; Page, C. J. "Composition-Property Relationships in High-κ $La_xZr_{1-x}O_y$ Thin Films from Aqueous Solution." *Solid State Sci.* Under review.

Woods, K. N.; Thomas, M. C.; Mitchson, G.; Ditto, J.; Xu, C.; Kayal, D.; Frisella, K. C.; Gustafsson, T.; Garfunkel, E.; Chabal, Y. J.; Johnson, D. C.; Page, C. J. "Nonuniform Composition Profiles in Amorphous Multimetal Oxide Thin Films Deposited from Aqueous Solution." *ACS Appl. Mater. Interfaces*. **2017**, *9*, 37476-37483.

Woods, K. N.*; Plassmeyer, P. N.* Park, D.-H.; Enman, L. J.; Grealish, A. K.; Kirk, B. L.; Boettcher, S. W.; Keszler, D. A.; Page, C. J. "Low-Temperature Steam Annealing of Metal Oxide Thin Films from Aqueous Precursors: Enhanced Counterion Removal and Improved Resistance to Water Absorption." *Chem. Mater.* **2017**, *29*, 8531-8538.

Woods, K. N.; Waddington, E. C.; Crump, C. A.; Bryan, E. A.; Gleckler, T. S.; Nellist, M. R.; Duell, B. A.; Nguyen, D. P.; Boettcher, S. W.; Page, C. J. "Tunable High-κ $Zr_xAl_{1-x}O_y$ Thin Film Dielectrics from All-Inorganic Aqueous Precursor Solutions." *RSC Adv.* **2017**, *7*, 39147-39152.

Plassmeyer, P. N.; Mitchson, G.; Woods, K. N.; Johnson, D. C.; Page, C. J. "Impact of Relative Humidity during Spin-Deposition of Metal Oxide Thin Films from Aqueous Solution Precursors." *Chem. Mater.* **2017**, *29*, 2921-2926.

Wood, S. R.; Woods, K. N.; Plassmeyer, P. N.; Marsh, D. A.; Johnson, D. W.; Page, C. J.; Jensen, K. M. Ø.; Johnson, D. C. "Same Precursor, Two Different Products: Comparing the Structural Evolution of In-Ga-O "Gel-Derived" Powders and Solution-Cast Films Using Pair Distribution Function Analysis." *J. Am. Chem. Soc.* **2017**, *139*, 5607-5613.

Woods, K. N.; Chiang, T.-H.; Plassmeyer, P. N.; Kast, M. G.; Lygo, A. C.; Grealish, A. K.; Boettcher, S. W.; Page, C. J. "High-κ Lanthanum Zirconium Oxide Thin Film Dielectrics from Aqueous Solution Precursors." *ACS Appl. Mater. Interfaces.* **2017**, *9*, 10897-10903.

Mitchson, G.; Ditto, J.; Woods, K. N.; Westover, R.; Page, C. J.; Johnson, D. C. "HAADF STEM Signal Intensity Analysis Method for Extracting Structural Information from Complex Thin Films." *Semicond. Sci. Tech.* **2016**, *31*, 084003

Norelli, K. M.; Plassmeyer, P. N.; Woods, K. N.; Glassy, B. A.; Knutson, C. C.; Beekman, M.; Page, C. J. "Influence of Composition and Processing Parameters on the Properties of Solution-Processed Aluminum Phosphate Oxide (AlPO) Thin Films." *Solid State Sci.* **2016**, *55*, 8-12.

Fairley, K. C.; Merrill, D. R.; Woods, K. N.; Ditto, J.; Xu, C.; Oleksak, R. P.; Gustafsson, T.; Johnson, D. W.; Garfunkel, E. L.; Herman, G. S.; Johnson, D. C.; Page, C. J. "Non-uniform Composition Profiles in Inorganic Thin Films from Aqueous Solutions." *ACS Appl. Mater. Interfaces.* **2016**, *8*, 667-672.

ACKNOWLEDGMENTS

I am deeply grateful to the University of Oregon and the Center for Sustainable Materials Chemistry (CSMC) for funding during the course of my graduate studies. I thank the staff of the Center for Advanced Materials Characterization in Oregon (CAMCOR) for use of instrumentation facilities and for their frequent assistance. I also thank the Department of Chemistry & Biochemistry and my committee members (Shannon W. Boettcher, James E. Hutchison, and Benjamin J. McMorran) for wonderful discussions, a welcoming environment, and general support. I especially thank my advisor, Catherine J. Page, for her mentorship and friendship.

I would be remiss if I did not also thank the many collaborators and colleagues who helped make this work possible. This list of graduate students, professors, and high school and undergraduate mentees is a long one, and I express my deepest gratitude to you all. In particular, I would like to thank Paul N. Plassmeyer and Matthew G. Kast for their advice, laughter, and "scientific discussions."

Words cannot express my appreciation to my family for all of their support, guidance, and love. Each of you has influenced me in some way, and I am a better man for it. Thank you for believing in me and for making life worth living. I especially thank the love of my life, Jacklyn R. Whitehead, for all of her love, encouragement, and positivity that inspired me and helped me make it across the finish line.

To my family

TABLE OF CONTENTS

Chapter Page

I. INTRODUCTION 1

Metal Oxide Properties and Applications 1

Thin Film Deposition Approaches 1

Vapor-phase Deposition Methods 1

Solution-phase Deposition Methods 2

Challenges in Solution-phase Deposition 3

Addressing Challenges in Solution-phase Deposition: This Work 5

Authorship Statement 6

Bridge 7

II. THIN FILM CHARACTERIZATION 8

Challenges in Thin Film Analysis 8

Physical Characterization 8

Chemical Analysis 12

Electrical Characterization 14

Bridge 16

III. HIGH-κ LANTHANUM ZIRCONIUM OXIDE THIN FILM DIELECTRICS FROM AQUEOUS SOLUTION PRECURSORS 17

Authorship Statement 17

Introduction 17

Experimental 19

Precursor Solution Preparation 19

Chapter Page

Thin Film Preparation 19

Precursor Solution Characterization 20

Thin Film Characterization 20

Device Fabrication and Testing 21

Results and Discussion 22

Conclusion 30

Bridge 30

IV. TUNABLE HIGH-κ $Zr_xAl_{1-x}O_y$ THIN FILM DIELECTRICS FROM ALL-INORGANIC AQUEOUS SOLUTION PRECURSORS 32

Authorship Statement 32

Introduction 32

Experimental 34

Precursor Solution Preparation 34

Thin Film Preparation 34

Precursor Solution Characterization 35

Thin Film Characterization 36

Device Fabrication and Testing 36

Results and Discussion 37

Conclusion 45

Bridge 45

V. LOW-TEMPERATURE STEAM ANNEALING OF METAL OXIDE THIN FILMS FROM AQUEOUS PRECURSORS: ENHANCED COUNTERION REMOVAL, RESISTANCE TO WATER ABSORPTION, AND DIELECTRIC CONSTANT 47

Chapter Page

Authorship Statement 47

Introduction 47

Experimental 49

Precursor Solution Preparation 49

Thin Film Preparation 50

Thin Film Characterization 51

Device Fabrication and Testing 52

Results and Discussion 53

Impact of Steam Annealing on Bulk Chemistry 53

Impact of Steam Annealing on Water Absorption 57

Impact of Steam Annealing on Morphology 61

Impact of Steam Annealing on Device Properties 64

Conclusion 65

Bridge 66

VI. NON-UNIFORM COMPOSITION PROFILES IN INORGANIC THIN FILMS FROM AQUEOUS SOLUTIONS 68

Authorship Statement 68

Introduction 68

Experimental 71

$InGaO_x$ and AlO_x Precursor Solution Preparation 71

$Hf(OH)_{4-2x-2y}(O_2)_x(SO_4)_y \bullet zH_2O$ (HafSOx) Precursor Solution Preparation 72

$InGaO_x$, AlO_x, and HafSOx Film Preparation 72

Chapter Page

Thin Film Characterization ... 73

Results and Discussion ... 74

Conclusion ... 84

Bridge ... 85

VII. NON-UNIFORM COMPOSITION PROFILES IN AMORPHOUS MULTI-METAL OXIDE THIN FILMS DEPOSITED FROM AQUEOUS SOLUTION ... 86

Authorship Statement ... 86

Introduction ... 86

Experimental ... 88

Precursor Solution Preparation ... 88

Thin Film Preparation ... 89

Thin Film Characterization ... 89

Device Fabrication and Testing ... 91

Results and Discussion ... 92

Conclusion ... 99

VIII. SUMMARY AND OUTLOOK ... 101

APPENDICES ... 103

A. CHAPTER III SUPPLEMENTARY INFORMATION ... 103

B. CHAPTER IV SUPPLEMENTARY INFORMATION ... 106

C. CHAPTER V SUPPLEMENTARY INFORMATION ... 110

D. CHAPTER VII SUPPLEMENTARY INFORMATION ... 125

REFERENCES CITED ... 134

LIST OF FIGURES

Figure Page

2.1. Simulated XRR patterns for films of various composition and thickness on a Si substrate generated using Bede REFS modeling software 9

3.1. TGA of $La(NO_3)_3 \cdot xH_2O$, $ZrO(NO_3)_2 \cdot xH_2O$, and LZO precursor powders derived from drying 1.0 M solutions 23

3.2. FTIR spectra of LZO films annealed between 200 and 600 °C 24

3.3. GIXRD of LZO films annealed between 300 and 1100 °C 25

3.4. (a) XRR patterns of LZO films annealed between 300 and 600 °C and best-fit models. A cartoon inset depicts the two-layer model necessary for generating good fits to the data. (b) Total thickness and total density extracted from best-fit models of XRR data in panel (a)................................ 26

3.5. (a) Representative AFM images of a 500 nm^2 area and (b) comparison of surface roughness determined by XRR and AFM for LZO films annealed between 300 and 600 °C 27

3.6. Cross-sectional SEM images of two-coat LZO films annealed at temperatures between 300 and 600 °C 28

3.7. (a) Dielectric constants and loss tangents, and (b) *J-E* data for MIS devices made from two-coat (~100 nm) LZO films 29

4.1. (a) Mass loss percent and (b) derivative of mass loss as a function of annealing temperature for bulk ZAO precursor powders 38

4.2. FTIR spectra of two-coat ZAO films annealed at (a) 200 °C and (b) 500 °C.. 39

4.3. GIXRD of single-coat ZAO films annealed at (a) 500 °C and (b) 600 °C........... 40

4.4. Representative AFM images of single-coat (a) AlO_y, (b) $Zr_{0.25}Al_{0.75}O_y$, (c) $Zr_{0.50}Al_{0.50}O_y$, (d) $Zr_{0.75}Al_{0.25}O_y$, (e) $Zr_{0.90}Al_{0.10}O_y$, and (f) ZrO_y films annealed at 500 °C and (g) corresponding surface roughness values.............. 41

4.5. SEM cross-sectional images of two-coat (a) ZrO_y, (b) $Zr_{0.75}Al_{0.25}O_y$, (c) $Zr_{0.25}Al_{0.75}O_y$, and (d) AlO_y films annealed at 500 °C............................... 42

4.6. (a) Dielectric constants measured at 1 kHz and (b) corresponding loss tangents for MIS devices fabricated from two-coat (~100 nm) ZAO films annealed at various temperatures 43

4.7. Representative *JE* data for MIS devices made from two-coat ZAO films (~100 nm) annealed at 500 °C 44

5.1. FTIR spectra of LZO films deposited from 1.8 M solutions derived from (a) NO_3^- precursors or (b) NO_3^-/Cl^- precursors. All films were annealed under humid or dry conditions at 200 °C 53

5.2. TPD data for dry- and humid-annealed LZO films deposited from a 1.5 M solution (NO_3^-/Cl^- precursors) and annealed at 200 °C prior to TPD experiments: (a) m/z 35, (c) m/z 30, and (d) m/z 32 55

5.3. FTIR spectra of LZO films deposited from a 1.8 M solution (NO_3^-/Cl^- precursors) and annealed under dry or humid conditions at 200 °C. Solid lines are data taken immediately after annealing and dashed lines are data taken after 1 h in ambient lab air (~45% relative humidity) 58

5.4. XPS spectra of films deposited from a 1.0 M solution (NO_3^-/Cl^- precursors) and annealed under dry or humid conditions at 500 °C 60

5.5. SEM images of LZO films deposited from a 1.5 M solution (NO_3^-/Cl^- precursors) and annealed at 500 °C under (a) dry or (b) humid conditions 62

5.6. SEM images of LZO films deposited from (a) 0.5, (b) 1.0, or (c) 1.5 M solutions annealed using a standard (25 °C min^{-1}) ramp, and LZO films deposited from a 1.5 M solution and annealed using (d) slow (0.25 °C min^{-1}), (e) standard, or (f) fast (125 °C min^{-1}) ramps. All films were deposited from NO_3^-/Cl^- precursors and annealed under dry conditions at 500 °C 63

5.7. (a) Dielectric constants and loss tangents for MIS devices made from two-coat LZO (NO_3^-, 1.0 M) films (~100 nm) annealed at various temperatures under dry or humid conditions 65

6.1. XRR patterns of four-coat films of InGaO*x*, AlO*x*, and HafSOx without peroxide 75

6.2. (a) A schematic representation of two simple structures of a four-coat stack, one in which each coat is homogeneous and one where each coat has the identical inhomogeneous electron density. (b) Simulated XRR data for the two cases shown in panel (a) 76

Figure Page

6.3. Raw and modeled XRR data of a four-coat multilayer of HafSOx without peroxide annealed at 180 °C for 1 min 77

6.4. XRR data for a single-coat HafSOx film without peroxide annealed at 180 °C for 1 min 78

6.5. XRR data for a single-coat HafSOx film containing peroxide annealed at 80 °C for 1 min 80

6.6. (a) HAADF-STEM image of the cryo-FIB cross-section of a single-layer HafSOx film containing peroxide annealed at 80 °C for 1 min and (b) the heavy atom density profile of the film obtained by integrating the intensity of the pixels in the boxed region in panel (a) 81

6.7. (a) MEIS data collected on a HafSOx film containing peroxide annealed for 3 min at 80 °C, 5 min at 150 °C, and 5 min at 300 °C. (b) An expansion of the Hf area 83

7.1. XRR patterns of four, three, two, and one layer LZO films deposited from 0.25, 0.33, 0.50, and 1.00 M precursor solutions, respectively 93

7.2. HAADF-STEM images of one (a), two (b), three (c), and four (d) layer LZO films deposited from 1.00, 0.50, 0.33, and 0.25 M precursor solutions, respectively 94

7.3. La:Zr atomic ratio as a function of distance from the film surface for a three layer film deposited from a 0.33 M precursor solution as determined by STEM-EDS elemental mapping 96

7.4. (a) C 1s and (b) O 1s XPS spectra of a single-layer LZO film annealed under vacuum and (c) C 1s and (d) O 1s XPS spectra of a LZO film annealed in air for various Ar^+ sputtering times 97

7.5. (a) Dielectric constants and (b) loss tangent as a function of frequency for MIS devices made from four, three, two, and one layer LZO films deposited from 0.25, 0.33, 0.50, and 1.00 M precursor solutions, respectively 98

AA1. a) Dielectric constant as a function of frequency for LZO MIS devices and b) corresponding loss tangents 104

AA2. *J-E* hysteresis test for a MIS device made from a two-coat (~100 nm) LZO film annealed at 500 °C 105

Figure Page

AB1. FTIR spectra of two-coat ZAO films annealed at (a) 300 °C and (b) 400 °C 106

AB2. Representative XRR spectra for single-coat ZAO films annealed at 500 °C and overlaid best fit models 107

AB3. (a) Film thickness and (b) density of single-coat ZAO films extracted from XRR best fit, two-layer models 108

AB4. (a) Dielectric constants as a function of frequency for ZAO-based MIS devices and (b) corresponding loss tangents 109

AC1. FTIR spectra of (a) ZnO, (b) YAO, and (c) LZO films deposited from 1.8 M aqueous nitrate precursors and annealed under dry or humid conditions at various temperatures 111

AC2. Photographs of LZO films deposited from a 1.0 M solution (NO_3^-/Cl^- precursors) and annealed under dry or humid conditions at 200 °C. Films were photographed immediately after annealing (0 h) and then after 1, 2, and 72 h of exposure to ambient air. 112

AC3. Representative AFM images (1 X 1 μm^2) taken of LZO films deposited from a 1.0 M solution (NO_3^- precursors). Films were annealed at (a) 200 °C under dry conditions, (b) 200 °C under humid conditions, (c) 500 °C under dry conditions, and (d) 500 °C under humid conditions 113

AC4. FTIR spectra of LZO films deposited from a 1.8 M solution (NO_3^- precursors) and annealed under dry or humid conditions at 200 °C. Solid lines are data taken immediately after annealing and dashed lines are data taken after 1 h in ambient lab air (~45% relative humidity) 114

AC5. XPS spectra of LZO films deposited from a 1.0 M solution (NO_3^-/Cl^- precursors) and annealed under dry or humid conditions at 200 °C: C 1s (a, g), O 1s (b, h), Cl 2s (c, i), N 1s (d, j), La 3d (e, k), and Zr 3d (f, l) 117

AC6. XPS spectra of LZO films deposited from a 1.0 M solution (NO_3^-/Cl^- precursors) and annealed under dry or humid conditions at 500 °C: Cl 2s (a, b), N 1s (c, d), and Zr 3d (e, f) 120

AC7. GIXRD spectra for LZO films deposited from a 1.0 M solution (NO_3^- precursors) and annealed at 500 °C under dry or humid conditions 122

Figure Page

AC8. SEM images of LZO films deposited from a 1.5 M solution (NO_3^- precursors) and annealed at 500 °C under (a) dry or (b) humid conditions..... 123

AC9. *J-E* data for MIS devices fabricated from two-coat LZO (NO_3^-, 1.0 M) films (~100 nm) annealed under dry or humid conditions at various temperatures 124

AD1. FTIR spectra of a single layer LZO film deposited from a 1.00 M precursor solution sequentially heated in situ to various annealing temperatures 125

AD2. Single layer models fit to XRR data collected from (a) one, (b) two, (c) three, and (d) four coat films deposited from 1.00, 0.50, 0.33, and 0.25 M precursor solutions, respectively 127

AD3. Multilayer models fit to XRR data collected from (a) one, (b) two, (c) three, and (d) four coat films deposited from 1.00, 0.50, 0.33, and 0.25 M precursor solutions, respectively 129

AD4. Cross-sectional STEM-EDS profiles from a three layer LZO film deposited from a 0.33 M precursor solution. Intensity profiles plotted are the O Kα, La Lα, and Zr Lα signals vs. distance from the film surface 131

AD5. MEIS experimental data collected from a thin two layer (~8 nm) film overlaid with the best fit model 133

LIST OF TABLES

Table Page

5.1. C and O Atomic Percentages from XPS Peak Fitting in Figure 5.4a-d........... 61

AA1. XRR best-fit modeling parameters 103

AC1. XPS atomic percentages for fitted C 1s and O 1s spectra for LZO (NO_3^-/Cl^-) films annealed at 200 °C 118

AC2. XPS atomic percentages for La, Zr, O, C, Cl, and N species for LZO (NO_3^-/Cl^-) films annealed at 200 °C 119

AC3. XPS atomic percentages for La, Zr, O, C, Cl, and N species for LZO (NO_3^-/Cl^-) films annealed at 500 °C 121

AD1. XRR single layer best fit model parameters 128

AD2. XRR multilayer best fit model parameters 130

AD3. EPMA measurements.. 132

AD4. XPS measurements 134

LIST OF SCHEMES

Scheme | Page

AC1. A cartoon schematic of the steam annealing apparatus 110

CHAPTER I

INTRODUCTION

Metal Oxide Properties and Applications

Metal oxides display an extensive range of physical and electrical properties, making them ubiquitous in modern technologies.[1] For example, metal oxides function as water splitting catalysts,[2,3] cathode materials for Li ion batteries,[4,5] and electrochromics[6,7] in energy production, storage, and conservation technologies, respectively. Metal oxides also operate as dielectric and semiconductor components in integrated circuit and display technologies.[8–12] For all of these applications, thin films of metal oxides are preferred.

Thin Film Deposition Approaches

Vapor-phase Deposition Methods

Thin film materials are produced using vapor- or solution-phase methods. The most developed and widely employed methods are vapor-phase routes, which are generally considered the current industry standard.[13] These techniques can be further designated as physical vapor deposition (PVD) or chemical vapor deposition (CVD) methods. PVD methods sublimate or evaporate pure materials into the gas phase, which are then transported to and condensed onto a substrate.[14–16] CVD methods are similar but employ mixtures of volatile precursors that react with or decompose on a substrate.[17] Perhaps the most well-known CVD method is atomic layer deposition (ALD), which takes advantage of self-limiting chemical reactions to synthesize films with atomic-level precision.[13,18] In general, vapor-phase techniques produce high-quality (smooth, dense, defect-free) films,

but suffer from expensive precursors and equipment, large energy inputs, and significant waste (low-atom economy). Careful control of multi-metal composition is also challenging.[19,20]

Solution-phase Deposition Methods

Solution-phase methods offer the potential to circumvent many of the drawbacks of vapor-phase methods,[21,22] including significantly reduced precursor costs. A simple cost-analysis of vapor-phase and solution-phase La precursors illustrates this. $(^iPrCp)_3La$, a common liquid-injection ALD La precursor,[23–25] is ~200 times the cost of $La(NO_3)_3 \bullet 6H_2O$, an analogous solution deposition precursor[26,27] (approximately $8,445 vs. $42 per mole of La, respectively). Solution-phase methods also offer higher atom economies relative to vapor-phase methods; solution precursor waste has the potential to be recovered and recycled,[28,29] while vapor-phase deposition precursors cannot be recycled because they are chemically altered during the deposition process. Furthermore, solution-phase methods employ relatively simple and inexpensive deposition equipment and lower energy inputs, while also offering the potential for high-throughput processing and large area coverage.[30–33] Facile manipulation of precursor stoichiometry also enables careful control of multi-metal oxide composition and tuning of thin film properties.[34]

In the field of solution-phase thin film deposition, sol-gel methods have dominated.[35] Traditional sol-gel methods utilize metal alkoxides or metal salts suspended in organic solvents, often with added chelating agents to produce homogeneous solutions. Controlled addition of water, acid, or base facilitates hydrolysis of the metal alkoxides/salts to metal hydroxides, which subsequently condense to form the

corresponding metal oxide during thermal processing.[36–38] In general, sol-gel methods can produce films with tailored porosity and properties. However, elevated annealing temperatures required to fully remove residual carbon (which can negatively impact film properties[39,40]) can result in rough, non-uniform film morphologies.[41]

Aqueous solution-phase routes avoid the need for organic additives and solvents altogether, producing smooth, continuous films with competitive morphology and device properties.[42] The simplest aqueous routes employ water soluble metal nitrate or metal chloride salts as precursors.[43–51] Increasing the pH of these acidic solutions through the addition of base or electrochemical reduction of H^+ ions can facilitate metal oxo-hydroxo cluster/oligomer formation for some metal cations.[52–59] In the latter case, reduction of H^+ ions to H_2(g) at the working electrode drives NO_3^- to the counter electrode and out of the main compartment as the metal oxo-hydroxo cluster/oligomer forms, effectively reducing nitrate in the precursor solution and subsequent films.[55] Because nitrates and other counterions must be eliminated during film evolution (either through evaporation of the conjugate acid or thermal decomposition) to realize fully condensed oxides, this electrochemical reduction approach is an effective method for reducing residual nitrate content in aqueous-derived oxides.

Challenges in Solution-phase Deposition

Despite the potential of solution-phase deposition to address the deficiencies of vapor-phase deposition, the promise of low-temperature routes to fully-dense, defect-free metal oxide thin films has not been broadly realized. Many solution deposition methods require relatively high processing temperatures (≥400 °C) to fully remove residual

counterions and solvent. A number of strategies for reducing processing temperatures have been investigated, including deep-ultraviolet photochemical activation,[60] ozone annealing,[61] and microwave irradiation.[62] Combustion synthesis is another widely investigated method for forming metal oxides at low temperatures,[1,63–65] but there is evidence that combustion occurs only in bulk powders and not in thin film samples because of inherent differences in sample mass and thermal transport.[66–68] In the case of sol-gel films, steam annealing has also been shown to promote condensation of metal organic precursors and formation of the subsequent metal oxide network.[69–71] However, the effect of steam annealing on the evolution of aqueous-derived films has not been explored.

High processing temperatures are also generally required to improve the stability of aqueous-derived films. Films processed at low temperatures (<400 °C) are often unstable with respect to ambient water absorption after annealing. Water absorption roughens the film surface, which negatively impacts device properties.[72] Researchers are exploring a variety of approaches to ameliorate post-anneal water absorption to realize lower processing temperatures. For example, Keszler and coworkers deposited a thin (10-20 nm) HfO_2 capping layer on aluminum phosphate oxide (AlPO) thin film dielectrics to create an AlPO-HfO_2 dielectric stack, which eliminated the negative effects of water absorption in the AlPO films.[73,74] Specifically, an AlPO-HfO_2 stack annealed at 350 °C for 1 h was shown to have the same resistance to water absorption as an AlPO film annealed at 600 °C for 1 h. Although dielectric properties were enhanced in the case of the AlPO-HfO_2 stack, this approach has a limited applicability; the deposition of an additional HfO_2 dielectric layer may not always be advantageous for a given application.

Furthermore, this report did not investigate the general applicability of this approach for preventing water absorption in other metal oxide thin films. A more general approach for eliminating water absorption in films processed at low temperatures is still needed.

It is generally assumed that homogeneous solution precursors produce homogeneous thin films.[75] However, a few reports in the sol-gel and aqueous deposition literature show data suggesting the presence of inhomogeneities.[73,76–79] These inhomogeneities may arise from density or compositional variations, but the nature of these non-uniformities and their implications on device properties have not been investigated.

Addressing Challenges in Solution-phase Deposition: This Work

To address these challenges, fundamental understanding of the processes involved in the evolution of aqueous precursors to metal oxide thin films is required. The elucidation of these processes is complicated by the inherently small volume of thin films samples, requiring the use of multiple complementary techniques to craft a complete picture of film formation. Chapter II surveys these techniques, providing a foundation for the subsequent chapters that are focused on advancing the field of aqueous solution deposition in three areas. First, all-inorganic aqueous deposition routes to high-κ lanthanum zirconium oxide (LZO) and zirconium aluminum oxide (ZAO) dielectrics are detailed in Chapters III and IV, respectively. The chemical evolution and morphologies of the LZO and ZAO thin films are studied as a function of annealing temperature and metal composition. Additionally, incorporating these dielectrics into metal-insulator-semiconductor (MIS) capacitors allowed for evaluation of their electrical properties. Second, a general route to lowering processing temperatures and improving resistance to

post-anneal water absorption using steam annealing is described in Chapter V. Specifically, the impact of steam annealing on the bulk chemistry of LZO, yttrium aluminum oxide, and zinc oxide thin films is reported. A detailed investigation of the effect of steam annealing on post-anneal water absorption, thin film morphology, and insulating properties of LZO dielectrics is also discussed. Lastly, the elucidation of non-uniform electron densities in single- and multi-metal aqueous-derived films are presented in Chapters VI and VII, respectively. These inhomogeneities are related to inhomogeneous metal distributions in hafnium oxide sulfate (HafSOx) and LZO films. Implications of these non-uniform metal distributions on dielectric properties are investigated for the LZO system.

Authorship Statement

This dissertation contains previously published coauthored material. Chapter III was previously published in *ACS Applied Materials and Interfaces* with Tsung-Han Chiang, Paul N. Plassmeyer, Matthew G. Kast, Alexander C. Lygo, Aidan K. Grealish, Shannon W. Boettcher, and Catherine J. Page. Chapter IV was previously published in *RSC Advances* with Emma C. Waddington, Connor A. Crump, Elizabeth A. Bryan, Tyler S. Gleckler, Michael R. Nellist, Brett A. Duell, Daniel P. Nguyen, Shannon W. Boettcher, and Catherine J. Page. Chapter V was previously published in *Chemistry of Materials* with Paul N. Plassmeyer, Deok-Hie Park, Lisa J. Enman, Aidan K. Grealish, Brenna L. Kirk, Shannon W. Boettcher, Douglas A. Keszler, and Catherine J. Page. Chapter VI was previously published in *ACS Applied Materials and Interfaces* with Kurtis C. Fairley, Devin R. Merrill, Keenan N. Woods, Jeffrey Ditto, Can Xu, Richard P. Oleksak, Torgny

Gustafsson, Darren W. Johnson, Eric L. Garfunkel, Gregory S. Herman, David C. Johnson, and Catherine J. Page. Chapter VII was previously published in *ACS Applied Materials and Interfaces* with Milana C. Thomas, Gavin Mitchson, Jeffrey Ditto, Can Xu, Donna Kayal, Kathleen C. Frisella, Torgny Gustafsson, Eric Garfunkel, Yves J. Chabal, David C. Johnson, and Catherine J. Page.

Bridge

Chapter I provided a broad overview of thin film deposition approaches, a summary of grand challenges in the field of aqueous deposition, and an outline of the contributions included in this work. Chapter II provides an overview of the thin film analytical techniques utilized in Chapters III, IV, V, VI, and VII. Many traditional material characterization techniques, such as thermogravimetric analysis, have insufficient sensitivities for thin film analysis because of the inherently small volume of these samples. Fortunately, there are a number of complementary characterization techniques that have been specifically developed for probing thin film samples.

CHAPTER II

THIN FILM CHARACTERIZATION

Challenges in Thin Film Analysis

The elucidation of chemical reactions that occur during the evolution of aqueous solutions to metal oxide thin films is complicated by the inherently small volume of thin film samples, which makes characterization challenging. Bulk powders are often used as analogues for thin films, but differences in sample geometry and mass transport make direct comparisons difficult.[1–4] Additionally, amorphous materials lack long-range atomic order, further complicating structural characterization.[4] These amorphous materials are a major focus of this work and are preferred for microelectronic device applications because grain boundaries in crystalline materials provide pathways for current leakage.[5] Because of these challenges, multiple complementary methods are generally required to fully characterize the evolution and properties of thin film materials.

Physical Characterization

Excellent thin film morphology (smooth, dense, uniform) is critical for the fabrication of functional microelectronic devices.[6–8] X-ray reflectivity (XRR) is a non-destructive technique that provides a wealth of morphological information for thin film samples.[9,10] In XRR, the incident beam and the detector are coupled ($\theta/2\theta$ scanning geometry) and scans are performed at low incident angles (i.e., 0 to 10° 2θ). At angles above the critical angle (the angle of total reflectance), X-rays penetrate the sample and are diffracted from parallel surfaces with distinct electron densities (e.g., film surface and film-substrate

interface). Constructive and deconstructive addition of the diffracted X-rays result in an XRR pattern, which provides information on film thickness, electron density, and roughness (Figure 2.1a).

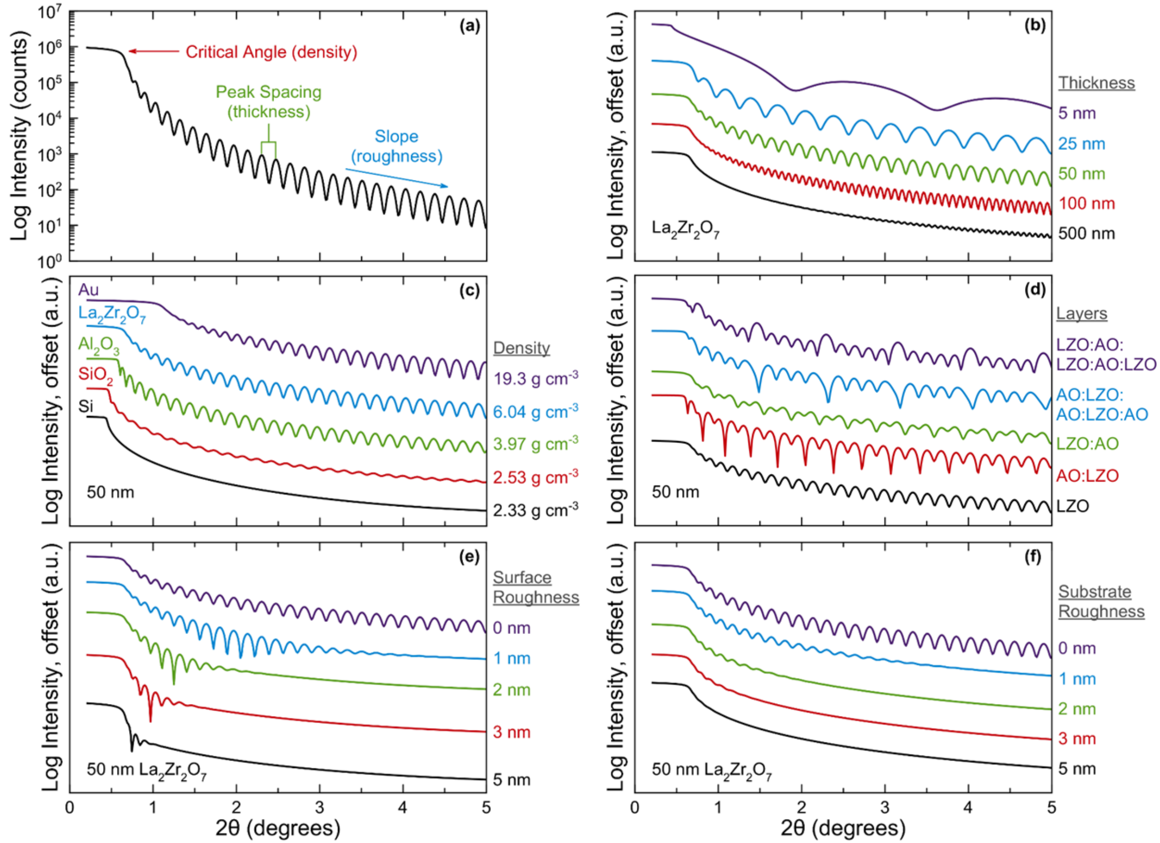

Figure 2.1. Simulated XRR patterns for films of various composition and thickness on a Si substrate generated using Bede REFS modeling software. (a) Main features and corresponding extractable information, (b) $La_2Zr_2O_7$ (LZO) films of various thickness, (c) 50 nm films of various composition and density, (d) 50 nm (total thickness) nanolaminates comprised of LZO and Al_2O_3 (AO) layers of equal thickness, (e) 50 nm LZO films with various surface roughness, and (f) 50 nm LZO films with various film-substrate interface roughness.

Film thickness is inversely proportional to the spacing of the peaks, or Kiessig fringes, in XRR patterns (Figure 2.1b). The electron density of the sample is directly related to the square of the critical angle (Figure 2.1c). Additionally, the amplitude of the

Kiessig fringes increases with increasing electron density contrast; large differences between sample and substrate electron density improve the resolution of Kiessig fringes (Figure 2.1c). Stacks of thin films with different electron densities (e.g., nanolaminates) produce XRR patterns with modulated periodicity related to the number of deposited layers (n), with n - 1 low-intensity fringes between intense peaks or valleys (Figure 2.1d).[11,12] Kiessig fringe amplitude is also heavily dependent on surface and interface roughness (e.g., film-substrate interface). Specifically, Kiessig fringe intensity (and the maximum angle in 2θ that they can be resolved) decreases as roughness increases (Figure 2.1e,f). Quantitative thickness, electron density, and roughness values can be extracted from XRR patterns using modeling software that generate a best fit based on an initial model input and a genetic algorithm to minimize residuals.[13] It is important to use a complementary technique (such as electron microscopy, discussed below) to inform XRR models; complex fits with an unreasonable number of parameters may fit the raw data better, but are not always meaningful.

XRR provides important insight into the surface and internal morphology of thin films, but the technique requires ultrasmooth surfaces and interfaces to obtain well-resolved Kiessig fringes for analysis. Atomic force microscopy (AFM) can probe the surface morphology of significantly rougher films.[14] In AFM, a sharp cantilever (tip radius ~15 to 40 nm) probes a sample surface using one of a number of sample interaction modes (e.g., tapping mode). As the cantilever scans the sample, vertical and lateral deflections are registered by a reflected laser beam (detected by a position-sensitive photo diode). AFM can produce a topographical map of a specified surface area, and subsequent image processing can calculate a surface roughness (most commonly

root-mean-square roughness).[8,15–18] Although AFM and XRR probe different types of roughness (physical vs. electron density roughness, respectively), the roughness determined by both techniques are complementary.[9]

The topographical maps obtained from AFM and electron density profiles from XRR can be further supported by electron microcopy techniques, which offer a method for visualizing the surface and bulk morphology of samples on a nanometer scale. In scanning electron microscopy (SEM) a high-energy beam of electrons is rastered along a sample (i.e., film surface or cross-section), causing the emission of secondary electrons that are detected to form a 3D image.[19–24] Conductive samples are preferred for SEM imaging to prevent the buildup of static charge at the sample surface (charging effects) that cause anomalous brightness and prevent collection of high-quality images.[25] Charging effects can be mitigated by applying a conductive coating to the film surface, decreasing the accelerating voltage of the electron beam, or applying a bias to the sample.[26] In this work, insulating dielectric films were coated with Al for SEM analysis.

Transmission electron microscopy (TEM) can also be used to visualize thin film samples.[12,27–29] In TEM, an electron beam is passed through an extremely thin (~50 to 100 nm) sample, which is prepared by milling out a cross-section of the film using a focused ion beam in an SEM instrument.[30,31] Although TEM can only produce 2D images, the resolution of TEM is superior to SEM; indeed, individual atoms can be imaged using TEM.[32,33] TEM can also be operated in scanning mode (STEM), allowing analysis of thicker samples and access to dark field and secondary electron imaging modes.[34] SEM and (S)TEM are powerful tools for visualizing nanomaterials, but they can alter samples during prolonged exposure to high-energy electron beams.[35,36] Films

processed at low-annealing temperatures that are not fully condensed are particularly beam-sensitive.

Chemical Analysis

Metal oxide properties depend on the degree of oxide condensation and densification of the material and are often negatively impacted by residual counterion or solvent content. A common technique for investigating bulk film chemistry is Fourier transform infrared (FTIR) spectroscopy, which takes advantage of characteristic absorption of IR radiation at specific wavelengths related to vibrational modes with associated changes in dipole moments.[4,37–41] Vibrational modes associated with water and nitrate are of particular interest to this work. Metal oxide vibrational modes generally occur at low wavenumbers and are difficult to detect and assign definitively. Films can be probed using attenuated total reflection (ATR) or transmission modes. The FTIR data presented in this work employ transmission FTIR, using an N_2 atmosphere to remove contributions from ambient H_2O and CO_2 and double-side polished Si wafers as a substrate.

FTIR is a convenient method for investigating residual counterion and solvent content in thin films, but not all species are FTIR "active." Thermal programmed desorption (TPD) is a complementary technique for investigating residual counterion and solvent content. In TPD, a previously annealed sample is heated under ultrahigh vacuum (UHV) conditions and desorbed species are detected using a mass spectrometer. TPD has the additional benefit of providing insight into film evolution reaction pathways through detection of molecular fragments (although the influence of UHV conditions must be considered).[37,38,42–44]

Another analytical UHV technique is X-ray photoelectron spectroscopy (XPS). In XPS, a sample is irradiated with X-rays and the measured kinetic energy distribution of ejected electrons provides information about composition, formal oxidation states, and local chemical environments.[45–48] This technique is surface sensitive (~10 nm) and can also probe bulk film chemistry by sputtering through the sample with an ion gun between XPS scans (depth-profiling analysis). To extract quantitative composition values, XPS peaks are modeled using a peak fitting program. Similar to XRR data fitting, a complex model with many peaks can always fit the data better but may not be meaningful; therefore, it is critical to inform XPS peak fitting with educated assumptions concerning the composition of the film.

In addition to XPS, medium energy ion scattering (MEIS) provides a method for investigating surface composition. MEIS is a high-resolution version of Rutherford backscattering, which measures the number and energy of backscattered ions to create a quantitative areal density and compositional depth-profile of the surface region.[49,50] For very thin films, a bulk density can be calculated if the film thickness is known (e.g., from XRR or TEM).

Heavy atom distributions in the bulk film can be analyzed using high-angle annular dark-field (HAADF) STEM. In HAADF-STEM, intensity is proportional to the square of the atomic number, providing insight into the distribution of heavy atoms in samples with little to no long range order.[51] More detailed elemental mapping can be performed using STEM energy-dispersive X-ray spectroscopy (STEM-EDS) by combining statistical analysis of STEM-EDS spectral images[52] with average bulk composition determined using electron probe micro-analysis (EPMA).[10,53]

Electrical Characterization

As discussed in Chapter I, metal oxides are critical microelectronic device components. For example, metal oxides are important gate dielectric components in thin-film transistors (TFTs, used in liquid crystal display technologies) and metal oxide field effect transistors (MOSFETs, used in integrated circuit technologies).[54–58] The most common gate dielectric is SiO_2 because of its excellent insulating properties (i.e., large band gap, low leakage current densities, high breakdown fields), high thermodynamic stability on Si, and low-defect density interface with Si.[59] To keep up with demands for increased performance, transistors (and their dielectric components) have been scaled down to increase device capacitance, which results in higher drive currents and decreased switching time.[59] This can be demonstrated by considering a parallel plate capacitor described by Eq. 2.1, where C is capacitance, κ is the dielectric constant (or relative permittivity) of the dielectric material, ε_0 is the permittivity of free space (a constant), A is the area of the capacitor, and t is the thickness of the dielectric component.

Eq. 2.1 $$C = \kappa\, \varepsilon_0\, A\, t^{-1}$$

At $t \leq 1$ nm, current leakage via electron tunneling through the dielectric layer becomes a significant issue and represents a fundamental scaling limit for high-performing devices. Replacement of SiO_2 with a high-κ dielectric would allow for continued improvements in device C without shrinking t, thereby eliminating electron tunneling effects.[57–60] For example, a dielectric material with $\kappa = 16$ and $t = 4$ nm would have an approximate equivalent C to a SiO_2 ($\kappa = 3.9$) with a thickness of 1 nm. Although

device performance does not scale perfectly with κ because of quantum mechanical and depletion effects from a Si substrate and gate,[59] this simplified picture illustrates the potential for high-κ materials to enable future improvements to transistor performance.

Ideally, the functionality of a gate dielectric would be directly investigated by incorporation into a transistor device and measuring device performance. However, the fabrication of thin-film transistors is challenging; interfacial reactions and component compatibility with multiple processing steps are major issues that generally require lengthy optimization procedures.[22] To avoid these difficulties, basic electrical characteristics of dielectrics can be characterized using relatively simple metal-insulator-semiconductor (MIS) devices prepared by stacking an insulating metal oxide between a Si substrate and a metal top contact.[23,61] In this work, Al dots are thermally evaporated onto an annealed film using a shadow mask. The dot size determines the area of the MIS capacitor device, and smaller devices generally display improved behavior because fewer defects in the insulating layer are likely to be sampled. Contact to the Si substrate (semiconductor) is made by physically scratching through one corner of the film to the bare Si substrate using a scribe and then applying a conductive In/Ga eutectic.

The dielectric constant of the insulating layer can be measured using impedance spectroscopy, in which an alternating current is applied at a specific frequency and the magnitude of the current and its phase are recorded.[62] This process is repeated for a range of frequencies. Capacitance can be calculated from the measured impedance (Z) for a specific frequency (f) using Eq. 2.2. The dielectric constant can then be calculated using Eq. 2.3, a rearranged form of Eq. 2.1.

$$\textbf{Eq. 2.2} \quad C = (2\pi f Z)^{-1}$$

$$\textbf{Eq. 2.3} \quad \kappa = C\, t\, (\varepsilon_0 A)^{-1}$$

Additionally, the leakage current density through the dielectric layer and the breakdown field (the field at which all insulating behavior is lost) can be determined by measuring current as a function of applied voltage (electric field).[23,63] Generally, low leakage currents and high breakdown fields are desirable for gate dielectric applications. Electrical characterization of dielectric materials will be discussed in Chapters III, IV, V, and VII.

Bridge

Chapter II surveyed a number of complementary thin film characterization techniques, which will be used extensively in the following Chapters. Together, these techniques provide insight into the evolution of aqueous precursors to metal oxides, which is critical for developing aqueous deposition chemistry for widespread industrial production of thin films materials.

CHAPTER III

HIGH-κ LANTHANUM ZIRCONIUM OXIDE THIN FILM DIELECTRICS FROM AQUEOUS SOLUTION PRECURSORS

Authorship Statement

This chapter was previously published as a full article in *ACS Applied Materials and Interfaces* in 2017 (volume 9, pages 10897-10903) and was coauthored by Keenan N. Woods, Tsung-Han Chiang, Paul N. Plassmeyer, Matthew G. Kast, Alexander C. Lygo, Aidan K. Grealish, Shannon W. Boettcher, and Catherine J. Page. The manuscript was written by K.N.W. with contributions from T.-H.C., P.N.P., and M.G.K. Editorial assistance was provided by S.W.B. and C.J.P. Experiments were performed by K.N.W., T.-H.C., M.G.K., A.C.L., and A.K.G. with data analysis done by K.N.W., T.-H.C., P.N.P., and M.G.K.

Introduction

Amorphous metal oxide thin films are used in a range of technological applications, particularly as channel and/or gate dielectric layers in metal-insulator-semiconductor field-effect transistors (MISFETs)[1] and thin-film transistors (TFTs).[2] In the case of gate components, the incorporation of high-κ dielectrics into devices is attractive for reducing power consumption.[3] Zirconium oxide (ZrO_2)[4–11] and lanthanum oxide (La_2O_3)[4,12–15] are two high-κ materials (κ = 22 and 27, respectively) that have attracted interest as gate layers in MISFETs.[16] However, ZrO_2 crystallizes at relatively low-annealing temperatures (~500 °C), which results in undesirable grain boundary formation, and

La_2O_3 suffers from water and carbonate absorption,[17–19] both of which result in increased leakage currents and poor device properties.[20] By combining the La and Zr components into ternary lanthanum zirconium oxides, it may be possible to take advantage of the inherent high-dielectric properties while suppressing crystallization and eliminating carbonate and water absorption.

Ternary oxide phases are known for La-Zr-O,[21] and the $La_2Zr_2O_7$ crystalline pyrochlore has been extensively investigated as a substrate for epitaxial growth of YBCO superconductors.[22–29] In the past decade, amorphous $La_xZr_yO_z$ has been studied as a dielectric material and has been synthesized via vacuum-based vapor-deposition routes[30–32] and sol-gel solution-deposition routes.[33–36] Although vapor-deposition routes generally produce high-quality films,[37–40] they are energy-intensive, require expensive starting materials and equipment, and have low atom economy. In contrast, solution-deposition routes are relatively inexpensive, require less-sophisticated equipment, and can produce less waste.[41–56] However, common sol-gel routes rely on organic additives and solvents which must be expelled during film processing, leading to porosity[57] and undesirable high leakage currents in devices.[58,59] Many of these disadvantages can be circumvented by using aqueous precursors.

We report an all-inorganic, aqueous route to $La_xZr_yO_z$ (where $x = 2$, $y = 2$, and $z = 7$). The method employed is similar to the prompt inorganic condensation (PIC) route developed by Keszler and coworkers,[60,61] which has been used to synthesize a range of metal oxide dielectrics,[47,52,62–65] in some cases producing films that rival those deposited by vapor-phase methods.[66,67] The amorphous $La_2Zr_2O_7$ (LZO) films reported herein are smooth on a subnanometer scale and are fully condensed and densified by 600 °C.

Crystallization of the LZO films does not occur until 800 °C, approximately 300 °C higher than for pure ZrO_2. Electrical characterization of LZO-based metal-insulator-semiconductor (MIS) devices reveal high dielectric constants with low deviation from ideal capacitive behavior and current density characteristics competitive with other aqueous, solution-deposited metal oxide dielectrics.[61,62,64–67]

Experimental

Precursor Solution Preparation

A 1.00 M (total metal, 1:1 La:Zr) LZO precursor solution was prepared by dissolving $ZrO(NO_3)_2 \cdot xH_2O$ (Sigma Aldrich, 99%) in 18.2 MΩ cm Millipore H_2O by gentle heating (~70 °C) and vigorous stirring of the solution. After complete dissolution, $La(NO_3)_3 \cdot 6H_2O$ (Alfa Aesar, 99.9%) was added in small portions to the still stirring solution. The solution was then diluted to 1.00 M and filtered through a 0.45 μm PTFE syringe filter.

Thin Film Preparation

Si substrates (2 x 2 cm squares) were sonicated in 5% Decon Labs Contrad-70 solution for 5 min and thoroughly rinsed with 18.2 MΩ cm H_2O. Substrates were then spin-dried using a spin-coater and subjected to a 1 min O_2/N_2 plasma etch using a PE-50 Benchtop Plasma Cleaner (Plasma Etch, Inc.) set to maximum power. Substrates were again rinsed with 18.2 MΩ cm H_2O and spin-dried before film deposition.

Five drops of LZO precursor solution were deposited onto cleaned Si substrates through a 0.2 μm PTFE syringe filter, and then immediately spun at 3000 RPM for 30 s.

Samples were directly transferred to a custom-built hot plate (consisting of an Al block with heating elements, a thermocouple, and a PID controller) set to 125 °C and ramped to a final annealing temperature of 200, 300, 400, or 500 °C at a rate of 25 °C min^{-1} and held for 1 h. Stacked, two-coat films for MIS device fabrication were annealed to 300 °C, 400 °C, or 500 °C for 10 min between coats and were annealed for 1 h at the desired final annealing temperature. Samples with a final annealing temperature over 500 °C were first heated to 500 °C for 10 min on the hot plate (for each layer), cooled to room temperature, and transferred to a box furnace which was ramped to the final annealing temperature (ramp rate 25 °C min^{-1}).

Precursor Solution Characterization

Samples were prepared for thermogravimetric analysis (TGA) from individual 1.0 M solutions of $ZrO(NO_3)_2 \cdot xH_2O$, $La(NO_3)_3 \cdot 6H_2O$, and LZO precursor that were dried at 50 °C for 12 h. TGA was performed using a TA Instruments Q500A with a ramp rate of 5 °C min^{-1} under a N_2 atmosphere.

Thin Film Characterization

Fourier-transform infrared (FTIR) spectra on LZO films deposited on lightly doped double-side polished p-type Si substrates were collected using a Thermo Fisher Nicolet 6700 spectrometer. To increase signal-to-noise, FTIR analysis was performed on thicker films made from 1.8 M total metal concentration LZO precursor solutions. Background subtraction was performed by using bare Si substrates subjected to the same thermal treatment.

Grazing incidence X-ray diffraction (GIXRD) and X-ray reflectivity (XRR) analysis were conducted using a Rigaku SmartLab X-ray diffractometer (Cu Kα radiation, 40 kV, and 44 mA). X-ray reflectivity data was modeled using the Bede REFS v4.00 software package,[68] and film thicknesses and densities were extracted from the generated best fits.

Atomic force microscopy (AFM) measurements were carried out on a Digital Instruments Multimode Atomic Force Microscope with an IIIa Controller. Si tapping mode probes (Nanosensors, PPP-NCH) were used, and three measurements from different locations were taken per film over a 500 nm^2 window at a scan rate of 1 $\mu m\ s^{-1}$. The height and phase response were collected on the retrace sweep. After data collection, a first order flatten fit and third order plane fit was applied to remove bowing effects from the piezoelectric motors and deviations in the sample from parallel to the piezoelectric motors. NanoScope Analysis software was used to calculate the root-mean-square roughness (R_{rms}) over the area of the scan window.

Cross-sectional scanning electron microscopy (SEM) was performed using a ZEISS Ultra-55 FESEM using a 20 μm aperture and 5 kV accelerating voltage. Films were first coated in thermally evaporated Al to prevent charging effects while imaging.[69]

Device Fabrication and Testing

MIS devices were fabricated to determine LZO dielectric constants and current density-electric field characteristics (*J-E*). Two-coat LZO films (~100 nm) were deposited on degenerately doped p-type Si (0.008-0.020 Ω cm). Al top contacts (0.013 cm^2, ~100 nm thick) were thermally evaporated onto the stacked LZO films through a shadow mask. A back contact was made by scribing through the film to the Si substrate

and applying an In/Ga eutectic. Dielectric constants were calculated from impedance measurements measured using an Agilent 4284A Precision LCR meter (20-100,000 Hz, 500 mV oscillation amplitude). Batch-to-batch variations were evaluated by making three separate samples per annealing temperature and measuring impedance of five MIS devices per sample. *J-E* characterization was accomplished using a Keithley 2400 SourceMeter (0.2 V steps, 0.2 s delay). *J-E* hysteresis tests were performed using an Agilent 4155B semiconductor parameter analyzer (0.1 V steps, 0.1 s delay). All device testing was performed in ambient atmosphere in a dark environment.

Results and Discussion

The decomposition pathways of dried $La(NO_3)_3{\bullet}xH_2O$, $ZrO(NO_3)_2{\bullet}xH_2O$, and LZO precursor powders to their corresponding oxides were examined by TGA (Figure 3.1). Thermal decomposition of $La(NO_3)_3{\bullet}xH_2O$ begins with a small mass loss around 100 °C, likely from loss of excess (unbound) water, and proceeds through two large mass-loss events starting around 180 and 400 °C, attributable to the loss of bound water and nitrates, respectively. The final mass-loss event starting around 500 °C can be attributed to the expulsion of residual water and nitrates during the final condensation and densification of the oxide. The mass-loss profile of $ZrO(NO_3)_2{\bullet}xH_2O$ is more gradual and appears as two broad mass-loss events from 100 to 220 °C and 220 to 400 °C. These events likely correspond to gradual water and nitrate loss, respectively. The mass loss profile of the LZO precursor appears to be an approximate average of the two metal nitrate salts and shows a gradual mass decrease from 100 to 160 °C (water loss), a mass-loss event around 220 °C (nitrate loss), and a more pronounced, gradual mass loss over

several hundred degrees (further nitrate loss, condensation, and film densification). Conversion of the LZO precursor to the corresponding oxide is complete by 500 °C, which occurs at a lower temperature than for either the La or Zr nitrate salts individually. Although thermal decomposition of the bulk powders is not necessarily representative of the decomposition pathways in thin films, the bulk mass-loss events offer insight into film formation phenomena and can be related to the infrared spectroscopy conducted on thin film samples heated to various temperatures.

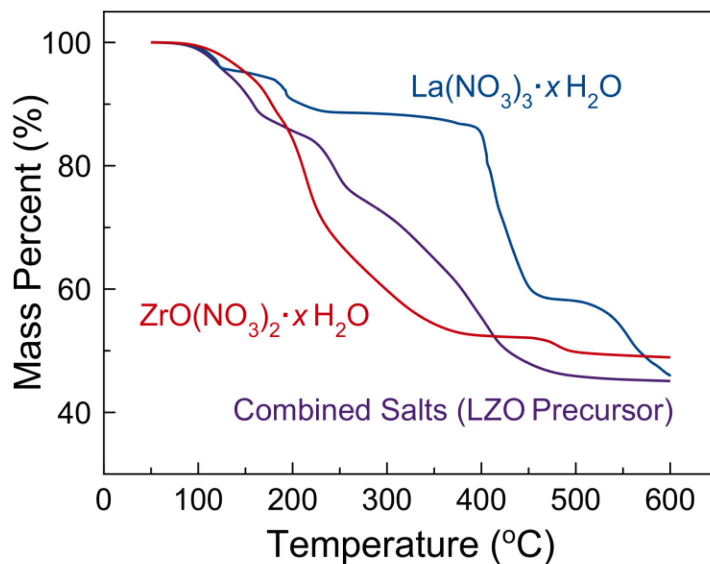

Figure 3.1. TGA of $La(NO_3)_3$•xH_2O (blue), $ZrO(NO_3)_2$•xH_2O (red), and LZO precursor (purple) powders derived from drying 1.0 M solutions.

FTIR spectroscopy was used to probe the hydroxide, water, and nitrate content in LZO films after annealing to various temperatures (Figure 3.2). Residual hydroxide and water (monitored via the broad O-H stretching mode peak around 3500 cm^{-1} and the sharp H-O-H bending mode peak around 1650 cm^{-1})[70] and NO_x content (monitored via the N-O stretches centered around 1280 and 1460 cm^{-1})[71] is dramatically reduced

between 200 and 300 °C. Loss of these species is important for film stability; films annealed at or below 200 °C were not stable, absorbing water and becoming cloudy after removal from the hot plate. Due to their instability, these low-temperature annealed films were not studied by other methods and are not discussed further. By 500 °C, water and hydroxides are completely removed from the films, indicating that complete condensation has occurred. Residual NO_x appear to remain in the films up to 600 °C. The sharp peaks at 744 and 1032 cm^{-1} are present only in the spectrum for the 200 °C sample and indicate the presence of hydrated metal nitrate species.[71,72] The peak centered around 1100 cm^{-1} corresponds to Si-O-Si[73,74] vibrations and is the result of small differences in the subtraction of the sample spectra and the bare Si substrate reference.

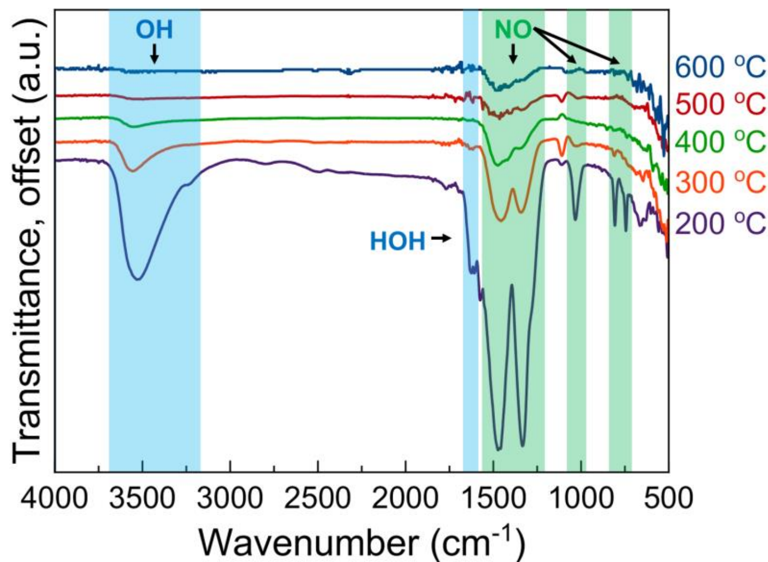

Figure 3.2. FTIR spectra of LZO films annealed between 200 and 600 °C.

Generally, polycrystalline films are undesirable for gate dielectrics because grain boundaries provide pathways for current leakage.[62] Amorphous films are thus preferred. GIXRD was used to assess the degree of crystallization in the films as a function of

annealing temperature (Figure 3.3). Films remained amorphous until 800 °C, at which temperature LZO begins to crystallize as the cubic pyrochlore phase (ICSD 154752).[75] At temperatures above 1000 °C, a mixture of phases is observed. The films used in MIS devices discussed below were prepared at temperatures well below the crystallization temperature (≤600 °C).

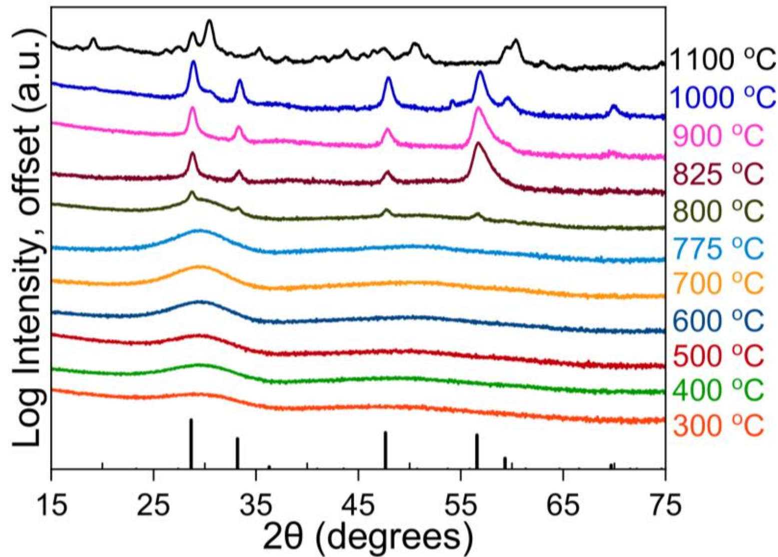

Figure 3.3. GIXRD of LZO films annealed between 300 and 1100 °C. LZO forms the cubic pyrochlore phase (ICSD 15475, peak positions shown in black at plot baseline) between 800 and 900 °C but decomposes at higher annealing temperatures.

The morphology of LZO films annealed between 300 and 600 °C was examined using XRR (Figure 3.4a). In order to extract thickness, density, and surface roughness information for the LZO films, modeling of the XRR patterns was conducted using Bede REFS software.[68] Best fits were obtained using two-layer models comprised of a bulk layer and a ~1-3 nm capping layer of different density (Figure 3.4 and Table AA1), consistent with XRR modeling performed on other aqueous solution-processed films.[76] Total film thickness decreases with increasing temperature, consistent with FTIR results

demonstrating the loss of H_2O and NO_x species as temperature increases. Overall film density (calculated from a weighted average of the densities derived from the two layer models) increases from 4.35 g cm^{-3} (300 °C) to 5.27 g cm^{-3} (600 °C), approximately 90% of the bulk density of the pyrochlore $La_2Zr_2O_7$ (6.05 g cm^{-3}).[77] Surface roughness was remarkably low (≤0.4 nm) for all samples (Figure 3.5b).

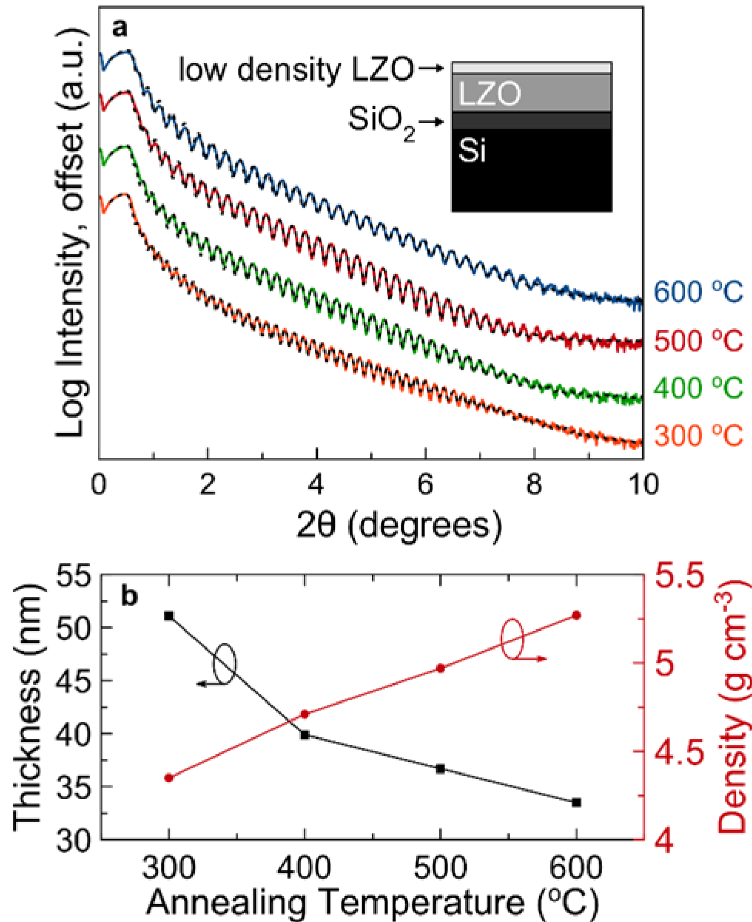

Figure 3.4. (a) XRR patterns of LZO films annealed between 300 and 600 °C and best-fit models (dashed, black lines). A cartoon inset depicts the two-layer model necessary for generating good fits to the data. (b) Total thickness and total density (weighted average of two-layer model) extracted from best-fit models of XRR data in panel (a).

AFM was used to corroborate surface roughness determined from XRR modeling (Figure 3.5). R_{rms} values of < 0.25 nm were calculated from AFM images (500 nm^2 area)

of LZO films annealed between 300 and 600 °C. Film roughness decreases from 300 to 400 °C but remains constant (within error) at higher annealing temperatures. R_{rms} values determined by AFM are smaller than surface roughness values determined by XRR data modeling, which can be ascribed to differences in how AFM and XRR measurements probe the samples.[78] The subnanometer smoothness of these films makes them promising materials for a variety of electronic devices, including TFTs.[79–81]

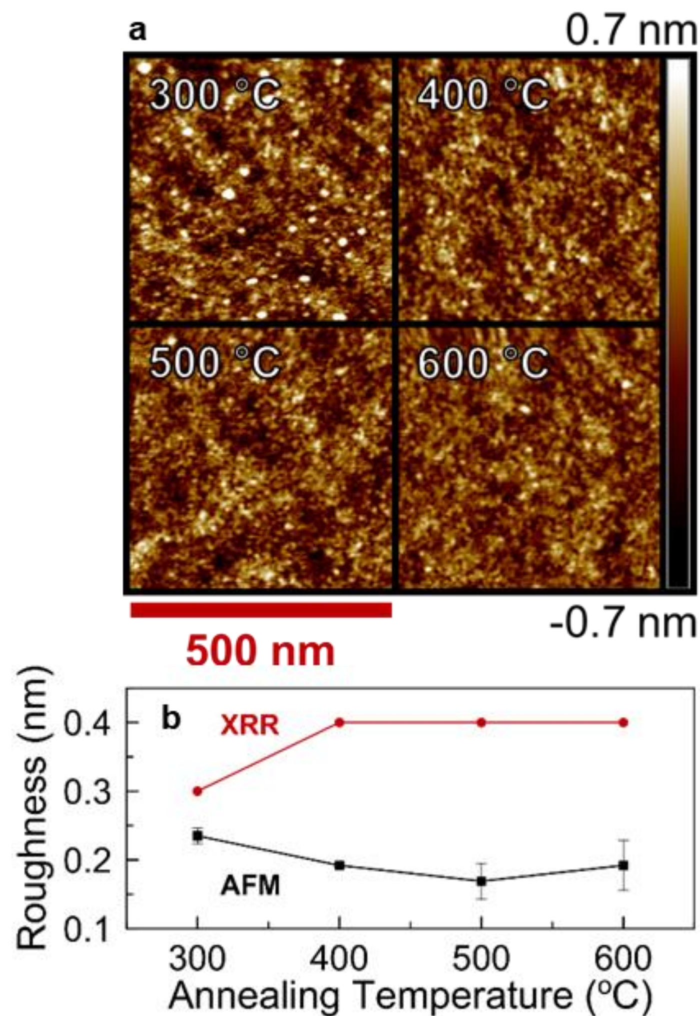

Figure 3.5. (a) Representative AFM images of a 500 nm^2 area and (b) comparison of surface roughness determined by XRR and AFM for LZO films annealed between 300 and 600 °C.

Cross-sectional SEM was used to visualize the morphology of stacked, two-coat LZO films used in electrical device fabrication (Figure 3.6). The films are uniform, dense, noncrystalline, and display no signs of interfacial roughness. Film thickness decreases with increasing annealing temperatures, which is in agreement with the trends observed by XRR.

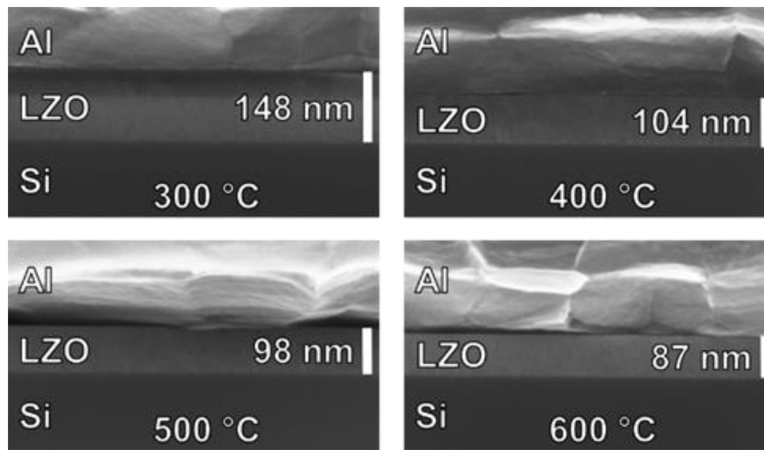

Figure 3.6. Cross-sectional SEM images of two-coat LZO films annealed at temperatures between 300 and 600 °C.

The dielectric characteristics of LZO-based MIS devices were measured using impedance spectroscopy. Dielectric constants and loss tangents were measured at frequencies between 20 and 100,000 Hz (Figure AA1), and dielectric constants and loss tangents measured at 1 kHz are shown in Figure 3.7a. The dielectric constant increases steadily with increasing annealing temperature, starting around 12.2 at 300 °C and reaching 16.4 at 600 °C. Loss tangents decrease with annealing temperature, consistent with more fully condensed (and consequently denser) films at higher annealing temperatures. Loss tangents were below 0.6% in all cases, demonstrating low deviation from ideal capacitive behavior. MIS devices were re-examined after 10 months of

exposure to ambient air. Samples annealed at 300 °C showed slight decreases in dielectric constants and increased loss tangents, while films annealed ≥ 400 °C were stable and exhibited no change.

J-*E* measurements were conducted to assess the effectiveness of LZO as a viable gate dielectric material (Figure 3.7b). Increasing the annealing temperature resulted in lower

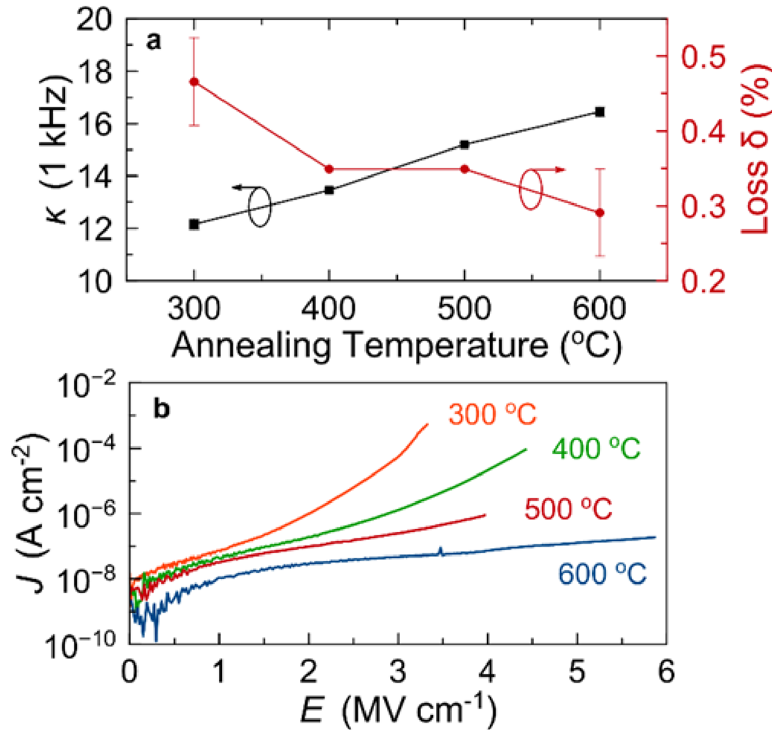

Figure 3.7. (a) Dielectric constants (κ) and loss tangents (loss δ), and (b) *J*-*E* data for MIS devices made from two-coat (~100 nm) LZO films.

leakage currents at all electric fields. This trend is consistent with trends of decreasing water and nitrate content (FTIR), increasing film densification (XRR), and low loss tangent values. LZO MIS devices generally experienced catastrophic breakdown and loss of insulating behavior at ~4 MV cm^{-1}. Stability of the LZO devices was tested by studying *J*-*E* hysteresis of successive cycles, as shown in Figure AA2. After an initial

burn-in sweep, it was observed that current density settled at 10^{-7}-10^{-8} A cm^{-2}. No discernable shift was observed in *J-E* behavior after the second sweep, indicating good stability. LZO films annealed ≥ 500°C have current density characteristics that meet or exceed those of other aqueous solution-deposited dielectric materials.[61,62,64–67]

Conclusion

An aqueous route to high-*κ* lanthanum zirconium oxide dielectrics using simple nitrate salts was reported. Residual nitrate and water species are fully removed from the films by 600 °C and the pyrochlore phase forms upon annealing to $T \geq 800$ °C. The remarkable smoothness of these films, the high dielectric constants with low deviations from ideal capacitive behavior, and low leakage currents make them promising gate components for thin-film transistor devices. Studies examining the effects of varying La:Zr composition on film properties and towards understanding density inhomogeneities (i.e., the less dense capping layer suggested by XRR modeling) are in progress.

Bridge

Chapter III detailed the preparation of ultrasmooth, dense, and uniform lanthanum zirconium oxide dielectric films from aqueous precursor solutions. These ternary films combined the advantageous dielectric properties of binary ZrO_2 and La_2O_3 while suppressing crystallization of ZrO_2 and mitigating carbonate and water absorption of La_2O_3. Complete characterization of thin film properties and evolution chemistry was achieved using multiple complementary analytical techniques, and the competitive device properties of lanthanum zirconium oxide were demonstrated.

Chapter IV builds on this initial study and makes use of the same aqueous route to explore ternary zirconium aluminum oxide dielectrics. This study takes advantage of the tunability offered by aqueous solution chemistry to investigate a complete range of Zr:Al compositions and corresponding film formation pathways and final properties.

CHAPTER IV

TUNABLE HIGH-κ $Zr_xAl_{1-x}O_y$ THIN FILM DIELECTRICS FROM ALL-INORGANIC AQUEOUS PRECURSOR SOLUTIONS

Authorship Statement

This chapter was previously published as a full article in *RSC Advances* in 2017 (volume 7, pages 39147-39152) and was coauthored by Keenan N. Woods, Emma C. Waddington, Connor A. Crump, Elizabeth A. Bryan, Tyler S. Gleckler, Michael R. Nellist, Brett A. Duell, Daniel P. Nguyen, Shannon W. Boettcher, and Catherine J. Page. The manuscript was written by K.N.W. with contributions from E.C.W. Editorial assistance was provided by S.W.B. and C.J.P. Experiments were performed by K.N.W., E.C.W., C.A.C., E.A.B., T.S.G., M.R.N., B.A.D., and D.P.N. with analysis done by K.N.W., E.C.W., and M.R.N.

Introduction

Metal oxide thin films function as critical components in a number of technological applications, including as gate dielectrics in transistors.[1,2] For these applications, amorphous high-κ materials are desirable for lowering power consumption and decreasing leakage current through the dielectric layer.[3] Zirconium oxide (ZrO_y)[4–14] and aluminum oxide (AlO_y)[15–33] are two high-κ materials that have been investigated as alternatives to SiO_2 gate dielectrics. ZrO_y has a high dielectric constant (~25) but is incompatible with the processing temperatures required for integrated circuit manufacturing.[3] This stems from an inherently low crystallization temperature (<500 °C),

which leads to grain boundaries and undesirable leakage currents.[34] Additionally, facile diffusion of oxygen through ZrO_y at elevated temperatures can result in uncontrolled interfacial growth at ZrO_2-Si interfaces.[3] Although AlO_y has a lower dielectric constant (~10), it remains amorphous until much higher temperatures (~800 °C) and exhibits high thermodynamic stability on Si.[3]

Previous reports of high-k zirconium aluminum oxide ($ZrAlO_y$, ZAO) thin film dielectrics indicate that Al incorporation can effectively suppress the crystallization of ZrO_y.[35–42] These reports utilized both vapor phase deposition routes (pulsed laser deposition[35,36] and atomic layer deposition[37,38]) and solution deposition routes (spray pyrolysis[39,40] and sol-gel[41,42]). Solution deposition routes are attractive because they generally employ inexpensive precursors and equipment, allow for facile variation of metal composition, and offer the promise of low-temperature processing.[43,44] However, the previously reported solution deposition routes to ZAO films make use of organic ligands and solvents, which are often difficult to remove and can result in carbon impurities that can adversely affect dielectric properties.[45,46] Only one previous study has investigated the effects of Zr:Al composition on dielectric properties. This study examined a limited composition range using a pyrosol method, but the authors were unable to establish a relationship between composition and dielectric properties.[39]

Herein, we report an all-inorganic aqueous solution deposition route to $Zr_xAl_{1-x}O_y$ (ZAO, $0 \leq x \leq 1$) thin films. This route is distinct from the previously employed solution deposition routes in that no organic ligands or additives are employed. This all-inorganic aqueous synthetic approach has previously produced dense, ultra-smooth metal oxide dielectric films with a variety of metal components.[34,47–57] Aqueous solution deposition

allows for precise control of film composition through the facile manipulation of precursor stoichiometry,[58] which we exploit to investigate a complete range of Zr:Al compositions. The ZAO films prepared *via* this aqueous route are smooth, dense, and defect-free. Films annealed at temperatures ≤ 500 °C are amorphous when the Al content is ≥10%. Device testing of ZAO-based metal-insulator-semiconductor (MIS) capacitors shows that the dielectric and leakage current density characteristics can be systematically tuned by varying the Zr:Al composition. The facile control of film composition and corresponding electrical properties make ZAO films promising functional components for microelectronic applications.

Experimental

Precursor Solution Preparation

A 1.0 M Zr stock solution was prepared by adding $ZrO(NO_3)_2 \cdot xH_2O$ (Sigma Aldrich, 99%) to 18.2 MΩ cm Millipore H_2O heated to ~70 °C. The solution was stirred vigorously for 1 h at this temperature, then stirred overnight at room temperature (RT) to produce a stable solution. A separate 1.0 M Al stock solution was prepared by dissolving $Al(NO_3)_3 \cdot 9H_2O$ (Alfa Aesar, 98.0-102.0%) in 18.2 MΩ cm H_2O at RT and stirring vigorously for 1 h. Mixed ratio precursor solutions were prepared from the 1.0 M stock solutions for a range of Zr:Al ratios. The total metal concentration for all Zr:Al ratios was 1.0 M, and all solutions were filtered through a 0.45 μm PTFE syringe filter.

Thin Film Preparation

Si substrates (2 x 2 cm^2 squares) were sonicated in 5% Contrad-70 solution (Decon

Laboratories) at RT for 1 h followed by rinsing with 18.2 MΩ cm H_2O. Precursor solutions were deposited onto treated Si substrates through 0.2 μm PTFE filters and then spun at 3000 rpm for 30 s. For samples annealed at or below 500 °C, samples were immediately transferred to a hotplate at 50 °C. Samples were then ramped to 200, 300, 400, or 500 °C (12.5 °C min^{-1}) and held for 1 h. Stacked, two-coat films (used for FTIR, SEM, and impedance measurements) were annealed to 200, 300, 400, or 500 °C for 10 min between coats with a final anneal at the desired temperature for 1 h. The maximum temperature that the hotplates could achieve was 500 °C. Therefore, samples with a final annealing temperature > 500 °C were first ramped to 500 °C for 10 min on a hotplate (for each layer), cooled to RT, and then transferred to a box furnace, which was then ramped to the desired final annealing temperature and held for 1 h.

In the case of Al-rich ZAO films ($Zr_xAl_{1-x}O_y$ where $x \leq 0.15$), sonicated Si substrates were also subjected to a 10 min O_2/N_2 plasma etch using a PE-50 Benchtop Plasma Cleaner (Plasma Etch, Inc.) set to maximum power, followed by rinsing with 18.2 MΩ cm H_2O. Following deposition, these Al-rich samples were transferred to hotplates preheated to 150 °C instead of 50 °C. These modifications were necessary to ensure good substrate wettability and to prepare high-quality, Al-rich ZAO films. All other annealing parameters (ramp rate, final annealing time) were kept the same.

Precursor Solution Characterization

Bulk powders were prepared for thermogravimetric analysis (TGA) from 1.0 M precursor solutions that were dried at 50 °C for 12 h. TGA was done using a TA Instruments Q500A with a ramp rate of 5 °C min^{-1} under an N_2 atmosphere.

Thin Film Characterization

Fourier transform infrared (FTIR) spectra were collected using a Nicolet 6700 spectrometer in transmission mode. Samples were deposited on lightly doped double-sided polished p-type Si substrates and background subtraction was done using a spectrum collected from a blank Si substrate (heated to match the thermal processing of each measured sample).

X-ray reflectivity (XRR) and grazing incidence X-ray diffraction (GIXRD) measurements were performed using a Rigaku SmartLab diffractometer with a Cu Kα radiation source (40 kV, 44 mA). XRR data were modeled using Bede REFS v4.00 software package,[59] and film thickness and density were extracted from best fit models (see Appendix B).

Atomic force microscopy (AFM) images were collected using a Dimension ICON AFM (Bruker, USA) in tapping mode. Standard tapping mode probes were used (42 N m^{-1}, 320 kHz). Images were collected at a scan rate of 1 Hz with 384 lines and 384 measurements per line. Image processing was performed using NanoScope Analysis 1.50 software, and a first order flattening compensated for any sample tilt in each image.

Cross-sectional scanning electron microscopy (SEM) was done using a FEI Helios Dual Beam FIB (5.0 keV accelerating voltage, 86 pA current, immersion mode). Samples were coated with thermally evaporated Al prior to imaging to prevent charging effects.[60]

Device Fabrication and Testing

Metal-insulator-semiconductor (MIS) devices were prepared by thermally evaporating Al top contacts (0.013 cm^2, 100 nm thick) onto ZAO films deposited on

degenerately-doped n-type Si substrates (<0.005 Ω cm). Electrical contact to the Si substrate was achieved by physically scratching the film with a scribe and applying an In/Ga eutectic. Impedance measurements were taken using an Agilent 4284A Precision LCR meter at 0.1, 1, and 10 kHz with 500 mV oscillation amplitude. Batch-to-batch variations were evaluated by making three separate samples per annealing temperature and measuring impedance of five MIS devices per sample. A Keithley 2400 SourceMeter (0.2 V steps, 0.2 s delay) was used for current density-electric field (*J*-*E*) characterization. All MIS device testing was performed in ambient atmosphere in a dark environment.

Results and Discussion

The decomposition of bulk precursor powders to the corresponding oxides was investigated by TGA (Figure 4.1). Mass loss events can be related to the elimination of water and nitrate counterions from the bulk precursor powders (Figure 4.1a). The temperatures at which significant mass loss occurs can be better visualized by examining the mass loss derivatives (Figure 4.1b). In the case of the ZrO_y precursor, gradual mass loss is observed between 50 and 150 °C (predominately water loss) followed by two large mass loss events between 150 °C and 250 °C (predominantly nitrate loss). Above 250 °C there is gradual mass loss (further water and nitrate loss) until ~500 °C when final densification and crystallization occurs. In contrast, the AlO_y precursor fully condenses and densifies at a much lower temperature, and mass loss appears to be complete by ~350 °C with the largest mass losses occurring between 50 and 200 °C.

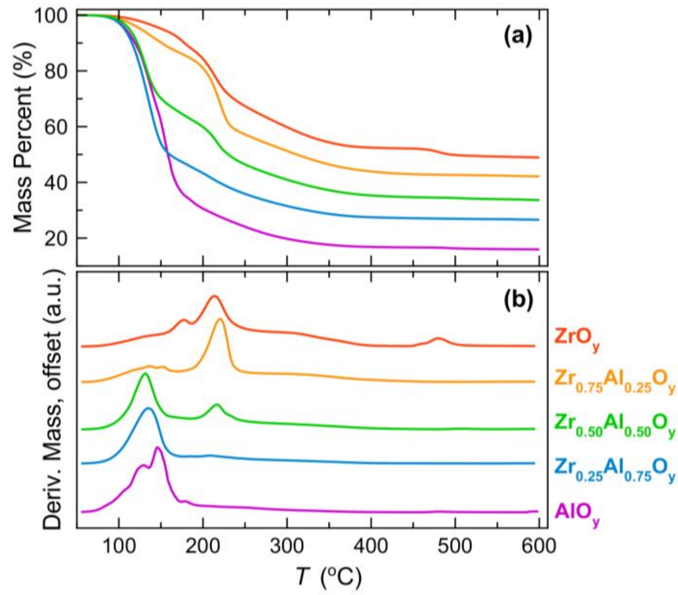

Figure 4.1. (a) Mass loss percent and (b) derivative of mass loss (absolute values) as a function of annealing temperature for bulk ZAO precursor powders.

For the mixed ZAO precursor powders, increasing the Al content decreases both the decomposition temperature and the resulting oxide formation temperature. This trend is not surprising as it is known that metal nitrate decomposition temperatures decrease with increasing metal cation charge density.[61] The higher charge density of Al^{3+} polarizes the nitrate ions, weakening N-O bond strengths and lowering decomposition temperatures for the Al-rich films.

TGA provides insight into the decomposition of the bulk precursor powders, but these measurements do not necessarily relate to the corresponding evolution of thin films due to differences in sample geometry, mass transport, and evaporation rates.[62,63] Nevertheless, TGA is useful for providing approximate temperature ranges at which decomposition events take place and for correlating how these change with metal composition.

FTIR allows a direct measurement of water and nitrate content in ZAO films as a function of annealing temperature (Figure 4.2). These spectra indicate that significant water (~3500 cm^{-1})[64] and nitrate (~1280 and 1460 cm^{-1})[31,65] are retained in films annealed at 200 °C (Figure 4.2a). Al-rich films generally contain less nitrate, consistent with TGA data of bulk powders. Water is fully removed from films of all compositions by 400 °C (Figure AB1), and nitrate is effectively removed by 500 °C (Figure 4.2b).

Peaks indicative of Al-O (~600 to 900 cm^{-1})[31] and Zr-O (~415 cm^{-1})[41] are observed for the pure AlO_y and ZrO_y films, respectively. The intensity of these peaks increases for films annealed at higher temperatures, indicating oxide formation is more complete. Significant overlap and broadening of the metal oxide peaks makes identification of Al-O and Zr-O peaks in the mixed composition samples difficult.[41] The loss of water and nitrate, coincident with growth of the oxide peak intensities, suggest that condensation is largely complete by 500 °C. XRR studies (which allow measurement of film thickness and density) also show that densification is complete by 500 °C (Figure AB2 and AB3).

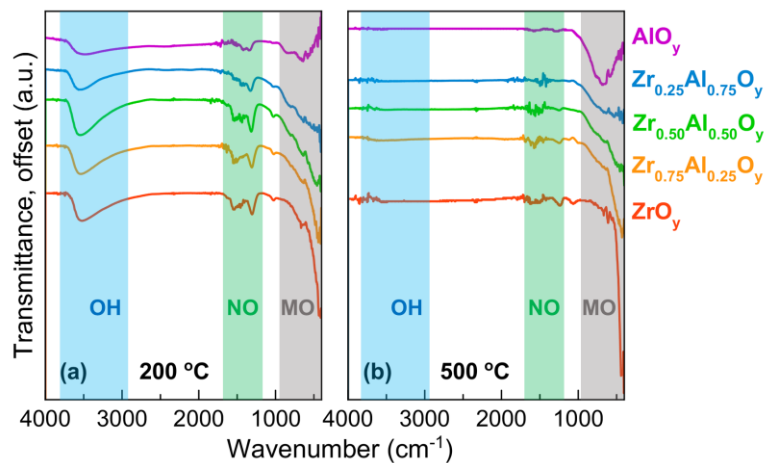

Figure 4.2. FTIR spectra of two-coat ZAO films annealed at (a) 200 °C and (b) 500 °C. FTIR spectra of ZAO films annealed at 300 and 400 °C can be found in Figure AB1.

As discussed above, amorphous metal oxides are preferred for gate oxide applications because grain boundaries in polycrystalline films negatively impact device performance.[3,34] The extent of crystallization as a function of Zr:Al composition and annealing temperature was investigated using GIXRD (Figure 4.3a,b). All compositions were amorphous at 400 °C, while ZrO_y is crystalline by 500 °C. ZAO films with compositions of ≥ 25% Al are amorphous at 500 °C and remain so up to 600 °C. The minimum amount of Al needed to prevent crystallization at 500 °C was 10% Al, although these films crystallize by 600 °C.

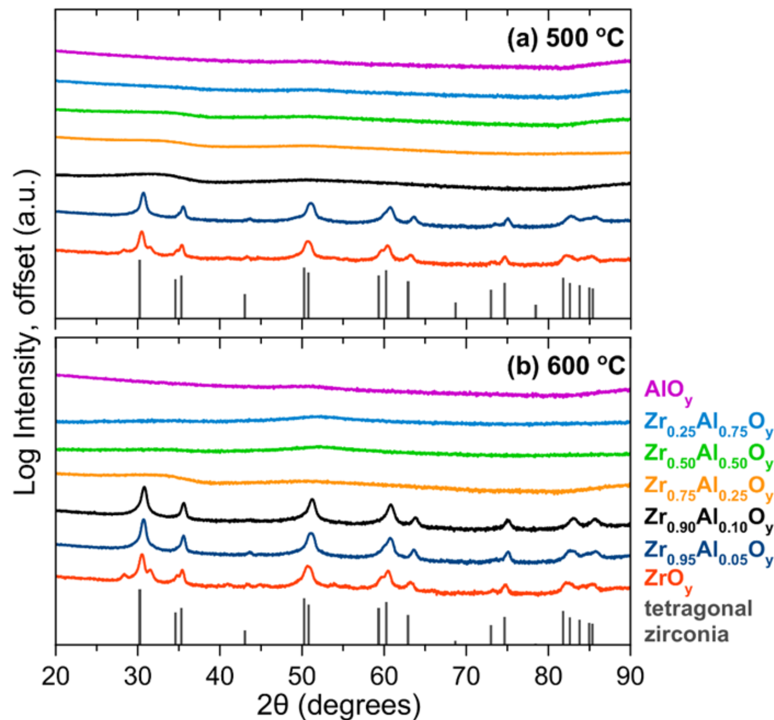

Figure 4.3. GIXRD of single-coat ZAO films annealed at (a) 500 °C and (b) 600 °C. The tetragonal zirconia phase (ICSD 66781)[66] is plotted for reference.

For many microelectronic applications, subnanometer surface roughness is essential for optimum device functionality.[67–69] AFM shows ZAO films annealed at 500 °C (Figure

4.4) are remarkably smooth (root-mean-square roughness (R_{rms}) < 1 nm). AlO_y films, in particular, are exceptionally smooth with $R_{\mathrm{rms}} \approx 0.1$ nm (Figure 4.4a). ZAO films with varying Zr:Al ratios are still quite smooth with $R_{\mathrm{rms}} \approx 0.2$-$0.4$ nm (Figure 4.4b-e).

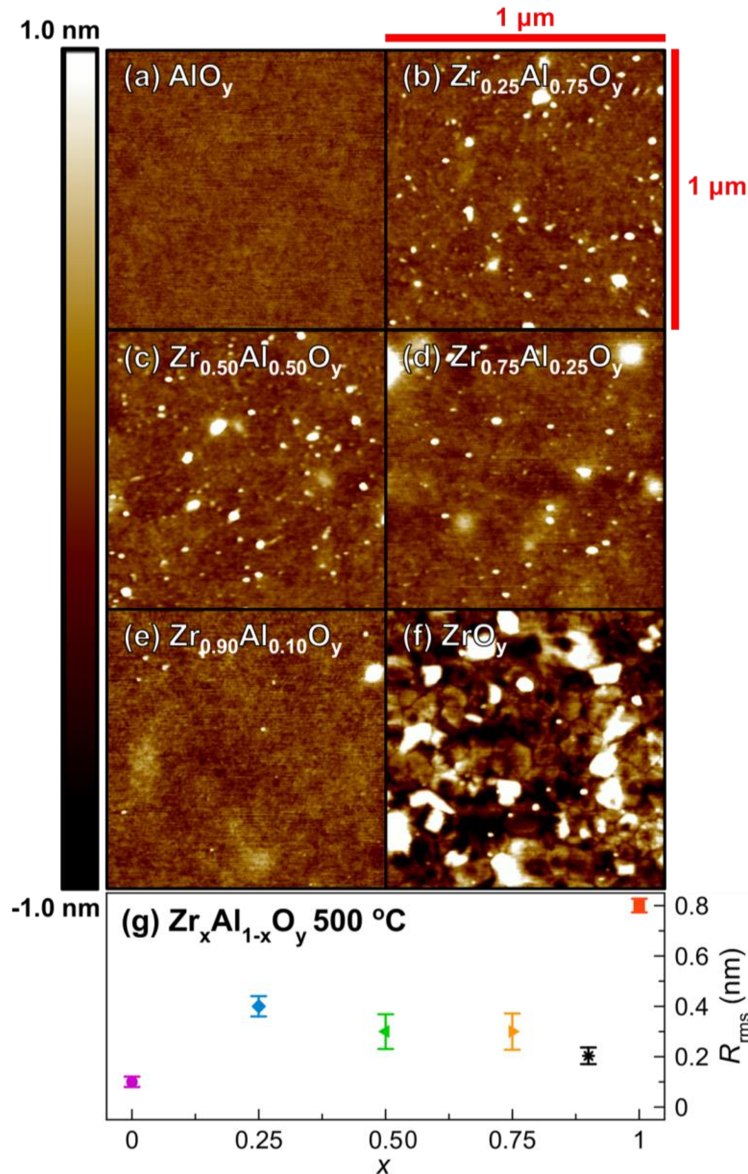

Figure 4.4. Representative AFM images of single-coat (a) AlO_y, (b) $Zr_{0.25}Al_{0.75}O_y$, (c) $Zr_{0.50}Al_{0.50}O_y$, (d) $Zr_{0.75}Al_{0.25}O_y$, (e) $Zr_{0.90}Al_{0.10}O_y$, and (f) ZrO_y films annealed at 500 °C (1 μm^2 area) and (g) corresponding surface roughness values. Error bars were determined using measurements taken from three separate 1 μm^2 areas on the same film.

In contrast, ZrO_y films are significantly rougher ($R_{rms} \approx 0.8$ nm). This increased roughness is likely associated with crystallization observed by GIXRD; indeed, crystallites are apparent in AFM images (Figure 4.4f).

Cross-sectional SEM shows the morphology of stacked, two-coat ZAO films incorporated into MIS devices (Figure 4.5). Amorphous ZAO films are dense and homogeneous, with no signs of interfacial roughness (Figure 4.5a-c). In the case of crystalline ZrO_y, large columnar grains are observed (Figure 4.5d).

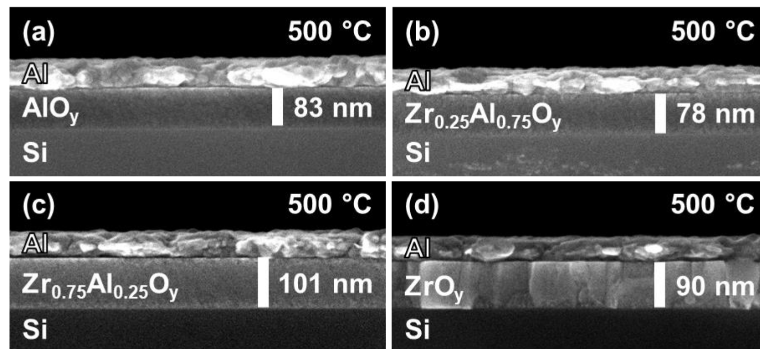

Figure 4.5. SEM cross-sectional images of two-coat (a) ZrO_y, (b) $Zr_{0.75}Al_{0.25}O_y$, (c) $Zr_{0.25}Al_{0.75}O_y$, and (d) AlO_y films annealed at 500 °C.

MIS devices were fabricated from two-coat ZAO films, and dielectric properties were examined by impedance spectroscopy (Figure 4.6 and Figure AB4). Dielectric constants (1 kHz) increase with increasing Zr content, ranging from 5.4 (AlO_y) to 18.6 (ZrO_y) for films annealed at 600 °C. We attribute the large increases in dielectric constants and batch-to batch variations for ZrO_y films annealed at 500 °C and $Zr_{0.90}Al_{0.10}O_y$ films annealed at 600 °C to the onset of crystallization (see Figure 4.4). Generally, loss tangents were low, indicating minimal deviation from ideal capacitance (Figure 4.6b).

Although it is difficult to directly compare properties of materials deposited using

different precursors and thermal treatments,[63] the dielectric constants reported here are within the range of values reported in the literature. In a previous sol-gel study, $Zr_{0.10}Al_{0.90}O_y$ films annealed between 250 and 350 °C for 2 h exhibited dielectric constants of 8.4 to 11.8.[42] Although these values are larger than those reported here, they compare well to dielectric constant of $Zr_{0.25}Al_{0.75}O_y$ films we prepared at 200 °C ($\kappa \approx 12$) and 300 °C ($\kappa \approx 10$). We do not include data for samples annealed at these low temperatures in Figure 4.6 because FTIR data (Figure 4.2 and AB1) indicate that these films contain residual polarizable water and nitrate, which can inflate dielectric constant values and lead to sample-to-sample variations.[53] In a separate ultrasonic spray pyrolysis study, ZAO films with similar compositions and annealing temperatures (475 °C) are also in the range of those reported here.[39]

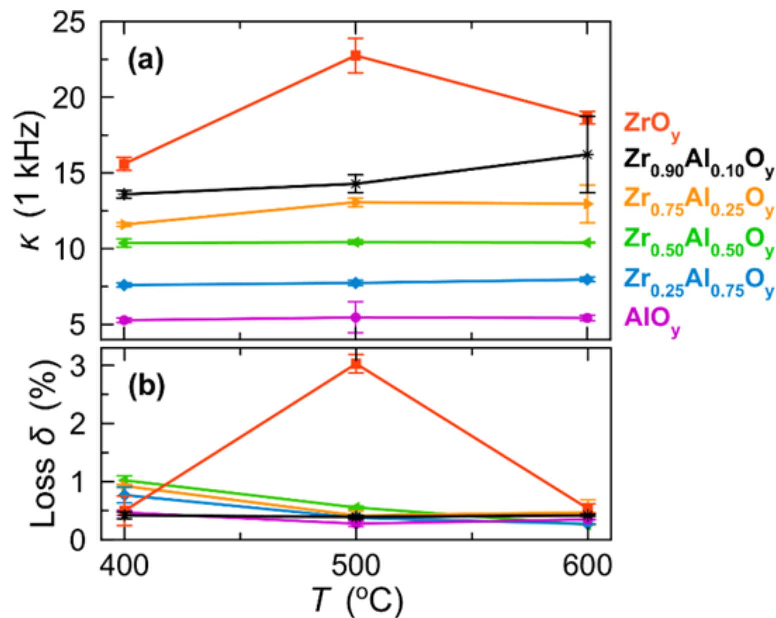

Figure 4.6. (a) Dielectric constants (κ) measured at 1 kHz and (b) corresponding loss tangents (loss δ) for MIS devices fabricated from two-coat (~100 nm) ZAO films annealed at various temperatures. Error bars were determined using measurements taken from three separate batches of devices. A plot of κ and loss δ as a function of frequency for ZAO-based MIS devices fabricated at 500 °C can be found in Figure AB4.

J-E measurements were conducted to assess the effects of Zr:Al composition on breakdown fields and leakage current densities of ZAO-based MIS devices processed at 500 °C (Figure 4.7). In general, $Zr_xAl_{1-x}O_y$ devices experience catastrophic breakdown (defined as $I > 100$ mA) and loss of insulating behavior at lower electric fields when $x \geq 0.90$ (2.0 to 2.5 MV cm^{-1}). In addition to lower breakdown voltages, batch-to-batch variation for $Zr_{0.90}Al_{0.10}O_y$ devices was high, suggesting the formation of microcrystallites beneath the detection limit of GIXRD for these films. In contrast, devices fabricated from more Al-rich $Zr_xAl_{1-x}O_y$ films ($x \leq 0.25$) experience breakdown at higher electric fields (~3 MV cm^{-1}), with AlO_y devices breaking down at ~3.7 MV cm^{-1}.

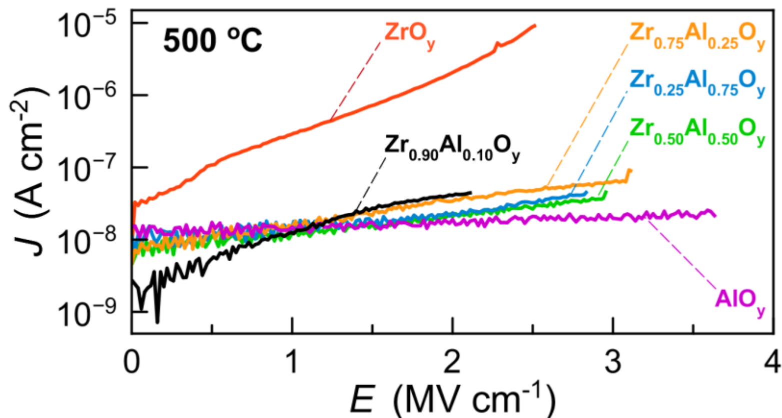

Figure 4.7. Representative *JE* data for MIS devices made from two-coat ZAO films (~100 nm) annealed at 500 °C.

Additionally, ZrO_y-based MIS devices display the highest leakage current densities at all electric fields, in agreement with the relatively high loss δ measured for ZrO_y-based devices annealed at 500 °C (Figure 4.6b). We attribute this to the formation of crystallites and the presence of grain boundaries in films annealed at this temperature.[34] Notably, incorporation of Al significantly decreases the leakage current densities of ZAO-based

devices at all electric fields. $Zr_xAl_{1-x}O_y$ films with $0.25 \leq x \leq 0.90$ show similar low leakage current densities, while AlO_y films exhibit the lowest leakage current densities. Together, the MIS characterization suggests that $Zr_{0.75}Al_{0.25}O_y$ displays the optimal balance of a high dielectric constant and low leakage current densities.

Conclusion

We report an all-inorganic aqueous deposition route to variable composition high-κ zirconium aluminum oxide films with subnanometer surface roughness and tunable properties. Residual nitrate and water are fully removed from ZAO films by 500 °C, and incorporation of Al ≥10% effectively suppresses crystallization of the tetragonal zirconia phase up to 500 °C. Dielectric constants increase with increasing Zr content, and films with Al >10% exhibit low leakage current densities. For the composition range studied, the combination of high dielectric constant and low leakage current densities makes $Zr_{0.75}Al_{0.25}O_y$ a promising candidate for microelectronic applications.

Bridge

In Chapter IV, the impact of manipulating solution stoichiometry on thin film evolution chemistry and resulting thin film properties was investigated. Optimization of Zr:Al composition produced amorphous zirconium aluminum oxide dielectrics with excellent morphologies and competitive device performances.

Both Chapters III and IV demonstrate the versatility and utility of all-inorganic aqueous approaches for preparing ultrasmooth, dense, and uniform metal oxide thin films. However, elevated processing temperatures (≥400 °C) were required to fully

decompose and remove residual counterions and solvent, which is a common issue for solution-deposited materials. Generally, films processed at low annealing temperatures also suffer from significant water absorption from the ambient after annealing, which prevents their use in functional microelectronic devices. Chapter V discusses a method for lowering processing temperatures by adding water to the annealing atmosphere. This steam annealing method effectively improves counterion removal, resistance to water absorption, and dielectric properties of aqueous-derived metal oxide thin films.

CHAPTER V

LOW-TEMPERATURE STEAM ANNEALING OF METAL OXIDE THIN FILMS FROM AQUEOUS PRECURSORS: ENHANCED COUNTERION REMOVAL, RESISTANCE TO WATER ABSORPTION, AND DIELECTRIC CONSTANT

Authorship Statement

This chapter was previously published as a full article in *Chemistry of Materials* in 2017 (volume 29, pages 8531-8538) and was coauthored by Keenan N. Woods, Paul N. Plassmeyer, Deok-Hie Park, Lisa J. Enman, Aidan K. Grealish, Brenna L. Kirk, Shannon W. Boettcher, Douglas A. Keszler, and Catherine J. Page. The manuscript was written by K.N.W. and P.N.P. (equal contributions) with additional contributions from D.-H.P. and L.J.E. Editorial assistance was provided by S.W.B., D.A.K., and C.J.P. Experiments were performed by K.N.W., P.N.P., D.-H.P., L.J.E., A.K.G., and B.L.K.

Introduction

Metal oxide thin films function as critical device components in a wide range of electronic and renewable energy technologies. The need for high-volume manufacturing has fueled interest in new deposition methods with capabilities to produce complex compositions, control morphologies, and increase throughput. In particular, solution deposition presents a potentially scalable, inexpensive route to address these demands.[1–7] Sol-gel and similar metal-organic methods, which utilize organic ligation to form stable solutions and control condensation reactions, currently dominate solution deposition.[4–16]

In contrast, inorganic aqueous solution deposition avoids organic additives and solvents, instead employing simple metal salts or precondensed oxo-hydroxo metal clusters to produce dense films with ultrasmooth surfaces.[2,17–38]

In both sol-gel and aqueous solution deposition techniques, water plays an important role in the film formation process. For example, sol-gel metal alkoxide precursors must hydrolyze to metal hydroxides before they condense to form a metal oxide network.[39–42] Consequently, water vapor aids in the conversion of sol-gel precursors to corresponding oxide films.[5,43,44] Similarly, Zn acetate and acetylacetonate salts react with steam to produce crystalline ZnO.[45,46]

Researchers are only beginning to examine the general effects of humidity on the formation of oxide films deposited from aqueous metal salts and oxo-hydroxo metal clusters. We recently showed, for example, that water vapor in the spin-coating chamber dramatically affects film thickness, i.e., during the coating process alone.[47] Specifically, we found film thickness increases with decreased solvent evaporation rate and increased viscosity, independent of solute identity. This effect is a physical phenomenon based on the properties of water as a solvent. We expect humidity will play a chemical role during thermal processing, where water will affect counterion loss, condensation pathways, and film morphology. For example, water forms azeotropes with both nitric and hydrochloric acids, so the presence of water in the annealing atmosphere may enhance the removal of nitrate and chloride counterions, respectively, via azeotropic evaporation. Indeed, we have observed that exposure of bulk scandium oxo-hydroxo nitrate powders to steam removes nitrate at temperatures well below its decomposition temperature.[48]

In this study, we demonstrate that introducing steam to the annealing ambient significantly reduces residual counterions in zinc oxide, yttrium aluminum oxide, and lanthanum zirconium oxide (LZO) films deposited from aqueous nitrate precursors. We then present a detailed study on the effects of steam annealing on the chemical, physical, and electrical properties of amorphous LZO dielectric films. We find that in addition to reducing residual counterion concentrations, steam annealing enhances resistance to water absorption, prevents void formation in chloride-containing films, and increases the dielectric constant of LZO films in metal-insulator-semiconductor (MIS) devices. Combined, the results from this study demonstrate the pronounced impact of steam in the annealing ambient on the chemical evolution, morphology, and electrical properties of thin films deposited from aqueous precursors.

Experimental

Precursor Solution Preparation

All precursor solutions were prepared by dissolving metal nitrate or metal chloride salts in 18.2 MΩ cm Millipore H_2O. Lanthanum zirconium oxide (LZO) precursors were prepared as 0.5, 1.0, 1.5, or 1.8 M (total metal, 1:1 La:Zr) solutions. Solutions were prepared from all NO_3^- precursors [$La(NO_3)_3 \cdot 6H_2O$ (Alfa Aesar, 99.9%) and $ZrO(NO_3)_2 \cdot xH_2O$ (Sigma-Aldrich, 99%)] or mixed NO_3^-/Cl^- precursors [$La(NO_3)_3 \cdot 6H_2O$ (Alfa Aesar, 99.9%) and $ZrOCl_2 \cdot 8H_2O$ (Sigma-Aldrich, 99%)]. ZnO precursor solutions were made using $Zn(NO_3)_2 \cdot 6H_2O$ (Sigma-Aldrich, ≥ 99.0%), and yttrium aluminum oxide (YAO, 3:5 Y:Al) precursor solutions were made using $Y(NO_3)_3 \cdot 6H_2O$ (Strem,

99.9%) and $Al(NO_3)_3•9H_2O$ (Alfa Aesar, 98.0-102.0%). All solutions were filtered through 0.45 μm PTFE syringe filters.

Thin Film Preparation

Si substrates (2 x 2 cm^2) were sonicated in 5% Decon Laboratories Contrad-70 aqueous solution for 5 min, thoroughly rinsed with 18.2 MΩ cm Millipore H_2O, and spin-dried using a spin-coater. Substrates were then exposed to a 1 min O_2/N_2 plasma etch using a Plasma Etch, Inc. PE-50 Benchtop Plasma Cleaner set to maximum power. Substrates were then rinsed with 18.2 MΩ cm Millipore H_2O and spin-dried before film deposition. This treatment ensured a hydrophilic substrate surface for good solution wetting.[49] Samples prepared for Fourier transform infrared (FTIR) spectroscopy and temperature programmed desorption (TPD) analysis were deposited on lightly doped double-side polished p-type Si substrates. Samples for TPD analysis were deposited on 1 x 1 in^2 substrates and physically cleaved into 1 x 1 cm^2 samples after annealing.

Precursor solutions were filtered through a 0.2 μm PTFE syringe filter onto pretreated Si substrates and spin-cast at 3000 rpm for 30 s. Samples were then immediately transferred to a pre-heated heating stage at 125 °C, held for ~15 s, and annealed under either a “dry” or “humid” annealing atmosphere. Dry-annealed samples were annealed on a custom-built hot plate under ambient laboratory atmosphere (~45% relative humidity at room temperature). Steam-annealed samples were annealed in a tube furnace equipped with a removable heating stage and a water vaporizer (Scheme AC1). Both hot plate and heating stage were equipped with a PID controller for precise control of annealing

temperature and ramp rate. All samples were annealed using a 25 °C min^{-1} ramp rate, unless otherwise noted. Samples were heated at their final annealing temperature for 1 h.

Thin Film Characterization

Water and residual counterion content was probed via FTIR and TPD analysis. FTIR spectra were collected using a Thermo Fisher Nicolet 6700 spectrometer. Background subtraction was performed using the spectra collected from bare Si substrates with the same thermal history as each sample. TPD analysis was conducted using a TPD Workstation (Hiden Analytical) with a quadrupole mass analyzer (3F PIC, Hiden Analytical). Samples were heated from room temperature to 550 °C (30 °C min^{-1}) under ultrahigh vacuum (base pressure $< 5 \times 10^{-9}$ Torr). Electron-impact ionization (EI) mass spectra were acquired with a 70 eV ionization energy and 20 µA emission current. Selected mass-to-charge (m/z) ratios (m/z 30, 32, and 35 for NO, O_2, and Cl desorption, respectively) for each sample were monitored in multiple ion detection (MID) mode with a dwell time of 200 ms and a settle time of 50 ms.

Atomic force microscopy (AFM) studies were done using a Dimension ICON AFM (Bruker, U.S.A.) in tapping mode with standard tapping mode probes (42 N m^{-1}, 320 kHz). Images were collected at a scan rate of 1 Hz with 512 lines and 512 measurements per line. NanoScope Analysis 1.50 software was used to calculate root-mean-square roughness (R_{rms}) and to correct for sample tilt in each image by applying a first order flattering.

X-ray photoelectron spectroscopy (XPS) was performed using an ESCALAB 250 (Thermo Scientific) with an Al Kα monochromated source (150 W, 20 eV pass energy,

500 μm spot size). Samples were grounded to the metallic sample holder with a metal clip and charge-neutralized using an electron flood source. The binding energy scale was calibrated using the C-H adventitious C 1s peak at 284.8 eV. Spectra were analyzed using Thermo Scientific Avantage 5.94 software with a linear background. A detailed description of the peak fitting analysis can be found in Appendix C.

Cross-sectional scanning electron microscopy (SEM) using a FEI Helios Dual Beam FIB was conducted on samples coated with thermally evaporated Al to prevent charging during imaging (5.0 keV accelerating voltage, 86 pA current).[50]

Grazing incidence X-ray diffraction (GIXRD) was performed using a Rigaku SmartLab diffractometer with a Cu Kα radiation source (40 kV, 44 mA).

Device Fabrication and Testing

MIS devices were fabricated from two-coat LZO (NO_3^-) films (~100 nm) deposited on degenerately doped n-type Si substrates (<0.005 Ω cm). Al top contacts (0.013 cm^2, 100 nm thick) were thermally evaporated onto the stacked LZO films through a shadow mask. Electrical contact to the Si substrate was achieved by scratching through the film to the substrate with a scribe and applying an In/Ga eutectic. Dielectric constants and loss tangents were calculated from impedance measurements taken with an Agilent 4284A Precision LCR meter (1 kHz, 500 mV oscillation amplitude). Three separate samples per annealing temperature were fabricated and tested to evaluate batch-to-batch variations. Current density-electric field (*J-E*) characterization was done using a Keithley 2400 SourceMeter (0.2 V steps, 0.2 s delay). All device testing was conducted in a dark environment under ambient atmosphere.

Results and Discussion

Impact of Steam Annealing on Bulk Chemistry

FTIR spectra (Figure 5.1) demonstrate steam annealing at 200 °C significantly reduces residual nitrate in LZO films, as evidenced primarily by a decrease in the intensities of the 1280 and 1460 cm^{-1} nitrate bands.[51] This is true for LZO films derived from NO_3^- (Figure 5.1a) and NO_3^-/Cl^- precursors (Figure 5.1b). Additionally, bands at

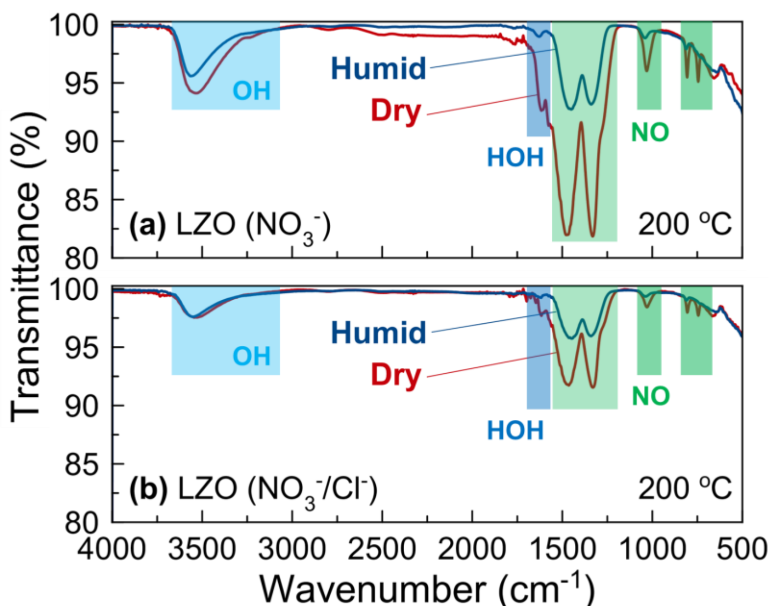

Figure 5.1. FTIR spectra of LZO films deposited from 1.8 M solutions derived from (a) NO_3^- precursors or (b) NO_3^-/Cl^- precursors. All films were annealed under humid (blue) or dry (red) conditions at 200 °C.

1000 and ~800 cm^{-1} (indicative of NO_3^- associated with hydrated metal species)[51,52] diminish under humid conditions. To determine whether this effect is specific to LZO films, we examined the effect of steam annealing on zinc oxide and yttrium aluminum oxide films spin-cast from aqueous NO_3^- precursors. FTIR studies reveal steam annealing also dramatically reduces residual NO_3^- content in these films (Figure AC1). We chose

these materials to compare with the LZO system because the metal components have very different hydrolysis and thermal decomposition profiles, and the impact of steam annealing on these disparate systems suggests steam annealing is a general method for removing nitrate from aqueous-derived films at low processing temperatures.

FTIR is unable to provide information on Cl^- content in films deposited from NO_3^-/Cl^- precursors. TPD allows mass spectral analysis of gases desorbed from a sample as it is heated and is sensitive enough to probe small volume samples, such as thin films. In the present case, we use TPD to measure residual nitrogen- and chlorine-containing species that evolve during the heating of a previously annealed film. Figure 5.2a shows a clear signal at m/z = 35 (Cl) from the 200 °C dry-annealed film. In contrast, the film annealed under steam desorbs no Cl, indicating that steam annealing at 200 °C effectively removes Cl to below the detection limit of TPD.

Figure 5.2b shows desorption of NO from dry- and steam-annealed films, and Figure 5.2c shows O_2 desorption in the same experiment. We associate these signals with thermally induced NO_3^- decomposition because the NO and O_2 signals overlap in the two spectra.[53,54] The significant signal reductions between 300 and 400 °C for the humid-annealed films demonstrate the effectiveness of steam for reducing NO_3^- content, and is consistent with trends observed by FTIR (see Figure 5.1). We propose the two distinct mass loss events from ~250 to 450 °C and ~450 to 500 °C in the NO trace of the dry-annealed film indicate NO_3^- exists in at least two distinct chemical environments. The absence of NO and O_2 signals up to 400 °C for the steam-annealed film indicates steam annealing at 200 °C removes loosely bound NO_3^-. Additionally, reduced signals at higher temperatures indicate strongly bound NO_3^- partially desorbs during steam annealing.

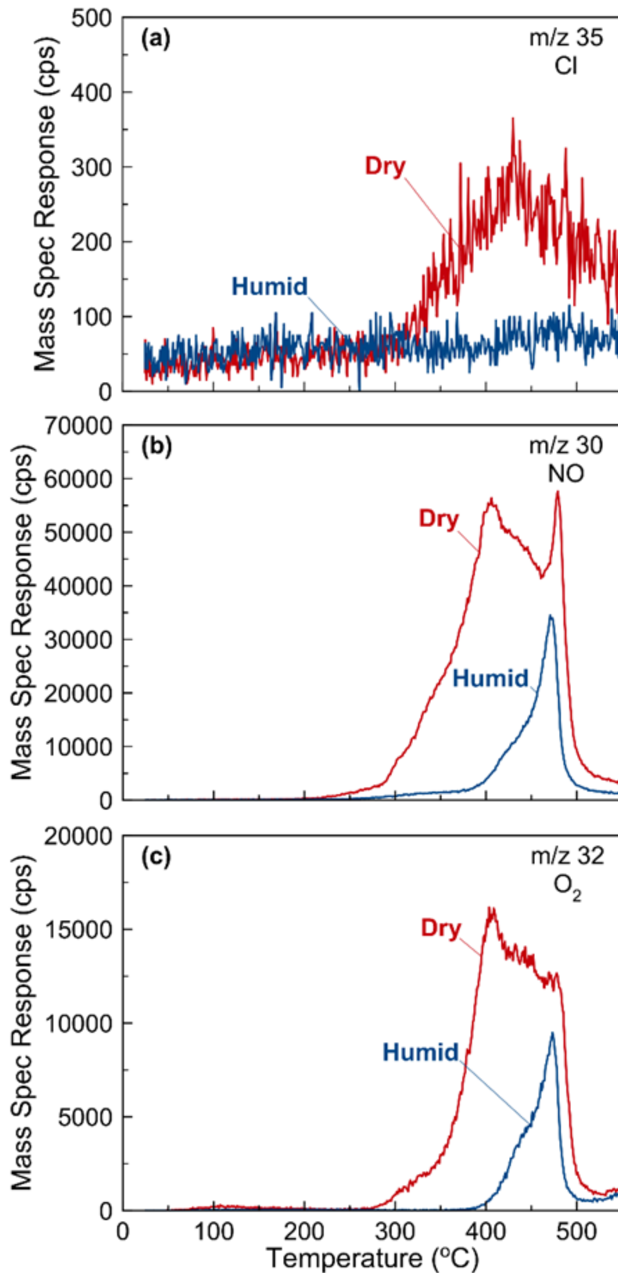

Figure 5.2. TPD data for dry- (red) and humid-annealed (blue) LZO films deposited from a 1.5 M solution (NO_3^-/Cl^- precursors) and annealed at 200 °C prior to TPD experiments: (a) m/z 35, (c) m/z 30, and (d) m/z 32.

In general, condensation (Eq. 5.1) of aqueous metal salt precursors requires the initial decomposition or chemical removal of counterions (Eqs. 5.2, 5.3) to produce hydroxide.

Eq. 5.1. $M\text{-}OH + HO\text{-}M \leftrightarrow M\text{-}O\text{-}M + H_2O$

Eq. 5.2. $M\text{-}NO_3 + H_2O \leftrightarrow M\text{-}OH + HNO_3$

Eq. 5.3. $M\text{-}Cl + H_2O \leftrightarrow M\text{-}OH + HCl$

These equations are general for oxide formation from metal salts, but different metals will undergo hydrolysis and condensation at different rates. Nevertheless, counterion removal effectively controls formation of M-O-M linkages.

The FTIR and TPD data indicate that steam annealing more effectively removes counterions from films prepared from aqueous metal salt precursors. We postulate a combination of factors controls and assists counterion removal under these conditions. First, Eqs. 5.2 and 5.3 shift to the left, as $H_2O(g)$ evolves from the films during dry anneals. This shift drives counterions to the inner coordination sphere of the metal cation. These strongly bound counterions decompose and evolve at high temperatures. In contrast, Eqs. 5.2 and 5.3 shift to the right under steam annealing, which generates counterions loosely bound in matrices of hydrogen bonds that are ostensibly easier to remove. Indeed, a recent report suggests increased inner-sphere hydration of metal cations reduces film processing temperatures.[25]

Second, counterions may evaporate as HNO_3/H_2O and HCl/H_2O azeotropes (68% HNO_3/32% H_2O and 20% HCl/80% H_2O, which boil at 120 and 110 °C, respectively). Azeotropic evaporation shifts the equilibria of Eqs. 5.2 and 5.3 to form metal hydroxides that may then condense via Eq. 5.1. A vapor pressure of water above the film surface promotes azeotrope formation and provides an alternative to thermal decomposition, allowing low-temperature removal of counterions.[48]

Impact of Steam Annealing on Water Absorption

Many solution-processed films absorb water readily after thermal processing,[55] but the literature rarely comments on this water resorption. Lanthanum-containing films are particularly prone to water absorption.[56–58] We observe that 200 °C dry-annealed LZO films become visibly hazy 15 to 60 min after removal from a heated hot plate (Figure AC2). In contrast, we observe no changes for films annealed under steam at the same temperature, and they retain their visual appearance for weeks in air at room temperature. AFM studies indicate that the visible changes in the dry-annealed films are associated with an increased surface roughness from 0.2 to 3.3 nm (Figure AC3). Because of these effects, we made the measurements described above immediately after the annealing step.

To determine the cause of the instability observed for dry-annealed films, we compared FTIR spectra of dry- and humid-annealed films taken immediately after annealing at 200 °C and again after a 1 h exposure to air. Figure 5.3 shows that air exposure does not significantly affect the humid-annealed film; notably, the OH band near 3500 cm^{-1} changes little. In contrast, the OH band of the dry-annealed film increases dramatically after air exposure, indicating significant water absorption.

Differences in surface chemistry may account for the enhanced resistance of steam-annealed films to water absorption. Indeed, a dense capping layer can act as an effective diffusion barrier to water.[55,59] We examined the surface chemistry of LZO films (NO_3^-/Cl^- precursors) annealed under humid and dry conditions with XPS. XPS spectra of films annealed at 200 °C (Figure AC5, Tables AC1 and AC2) show that dry-annealed films contain significantly more N from residual NO_3^- (consistent with FTIR and TPD). However, both dry- and steam-annealed films retain considerable nitrate at this annealing

temperature, complicating peak fitting of the O 1s spectra. Additionally, the hygroscopic nature of dry-annealed films results in sample-to-sample variations. For these reasons, we also studied LZO films annealed under both atmospheres at 500 °C (Figures 5.4 and AC6, Table 5.1 and AC3). Nitrates are completely removed at this annealing temperature, allowing for more reliable O 1s peak fitting and a more detailed analysis of surface chemistry. Additionally, water absorption is not an issue at this annealing temperature, and samples remain amorphous by GIXRD (Figure AC7).

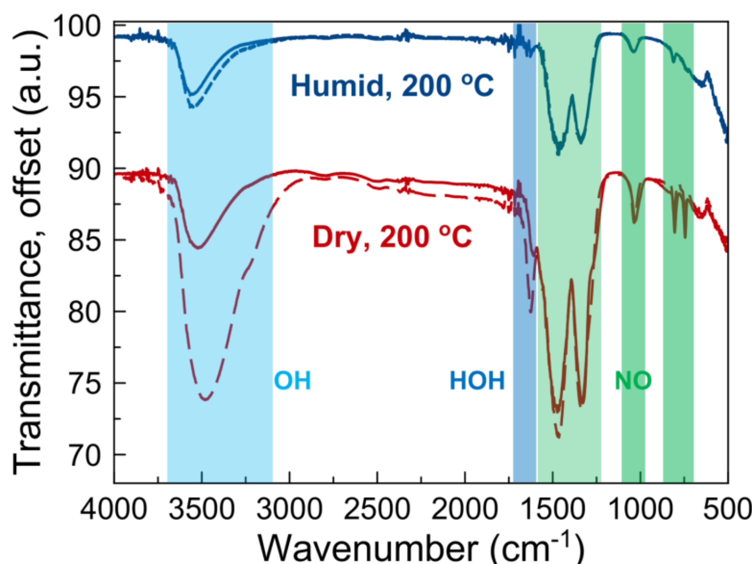

Figure 5.3. FTIR spectra of LZO films deposited from a 1.8 M solution (NO_3^-/Cl^- precursors) and annealed under dry (red) or humid (blue) conditions at 200 °C. Solid lines are data taken immediately after annealing and dashed lines are data taken after 1 h in ambient lab air (~45% relative humidity). See Figure AC4 for similar FTIR stability data for LZO (NO_3^-) films.

Figure 5.4 shows C 1s, O 1s, and La 3d spectra for LZO films (NO_3^-/Cl^-) annealed at 500 °C, and Table 5.1 shows the atomic percentages from the C 1s and O 1s spectra peak fitting. The peak fitting indicates LZO films contain carbonate near the film surface. A higher concentration of carbonate exists in dry-annealed films (~4%) compared to humid-

annealed films (~1%). Carbonate near the film surface likely arises from CO_2 adsorption, which is known to occur for lanthanum oxides.[57,60] Comparison of the ratios of O and C attributed to carbonate from peak fitting provides further insight. For the dry-annealed sample, the relevant O:C ratio is ~2.7, which is similar to the expected 3:1 O:C ratio of CO_3^{2-}. In the case of the humid annealed sample, the O:C ratio is ~7.7, significantly higher than the O:C ratio expected for CO_3^{2-}. Lanthanum oxides also absorb H_2O from the atmosphere to form lanthanum hydroxide,[56] so it is possible that steam-annealed films contain significant OH at the film surface. Because OH has a similar O 1s binding energy range to CO_3^{2-} (530.8 to 532 and 530.5 to 531.5 eV, respectively[61]), the presence of OH could account for the anomalously high O:C ratio in the humid-annealed sample. The intensity ratio of the multiplet-split La $3d_{3/2}$ and La $3d_{5/2}$ peaks further supports enhanced OH content in the steam-annealed films; the shape of these peaks more closely resembles pure $La(OH)_3$ than pure La_2O_3 for the steam-annealed sample.[62]

XPS also shows nitrate is completely removed from films annealed under both atmospheres at 500 °C, but that dry-annealed films retain a small amount of Cl (~1%, Figure AC6, Table AC3). This is consistent with XPS for films annealed at 200 °C (Figure AC5, Table AC2), which shows that both Cl and N content of steam-annealed films are significantly reduced relative to dry-annealed films.

From the XPS and FTIR data, it is clear that steam annealing diminishes residual counterion concentrations and effectively limits water resorption. There are two potential explanations for these effects. First, many metal nitrate and chloride salts are hygroscopic. Steam-annealed films may be less hygroscopic simply because they contain fewer residual counterions. Second, the enhanced removal of counterions via steam

annealing signifies that metal hydrolysis (Eqs. 5.2, 5.3) and subsequent condensation to the oxide (Eq. 5.1) are more complete. Generally, we observe that steam annealing produces ~10% thinner (and presumably denser) films relative to dry annealing. Increased metal oxide condensation and densification would presumably impede water

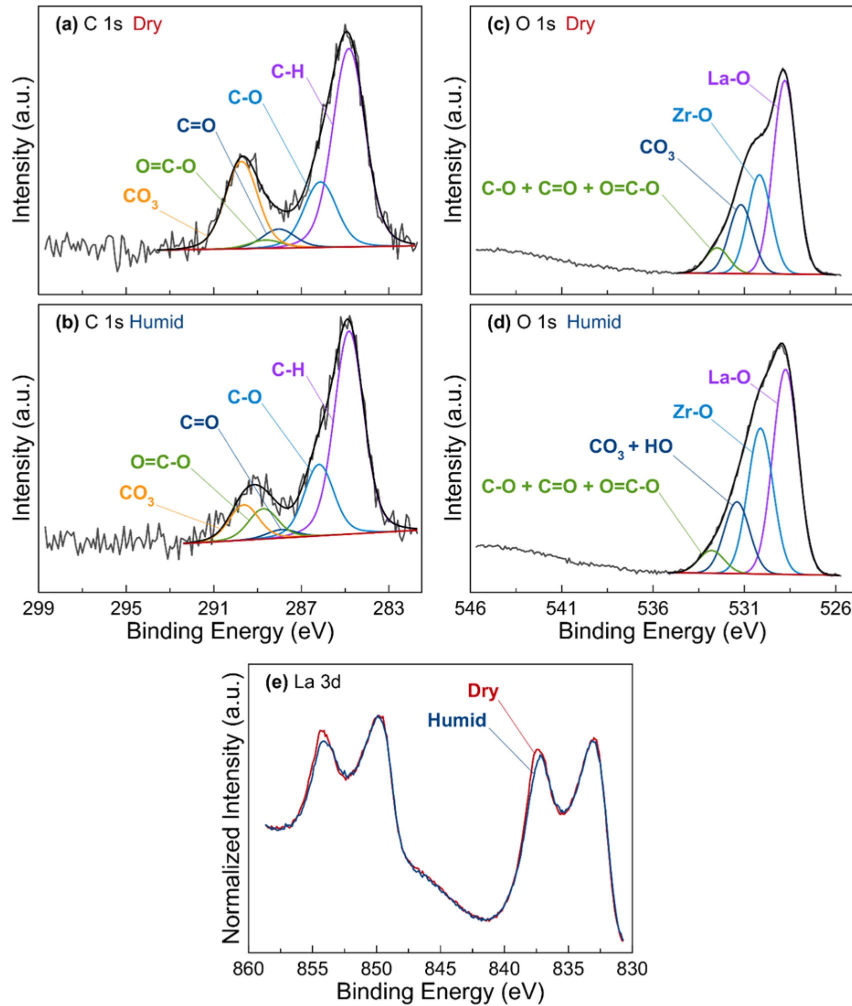

Figure 5.4. XPS spectra of films deposited from a 1.0 M solution (NO_3^-/Cl^- precursors) and annealed under dry or humid conditions at 500 °C. The C 1s (a, b) and O 1s (c, d) data were fit using Avantage peak fitting software, and raw data are shown in gray, envelope peak fits are shown in black, and linear backgrounds are shown in red. Individual fit peaks corresponding to specific C or O species are labeled and color-coded. Overlaid La 3d data (e) are color-coded red and blue for films annealed under dry and humid conditions, respectively.

absorption. This explanation for the enhanced resistance to water absorption is consistent with previous reports that show a dense oxide capping layer prevents H_2O absorption in water-sensitive oxides.[55,59,63]

Table 5.1. C and O Atomic Percentages from XPS Peak Fitting Shown in Figure 5.4a-d (see Table AC3 for a complete list of atomic percentages).

C Species	At. % Dry	At. % Humid	O Species	At. % Dry	At. % Humid
C-H	8.8	7.3	La-O	29.1	28.4
C-O	2.9	2.6	Zr-O	14.9	20.2
C=O	0.8	0.3	CO_3	10.4	-
O=C-O	0.4	1.1	CO_3 + HO	-	10.0
CO_3	3.9	1.3	C-O + C=O + O=C-O	3.8	3.2

Impact of Steam Annealing on Morphology

Further studies reveal a surprising impact of annealing atmosphere on film morphology. The cross-sectional SEM image in Figure 5.5a shows a dry-annealed LZO film (NO_3^-/Cl^-) contains large voids in the lower portion of the film and a nonporous, uniform surface region. A thin, continuous layer of material at the LZO-substrate interface indicates voids are not caused by dewetting of the precursor solution. In marked contrast, Figure 5.5b shows a humid-annealed LZO film (NO_3^-/Cl^-) is uniform and homogeneous, containing no voids. Interestingly, NO_3^- precursors produce uniform and homogeneous films regardless of annealing atmosphere (Figure AC8).

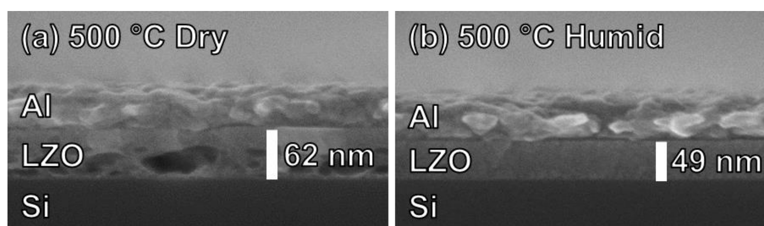

Figure 5.5. SEM images of LZO films deposited from a 1.5 M solution (NO_3^-/Cl^- precursors) and annealed at 500 °C under (a) dry or (b) humid conditions. See Figure AC8 for SEM images of LZO (NO_3^-) films.

Counterion loss during film formation requires thermal decomposition and/or diffusion to the film surface via a charge-compensated mechanism. These processes, however, compete with the densification of the oxide network. If the rate of densification exceeds those of counterion diffusion, decomposition, and desorption, then counterions, hydroxide, and water may form trapped bubbles within the films. Bubble collapse during continued annealing may then produce voids. We propose that for chloride ions, the rate of diffusion relative to densification is low under dry annealing, leading to entrapment and void formation. This explanation is consistent with the observation of residual Cl in dry-annealed films by TPD and XPS. In contrast, steam annealing affects the relative rates of diffusion and condensation, enhancing counterion removal and suppressing void formation.

To explore this hypothesis further, we conducted an additional SEM study to examine the importance of the relative rates of diffusion and densification in more detail. Specifically, we varied heating rates and the concentration of the precursor solutions (which determines film thickness[64]) to monitor void formation in dry-annealed (NO_3^-/Cl^-) films. Figure 5.6a-c shows SEM images of films prepared from different concentrations using a "standard" ramp rate of 25 °C min^{-1} to 500 °C. The thinnest film (~20 nm, from

0.5 M solution) exhibits no voids (Figure 5.6a). Thicker films (~40 and 70 nm, from 1.0 and 1.5 M solutions, respectively) contain voids near the substrate (Figure 5.6b,c). Curiously, each of these thicker films exhibits a dense, void-free surface region of ~20 nm, suggesting Cl species can diffuse from this depth to desorb as the film is forming. Species below this depth become trapped, forming voids.

We also examined the effect of ramp rates on film morphology for a fixed film thickness (Figure 5.6d-f). Films annealed at the slowest ramp rate (0.25 °C min^{-1}, Figure 5.6d) form the smallest voids, while films annealed at the fastest ramp rate (125 °C min^{-1}, Figure 5.6f) form the largest voids. Notably, the thickness of the dense, pore-free region

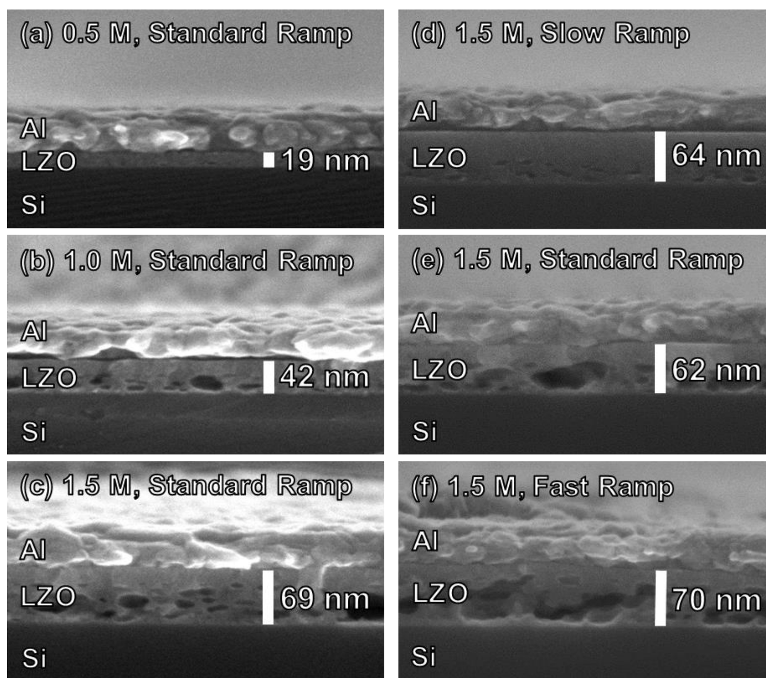

Figure 5.6. SEM images of LZO films deposited from (a) 0.5, (b) 1.0, or (c) 1.5 M solutions annealed using a standard (25 °C min^{-1}) ramp, and LZO films deposited from a 1.5 M solution and annealed using (d) slow (0.25 °C min^{-1}), (e) standard, or (f) fast (125 °C min^{-1}) ramps. All films were deposited from NO_3^-/Cl^- precursors and annealed under dry conditions at 500 °C.

at the top of each film increases with slower ramp rates. These observations indicate slow ramp rates allow species to diffuse and desorb more readily and from deeper within the film.

Impact of Steam Annealing on Device Properties

From the proceeding data and discussion, it is clear that steam annealing reduces residual NO_3^- and Cl^- content, mitigates water absorption, and improves the morphology of LZO films. To determine the impact of steam annealing on device properties, we incorporated LZO films into MIS capacitors and examined their dielectric properties. Our SEM studies show that LZO films deposited from NO_3^-/Cl^- precursors contain voids when dry-annealed but not when steam-annealed. Therefore, a comparison of device properties between dry- and steam-annealed LZO (NO_3^-/Cl^-) films would not be informative, as the dry-annealed films would display undesirably high leakage currents and poor device properties. For this reason, we characterize devices fabricated from LZO (NO_3^-) films.

Generally, and regardless of annealing atmosphere, dielectric constants increase and loss tangents decrease with increasing annealing temperature (Figure 5.7). We attribute this to increased condensation and densification as annealing temperature increases. Steam annealing at 350 and 500 °C produced films with higher dielectric constants relative to dry-annealed films. We note that the dielectric constant for the humid-annealed 350 °C film is approximately the same as for the 500 °C dry-annealed film. This is consistent with greater degrees of condensation and densification in the humid-annealed films, which is supported by FTIR, TPD, and XPS studies. Additionally,

breakdown and leakage current characteristics were similar for films annealed under dry and humid conditions (Figure AC9), suggesting that the enhanced dielectric constants observed for steam-annealed films are not due to water incorporated from processing under water vapor. Notably, 200 °C steam-annealed films produced stable, functional MIS devices, whereas devices prepared from films dry-annealed at the same temperature were nonfunctional.

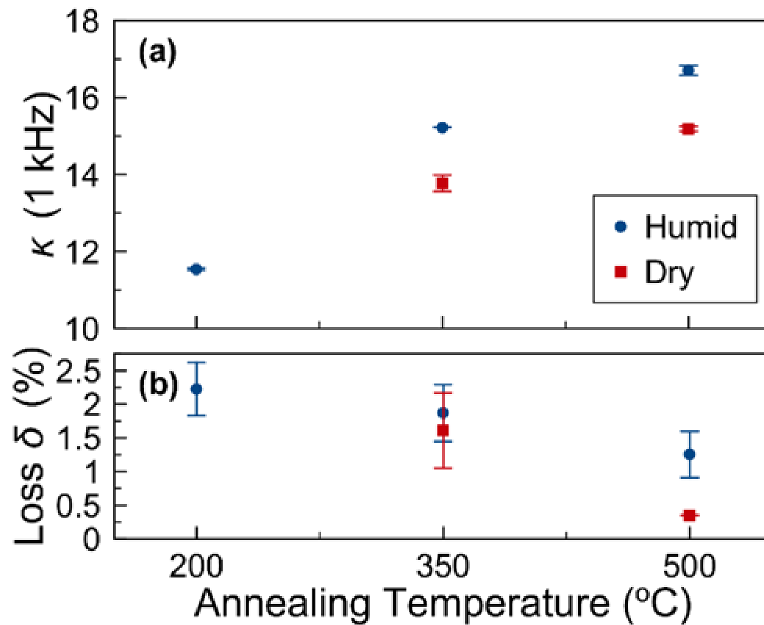

Figure 5.7. (a) Dielectric constants (κ) and loss tangents (loss δ) for MIS devices made from two-coat LZO (NO_3^-, 1.0 M) films (~100 nm) annealed at various temperatures under dry (red squares) or humid (blue circles) conditions.

Conclusion

We report the dramatic effects of steam annealing on metal oxide films deposited from aqueous precursors. Steam annealing significantly reduces residual NO_3^- and Cl^- content, enhances resistance to water absorption, prevents void formation, and enhances dielectric properties. We postulate steam annealing increases the inner sphere hydration

of metal cations (preventing strong counterion binding) and facilitates improved counterion removal via water/acid azeotropic evaporation. Steam annealing may also suppress condensation at low processing temperatures, thereby enhancing the diffusion and desorption of counterions and condensation byproducts from the films. Overall, this study shows that annealing humidity affects the decomposition temperatures and chemical evolution pathways of metal oxides from aqueous solution precursors. Our findings indicate steam annealing offers a promising avenue for producing high-quality device components with enhanced properties relative to ambient thermal processing methods.

Bridge

Chapter V discussed the impact of steam annealing on the evolution of aqueous precursors into thin films. Specifically, steam in the annealing atmosphere was shown to enhance counterion removal at low temperatures, promoting hydroxide condensation and subsequent densification of the oxide. Film stability with respect to water absorption was improved and dielectric properties of lanthanum zirconium oxide, introduced in Chapter III, were also augmented. The effects of steam annealing were demonstrated for a variety of oxide materials, making it a general method for lowering processing conditions for aqueous-based oxide thin films.

Thin films deposited from homogeneous aqueous solutions are generally assumed to be homogeneous. To date, there have been several reports of non-uniform density profiles in aqueous-based films, but it is unclear if these inhomogeneities stem from density or

composition gradients in the films. Chapter VI provides a detailed investigation of the nature and origin of these non-uniform density profiles.

CHAPTER VI

NON-UNIFORM COMPOSITION PROFILES IN INORGANIC THIN FILMS FROM AQUEOUS SOLUTIONS

Authorship Statement

This chapter was previously published as a full article in *ACS Applied Materials and Interfaces* in 2016 (volume 8, pages 667-672) and was coauthored by Kurtis C. Fairley, Devin R. Merrill, Keenan N. Woods, Jeffrey Ditto, Can Xu, Richard P. Oleksak, Torgny Gustafsson, Darren W. Johnson, Eric L. Garfunkel, Gregory S. Herman, David C. Johnson, and Catherine J. Page. The manuscript was written by K.C.F., D.R.M., and K.N.W. with contributions from J.D. Editorial assistance was provided by T.G., D.W.J., E.L.G., G.S.H., D.C.J., and C.J.P. Experiments were performed by K.C.F., D.R.M., K.N.W., J.D., C.X., and R.P.O. with data analysis done by K.C.F., D.R.M., and K.N.W.

Introduction

Inorganic coatings are ubiquitous in modern technology. While the majority of inorganic coatings are made via high-vacuum processes (e.g., sputtering, evaporation, atomic-layer deposition), there has long been an interest in preparing dense, smooth inorganic coatings using a solution route. Perhaps the most widely studied solution route to thin films is the sol-gel method, which generally employs non-aqueous solvents.[1] This method has been used to prepare films with varying degrees of porosity and a wide range of pore sizes. Sol-gel-derived monoliths and films can generally be described as porous rigid oxide networks in which the pores are filled with liquid or gas.[1,2] More recently,

Keszler and coworkers have developed a "prompt inorganic condensation" (PIC) aqueous route to prepare ultrasmooth amorphous inorganic films with a variety of cations by controlling the condensation process.[3–10] This method allows the preparation of dense oxide films with near-atomic surface smoothness, presumably due to the surface tension of the water-based solution during spin coating.[3,10] Film thicknesses can easily be controlled via the concentration of the solution and the physical parameters used to spin the films. Thin films made via PIC have been incorporated into thin-film transistors using spin coating and low-temperature annealing to obtain devices that meet or exceed the performance of conventional vapor-deposited devices.[5,11–15] PIC films prepared from solutions of hafnium oxychloride dissolved in sulfuric acid (HafSOx) with added peroxide have been shown to function as ultrahigh-resolution resists, patternable with electron beam or extreme ultraviolet radiation.[16,17] These resists enable patterning with minimum linewidths and edge roughness superior to those obtainable using organic resist materials using conventional lithography techniques. These advantages are expected to become even more important for extreme ultraviolet (EUV) lithography in next generation semiconductor manufacturing.[18]

For solution-processed films, developing a fundamental understanding of the chemistry occurring in each processing step is critical for improving film morphology and performance.[19–23] In the case of inorganic metal oxide films (using sol-gel or PIC), processing steps include: film deposition (via spin coating or dip coating), a "soft bake" to drive off excess solvent, and higher temperature annealing to facilitate counterion removal and condensation. In the sol-gel process, evaporation of organic solvent molecules and simultaneous hydrolysis reactions at relatively low temperatures lead to a

stiff inorganic network, and subsequent drying occurs via evaporation from pores.[24] By contrast, in the aqueous PIC route, evaporation of solvent (water) involves considerably more energy due to hydrogen bonding and increased solvent/solute interaction strength. The loss of water leads to condensation reactions that directly link the inorganic species as their concentration increases.[12]

Although fundamentally different chemistries occur in the various methods used to prepare inorganic films, drying and densification models generally assume the resulting films are homogeneous.[24] However, there are a few previous studies that show inhomogeneities in sol-gel-derived multilayer films observable by TEM[25] or X-ray reflectivity (XRR).[26,27] Denser surface "crusts" in single-layer films have also been observed via ellipsometry in sol-gel silica coatings[28] and by XRR in PIC aluminum oxide phosphate films.[29] The nature of these inhomogeneities, whether due to density variations or compositional inhomogeneity, has not been determined. This prompted us to undertake a systematic study of density and composition gradients in PIC-prepared films using multiple techniques.

In this work we present XRR data on a diverse set of films made using PIC with different metal precursor solutions. The three material systems investigated were selected based on their ability to form dense, smooth, amorphous thin films. Films comprised of multiple layers yielded XRR patterns inconsistent with those expected for homogeneous films, suggesting a general phenomenon of density or composition gradients in the individual layers of PIC-derived films. Using HafSOx as a model system, single and multilayer films annealed at different temperatures were examined using XRR, cross-sectional high-angle annular dark-field scanning transmission electron microscopy

(HAADF-STEM), and medium energy ion scattering (MEIS). These techniques reveal the evolution of density and compositional inhomogeneity in the films during processing. They suggest a thin, dense surface crust forms during spin coating, presumably because the reactants near the surface dehydrate faster than the interior of the film. This surface crust persists during subsequent low-temperature annealing, but surprisingly does not increase in thickness. Because the performance of photoresists has been shown to be very sensitive to processing conditions,[22] controlling the inhomogeneity in HafSOx films may be an important avenue towards improving performance in ultra-high resolution resist applications. More generally, the presence of a dense surface layer may affect the kinetics of film formation, as well as the final properties of metal oxide films derived using PIC. Therefore, understanding and controlling the formation of the surface layer is important for tailoring the evolution and properties of films made using this method.

Experimental

InGaO$_x$ *and AlO*$_x$ *Precursor Solution Preparation*

A 2.00 M total metal concentration (6:7 In:Ga) solution of $In(NO_3)_3 \cdot xH_2O$ (Sigma Aldrich, 99.9% In) and $Ga(NO_3)_3 \cdot xH_2O$ (Alfa Aesar, 99.999% Ga) and a 1.70 M metal concentration solution of $Al(NO_3)_3 \cdot 9H_2O$ (Alfa Aesar, 98% Al) were electrochemically treated to reduce nitrate counterion concentrations according to previously reported methods.[30,31] Water contents of the indium and gallium nitrate hydrate salts were determined through calcination of the salts to form the oxide and back calculation of the hydrate content (~5 and ~8 H_2O for the indium and gallium nitrate hydrate salts, respectively). Both solutions were diluted to 0.25 M (total metal concentration) with 18

MΩ cm nanopure water and filtered through 0.45 μm PTFE filters.

$Hf(OH)_{4-2x-2y}(O_2)_x(SO_4)_y \cdot zH_2O$ (HafSOx) Precursor Solution Preparation

A 1.00 M stock solution of $HfOCl_2 \cdot 8H_2O$ (Alfa Aesar, 98% Hf) was prepared by dissolution and dilution with 18 MΩ cm nanopure water. Solutions for spin coating were prepared by mixing 2.000 N H_2SO_4(aq) (VWR) and 30 wt % H_2O_2(aq) (EMD Millipore) followed by the addition of $HfOCl_2$(aq).[32] The final solution was diluted using 18 MΩ cm water to a concentration of 0.105 M sulfuric acid, 0.45 M hydrogen peroxide, and 0.15 M Hf. The four-coat multilayer was synthesized from a solution without peroxide to decrease the solubility of the film, allowing for a lower annealing temperature to prevent subsequent layers from dissolving the previous.[17]

$InGaO_x$, AlO_x, and HafSOx Film Preparation

N-type, Sb-doped silicon substrates (0.008-0.02 Ω cm) received surface treatments using a MΔRCH cs-1701 plasma cleaner running on O_2 plasma at 30% O_2 in N_2 using 150 W for 60 s immediately before spin coating. Films were prepared by filtering the solutions through a 0.45 μm filter and spin coating at 3000 rpm for 30 s. The HafSOx thin films were subjected to a 1 min anneal at either 80 °C for a single layer or 180 °C for the multilayer samples. The $InGaO_x$ and AlO_x multilayer films were annealed at 450 °C for 20 min per coat followed by a final 60 min anneal at 450 °C. All films were annealed on a preheated, calibrated hot plate.

Thin Film Characterization

XRR patterns were obtained on a Bruker D8 discover (Cu Kα radiation). Sample alignment was checked to ensure that the incident and exit angle were equal and that the sample was in the center of the goniometer. Alignment procedures involved iteratively performing rocking curves and z (height) scans to ensure the aforementioned criteria were met.[33]

Fits of the XRR data were performed using the Bede REFS software package, which creates a population of solutions based on an initial model and uses a genetic algorithm to minimize residuals.[34] Once the best fit was achieved, the models were perturbed to confirm that the model was not a local minimum. Films were initially fit as a single film, to determine the average density and total film thickness. For single coat films, the model was then split in half, with each half being allowed to vary thickness and density independently to improve the fit. A gradient was also added to the fit, as the abruptness of the interface was unknown. Comparison of the difference between the simulated and experimental data (i.e., residuals) over a constant range allows for the quantitative comparison of the fits for a single data set. Comparison of residuals between different data sets requires a more detailed analysis, as the noise inherent in the experimental data contributes differently to the residuals for each data set. Multilayer films were modeled similarly; each coat was split into a two-layer unit, and each layer was allowed to vary independently in thickness and density (all coats assumed to be identical).

For scanning transmission electron microscopy (STEM) investigations, a thin cross-section sample was prepared from a section of the film using an in situ lift-out process on a FEI Helios 600 equipped with a Sidewinder ion column and a Quorum cryo stage.[35]

Steps were taken to avoid exposure of the beam-sensitive film while imaging with the SEM and sputtering with the focused ion beam (FIB). Prior to loading the sample in the FIB-SEM, the sample was coated with a 30 nm protecting layer of evaporated carbon. A second 1.5 μm thick protecting layer of FIB-induced carbon was deposited over the area of interest using a 2 keV accelerating voltage (<5 nm stopping range in evaporated carbon). The lift-out and thinning process was carried out using a 500 eV accelerating voltage on the electron beam to minimize the interaction volume of the beam (<9 nm interaction depth). After completing the lift-out, the sample remained 1.5 μm thick to assure no beam interaction had taken place. The sample was then cooled to -170 °C throughout the thinning process. The FIB accelerating voltages used were lowered as the thickness decreased, 30 keV (1.5 to 0.5 μm), 5 keV (500 to 100 nm), and 2 keV (100 to 40 nm). During thinning the sample was monitored using low dose electron beam conditions to reduce risk of exposure and excessive heat (periodic single frames using 500 eV, 90 pA, 500 ns dwell per pixel, 50 um horizontal field width, 1024 x 768 pixels). The thin sample (approximately 40 nm thick) was warmed slowly overnight in the FIB-SEM vacuum chamber to ambient temperature. HAADF-STEM imaging was completed on a FEI Titan at 300 keV (0.245 m camera length, 10 μs dwell, 2048 x 2048 pixels, and 0.6 nA current) at -175°C with a Gatan single-tilt cryo-transfer holder.

MEIS, a high resolution version of Rutherford backscattering (RBS), was performed at the Rutgers MEIS facility using 130 keV protons as the incident ion.[36]

Results and Discussion

Four-coat samples of $InGaO_x$, AlO_x, and HafSOx were prepared using PIC as

described earlier and examined by XRR (Figure 6.1). For all samples, the XRR patterns consist of regular Kiessig fringes with a pattern of varying intensity. Figure 6.2a contains a schematic of two potential structures of these films, one that is homogeneous and one that contains a repeating structure of four layers (coats) where each layer has an identical non-uniform electron density gradient. Figure 6.2b contains the simulated XRR patterns for these two films. Since XRR is very sensitive to variations in electron density, small (1%) differences in electron density can be detected. The simulated XRR pattern for a homogeneous single-coat film shows a characteristic systematic decay in the Kiessig fringe intensity with increasing diffraction angle. The simulated XRR pattern of the film with a repeating structure of four identical layers with non-uniform electron density contains a characteristic modulation of the Kiessig fringe decay, with more intense diffraction maxima corresponding to the thickness of the individual layers resulting from

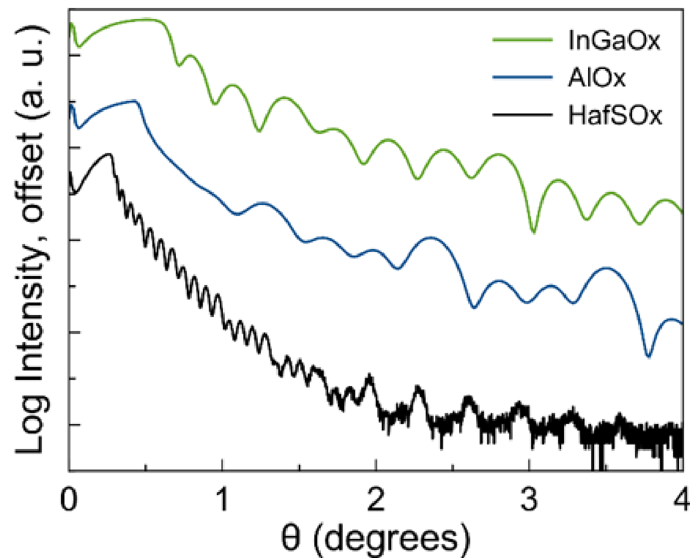

Figure 6.1. XRR patterns of four-coat films of $InGaO_x$, AlO_x, and HafSOx without peroxide (top to bottom, respectively). The patterns are offset for clarity.

the coherent scattering of the electron density profiles in each layer. Between these more intense maxima are n - 2 smaller maxima, where n is the number of coats, resulting from incomplete destructive interference. All of the multilayer films prepared via PIC have XRR patterns (Figure 6.1) characteristic of films consisting of repeating layers of non-uniform electron density profiles, inconsistent with those expected for homogeneous films. This suggests that this inhomogeneity is a general characteristic of PIC solution-deposited thin films. We elected to study the effects of this phenomenon in more detail for the HafSOx system.

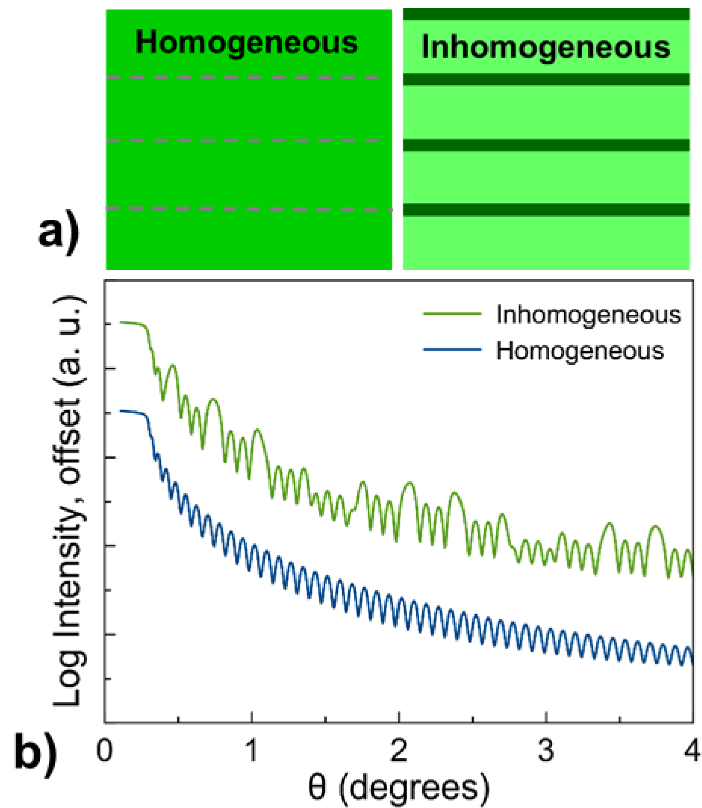

Figure 6.2. (a) A schematic representation of two simple structures of a four-coat stack, one in which each coat is homogeneous and one where each coat has the identical inhomogeneous electron density. (b) Simulated XRR data for the two cases shown in panel (a).

In Figure 6.3, we model the XRR data of the four-coat HafSOx film assuming that each deposited coat consists of a bilayer: a “bulk” layer and a surface layer. The density and thickness of the bulk and surface layers were allowed to freely vary in order to obtain the best possible fit. It was also assumed that all four coats were identical as a simple, first approximation. This model is not quantitative, as the actual structure is more complex due to the different thermal treatment for each layer. Within these constraints, the best fits were obtained with a thin surface layer (or crust) in each coat with a higher electron density than the underlying bulk layer. Attempts to perturb the models to give a bulk layer of higher density than the surface layer resulted in low-quality fits. Although this model is an oversimplification, it indicates that the films have a higher density surface region within each deposited layer.

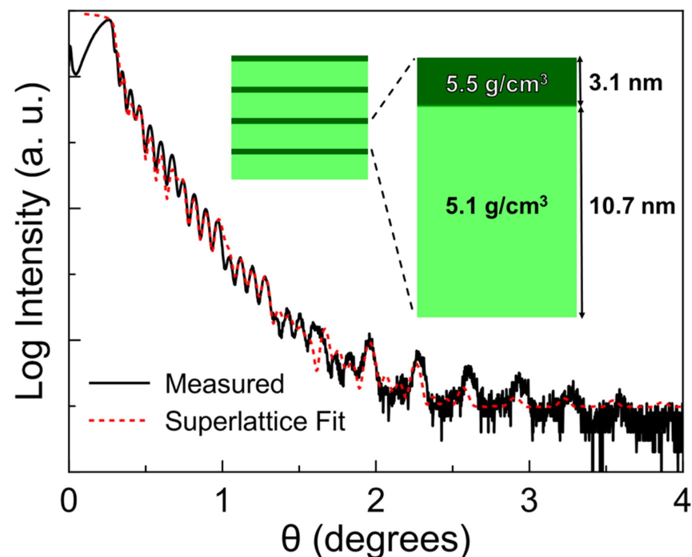

Figure 6.3. Raw and modeled XRR data of a four-coat multilayer of HafSOx without peroxide annealed at 180 °C for 1 min.

A single coat film was also investigated to determine if the crust is inherent in each coat or whether it is induced by the processing conditions used to make the four-coat multilayer. To match the processing of the four-coat multilayer, the film was annealed at 180 °C. XRR data for the single-coat film was modeled both as a homogeneous single-layer film and as a bilayer separated by a gradient. For the latter model, the surface and bulk layer were allowed to freely vary in thickness and electron density (Figure 6.4).

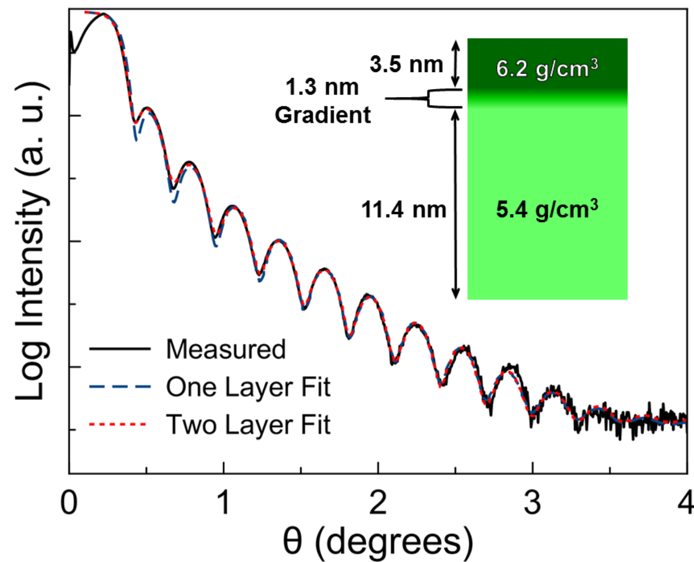

Figure 6.4. XRR data for a single-coat HafSOx film without peroxide annealed at 180 °C for 1 min. The data were modeled as a homogeneous single layer and as a bilayer with a thin, dense surface layer and a less dense bulk layer separated by a density gradient. The addition of the surface "crust" improved the agreement between the model and the data, especially in the first three observed minima in the XRR pattern.

Between the two models, the two-layer model with a thin, denser crust has a 20% reduction in the residuals as compared to the single-layer model when both models are allowed to search for the minimum using the genetic algorithm and modeling procedure described previously. Perturbing the models from the fits to find better solutions was unsuccessful, indicating the refined fits represent global minima. In XRR, the density

values are derived from the critical angle, which is directly related to electron density. In order to obtain density in g cm^{-3}, the composition of the film must be assumed. Therefore, the density values of the layers should be viewed as being approximate, as they depend on the model used. The modeling suggests the best description of the film within the applied modeling constraints is that of a less electron-dense layer topped by a thin, higher electron density crust. These are probably separated by a thin gradient region between the surface and bulk layers, which was included in the model of the single-coat films. This two-layer model with a thin, dense crust therefore qualitatively agrees well with the modeling of the individual coats in the four-coat film, which was previously discussed. Not surprisingly, the simple model assuming four identical bilayers does not quantitatively match the model used for the single-coat films, where the addition of a gradient layer increases the density of the surface layer. In both models, a denser surface crust and less dense bulk layer are required to obtain good fits.

Since it has previously been reported that peroxide-containing HafSOx films used for lithography were homogeneous,[17] new films containing peroxide were prepared to test whether the crusts observed above also occur when peroxide is added. These peroxide-containing films were also used to examine the effect of annealing temperature. In order to replicate HafSOx films used for patterning, a single coat film containing peroxide was annealed to the soft-bake temperature of 80 °C for XRR studies. As seen in Figure 6.5, not only does the bilayer model give a better fit to the data but also the residuals are reduced by 50% when the model is allowed to create two layers separated by a gradient. This supports the formation of a crust in films containing peroxide, even at the low soft-bake temperatures used for lithography.

XRR studies reveal electron density gradients and periodicity (in multilayers), but do not reveal the source of the density gradients (i.e., whether they are due to density variations of a single chemical composition or a chemical gradient). Additional information on the HafSOx films was obtained using HAADF-STEM. Cross-sections of a

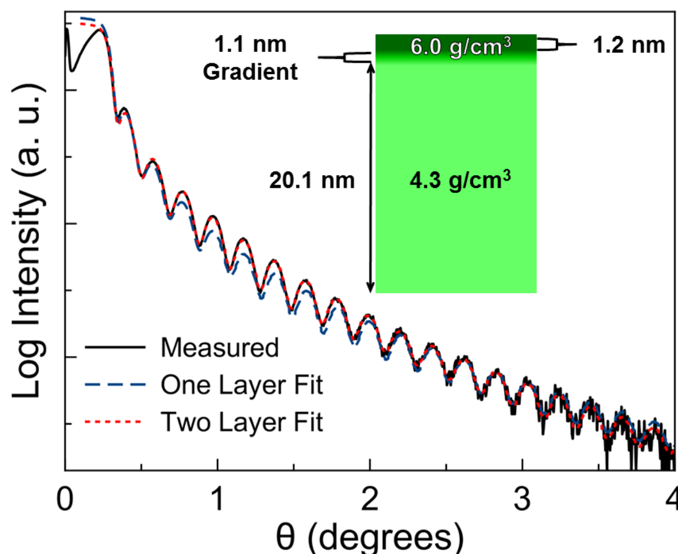

Figure 6.5. XRR data for a single-coat HafSOx film containing peroxide annealed at 80 °C for 1 min. The data were modeled as a homogeneous single layer and as a bilayer consisting of a thin, dense surface layer and a less dense bulk layer separated by a density gradient. The addition of a surface "crust" improved the agreement between the model and data, especially with respect to the minima in the XRR pattern between 0.8 and 2°.

single-coat film containing peroxide were prepared with care to maintain its condition prior to exposure, and a representative cryo-HAADF-STEM image is shown in Figure 6.6a. The image reveals a bright thin band at the top of the sample, indicating an increased density of heavy atoms at the surface. Integration of the average HAADF signal intensity over the highlighted area in Figure 6.6a provides a two-dimensional plot of the heavy atom density profile across the film (Figure 6.6b). This indicates that, in addition to concentration of heavy atoms at the surface of the film, there is also a slight increase of

heavy atom density near the bottom of the film. This data provides direct evidence that there is electron density inhomogeneity within the films and supports the two-layer XRR model used earlier.

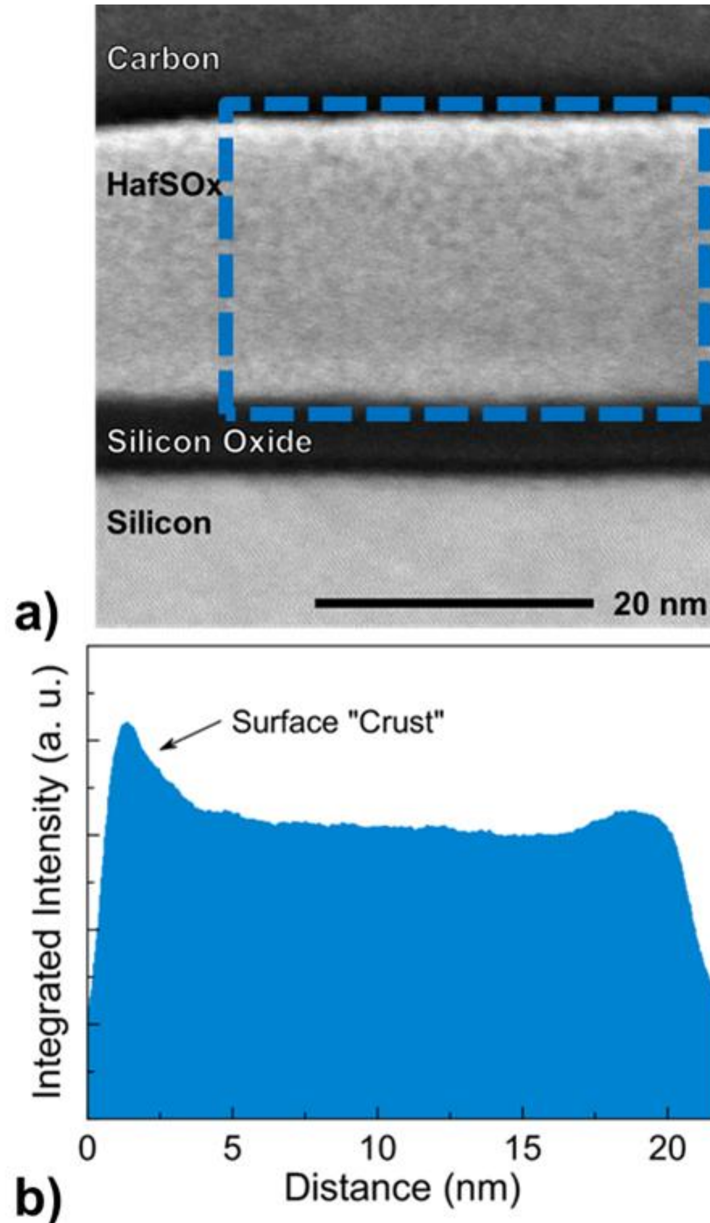

Figure 6.6. (a) HAADF-STEM image of the cryo-FIB cross-section of a single-layer HafSOx film containing peroxide annealed at 80 °C for 1 min and (b) the heavy atom density profile of the film obtained by integrating the intensity of the pixels in the boxed region in panel (a).

In order to obtain information about chemical inhomogeneity, MEIS data were collected as a function of annealing temperature and time. MEIS, a low energy, high-resolution version of RBS, is a quantitative technique. The experiment directly measures the number of backscattered ions of each mass. Using calibrated instrumental parameters and well-established cross-sections, these can be converted into areal densities. Further, the ions lose energy as they travel through the film, with the amount of energy loss being a measure of the distance traveled. The width of a peak in an MEIS spectrum is therefore a measure of the thickness of the corresponding layer, and its integrated area yields a direct quantitative areal density (atoms cm^{-2}). The highest energy peak results from protons backscattered from the heaviest atom (i.e., Hf) in the film. The areal density can be converted into a thickness if the bulk density is known (e.g., from XRD), and, conversely, the density can be determined if one has an alternative measure of thickness (e.g., from TEM). Because there is some uncertainty in the water content of the HafSOx films (which depends on processing conditions, film history, temperature, and gas-phase partial pressures during characterization), precise comparisons between different samples is challenging. Nevertheless, the relative density changes from MEIS in the film as a function of depth are quite meaningful.

Hafnium segregation to, or densification at, the surface is readily apparent from the raw MEIS data (Figure 6.7). If Hf were distributed uniformly throughout the film, the highest energy peak (corresponding to Hf) would have a “flat” plateau. However, the intensity of the Hf MEIS peaks is greatest at the highest detected energy (at the surface) and is decreased at lower energies (further below the surface). This is consistent with the increased intensity in the HAADF-STEM image at the surface due to an increased

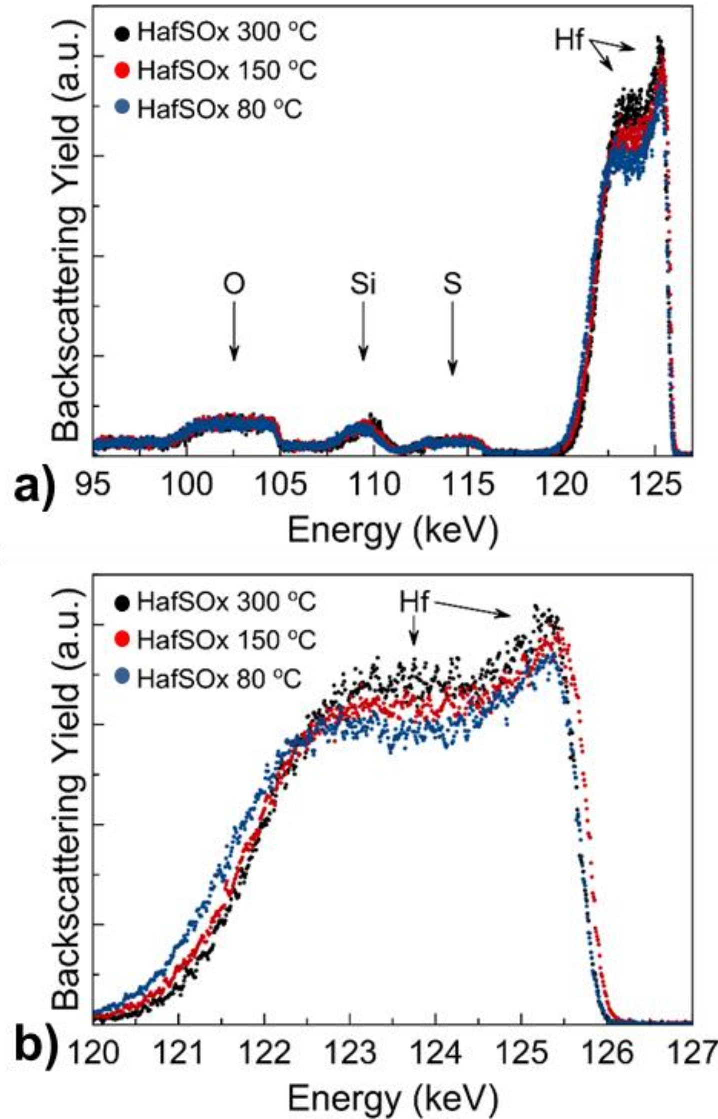

Figure 6.7. (a) MEIS data collected on a HafSOx film containing peroxide annealed for 3 min at 80 °C (blue), 5 min at 150 °C (red), and 5 min at 300 °C (black). (b) An expansion of the Hf area, which visually demonstrates the total film thickness decreases with increasing annealing temperature while the average density increases. The peak at 125 keV indicates that all of the films have a surface layer with higher Hf density.

concentration of heavy atoms (i.e., Hf). It is also readily apparent in the MEIS spectra that the film thickness decreases (with corresponding increase in density) as the annealing temperature is increased (Figure 6.7b). Qualitatively, the MEIS data is consistent with the results obtained from XRR and STEM investigations. All three techniques indicate the

presence of a Hf-enriched denser surface crust in all HafSOx films reported in this work (annealed from 80 to 300 °C, with or without peroxide).

Conclusion

The data presented suggests that films prepared from aqueous solutions via the PIC process are inhomogeneous in composition and density throughout their thickness. For HafSOx films, a dense region forms at the surface after a low-temperature anneal. This may result from enhanced evaporation of solvent at the surface of the film, increasing concentration and resulting in condensation reactions between the Hf-containing moieties to yield a dense surface layer on the film. Presumably this acts as a diffusion barrier, leading to the lower density observed in the bulk of the film. We postulate that the slow rate of water diffusion through the crust relative to the rate of diffusion within the bulk layer of the film prevents the formation of density gradients in the bulk of the film during subsequent annealing. In the case of HafSOx, the denser surface layer may influence the patterning resolution and contrast obtainable with this system. It may be possible to control the density and/or thickness of the surface crust by adjusting annealing conditions (e.g., temperature, atmosphere, ramp rate) and to correlate changes with patterning metrics. We also show that crust formation is quite general for PIC processed films and that the density inhomogeneities in single coats result in periodic density gradients in multilayer films, which may affect film properties such as electrical conductivity or breakdown voltage. In the case of multi-metal-component oxides deposited from solutions of mixed metal cations, the chemical composition profiles are expected to be more complicated and dependent on a number of factors (e.g., metal solubility and

diffusion rate differences). Determining chemical composition gradients at the nanoscale would enable the development of a mechanistic picture of the chemistry occurring during film formation and provide avenues to design chemical inhomogeneities to obtain enhanced properties. The determination of chemical composition gradients at the nanoscale, however, remains a major analytical challenge. Ultimately, understanding and controlling film inhomogeneities will provide an additional tool to modify the physical and chemical properties of films prepared using the PIC approach.

Bridge

In this Chapter, non-uniform density profiles were linked to composition inhomogeneities in hafnium sulfate oxide thin films. Specifically, greater electron density at the film surface was attributed to Hf-enrichment resulting from increased evaporation at the film surface.

Chapter VI focused on non-uniformities in a single-metal component oxide, but complex compositional gradients likely exist in multi-metal oxides, which are often used to achieve particular properties for specific applications. Chapter VII details density and composition gradients in lanthanum zirconium oxide films. The next Chapter also investigates the implications of stacking inhomogeneous single layer films to prepare multilayer films, a method commonly used to control film thickness.

CHAPTER VII

NON-UNIFORM COMPOSITION PROFILES IN AMORPHOUS MULTI-METAL OXIDE THIN FILMS DEPOSITED FROM AQUEOUS SOLUTION

Authorship Statement

This chapter was previously published as a full article in *ACS Applied Materials and Interfaces* in 2017 (volume 9, pages 37476-37483) and was coauthored by Keenan N. Woods, Milana C. Thomas, Gavin Mitchson, Jeffrey Ditto, Can Xu, Donna Kayal, Kathleen C. Frisella, Torgny Gustafsson, Eric Garfunkel, Yves J. Chabal, David C. Johnson, and Catherine J. Page. The manuscript was written by K.N.W. with contributions from M.C.T., G.M., J.D., and C.X. Editorial assistance was provided by T.G., E.G., Y.J.C., D.C.J., and C.J.P. Experiments were performed by K.N.W., M.C.T., G.M., J.D., C.X., D.K., and K.C.F.

Introduction

The diversity of chemical and physical properties exhibited by metal oxide thin films make them critical components in a number of technological applications, including electronic display,[1–4] photovoltaic,[5–8] and fuel cell technologies.[9–11] For many applications, oxide films with multiple metal components are necessary to achieve desired properties. Solution deposition is an attractive method for producing multi-metal oxides because it enables facile manipulation of metal compositions by controlling precursor stoichiometry,[12] and offers the promise of high-throughput processing and large area coverage.[13–15] Sol-gel routes are the most common solution deposition methods, but

all-inorganic aqueous routes produce high-quality, dense films without the need for organic additives.[16–26] In some cases, aqueous solution deposition yields films with device properties comparable to films made using atomic layer deposition.[27,28]

Despite the inherent differences between organic sol-gel and aqueous deposition routes, density inhomogeneities have been observed in films derived from both solution deposition methods.[29–36] Recently, we reported the first in-depth chemical analysis of non-uniform density profiles in aqueous-derived thin films.[34] Specifically, Hf enrichment at the surface of hafnium sulfate oxide (HafSOx) films was observed, and the denser, more condensed surface layer was attributed to enhanced evaporation at the film surface. The HafSOx system has a single metal component, but a multi-metal oxide might be expected to have a more complex distribution of metal components. For example, differences in the network forming ability and diffusion rates of metal species may give rise to inhomogeneous metal distributions.

We recently reported density inhomogeneities in lanthanum zirconium oxide (LZO) thin films,[35,36] which are of interest as high-κ gate dielectrics[35,37–43] and as barrier layers for a number of applications.[44–50] We demonstrated that single layer LZO films have non-uniform electron densities, consistent with a bulk layer capped by a thin (1-3 nm) surface layer of different density.[35] Additionally, preliminary data indicate that these inhomogeneities persist when multiple coats of solution are stacked to make multilayer films,[36] a common practice for producing films with a desired thicknesses. From these initial studies, it is not clear if the observed non-uniform density profiles are the result of inhomogeneous metal distributions or simply a consequence of density gradients in the oxide network (with uniform metal ratios throughout).

In this study, we detail an in-depth chemical analysis of non-uniform density profiles in amorphous aqueous-deposited LZO films. We show that density variations in single and multilayer LZO films are associated with inhomogeneous La and Zr distributions. Specifically, we find that La is concentrated at the film surface and at the interface between sequentially deposited layers in multilayer LZO films. We attribute the inhomogeneous metal distributions to differences in solubility and network forming ability of the two metal components. We also show that layering artifacts in multilayer films do not negatively impact electrical properties; multilayer films have higher dielectric constants, in agreement with greater condensation (and densification) relative to single layer films. Similar inhomogeneities are likely present in other solution-deposited oxide films with multiple metal components, and determining the chemical origin of these inhomogeneities is a critical first step for understanding their effect on film properties.

Experimental

Precursor Solution Preparation

LZO precursor solutions were prepared by dissolving $La(NO_3)_3 \cdot 6H_2O$ (Alfa Aesar, 99.9%) and $ZrO(NO_3)_2 \cdot xH_2O$ (Sigma-Aldrich, 99%) in 18.2 MΩ cm Millipore H_2O. Solutions with various total La and Zr metal concentrations (1:1 ratio) were prepared via stirring and gentle heating, followed by filtration through a 0.45 μm PTFE syringe filter. Precursor solutions are stable for at least six months, with no observed precipitation.

Thin Film Preparation

Si substrates were prepared with a 5 min sonication in 5% Decon Labs Contrad-70 solution, followed by rinsing with 18.2 MΩ cm H_2O, spin-drying, and a 1 min oxygen plasma etch using a PE-50 Benchtop Plasma Cleaner (Plasma Etch, Inc.) set to maximum power. Five drops of LZO precursor solution were deposited through a 0.2 µm PTFE syringe filter onto the substrates, then spun at 3000 rpm for 30 s. Samples were immediately placed onto a hotplate preheated to 125 °C. Single layer films were ramped to 450 °C (25 °C min^{-1}) and annealed for 1 h. Multilayer films were made by the sequential deposition of individual layers that were ramped from 125 °C to 450 °C (25 °C min^{-1}) and annealed for 10 min per layer, with a final anneal at 450 °C for 1 h. An annealing temperature of 450 °C was chosen because Fourier transform infrared spectroscopy (FTIR) indicates that nitrate is fully removed from the films by that temperature (Figure AD1). Precursor solution concentrations of 0.25, 0.33, 0.50, and 1.00 M were used to prepare four, three, two, and one layer samples, respectively, to give the same approximate overall thickness (~40 nm). All samples were annealed in air, unless otherwise noted.

Thin Film Characterization

Electron density profiles were studied via X-ray reflectivity (XRR) collected using a Bruker D8 Discover diffractometer with Cu Kα radiation. The incident beam was conditioned with large horizontal and vertical slits, and the exit beam was conditioned with a 0.1 mm detector slit. The data were collected from 0-10° 2θ in 0.015° steps at 25 s $step^{-1}$. Film density, thickness, and roughness were extracted from the XRR data using

Bede REFS modeling software.[51] A detailed description of the XRR modeling process can be found in the Appendix D.

Heavy atom distributions were examined using high-angle annular dark-field scanning transmission electron microscopy (HAADF-STEM). Cross-sectional lamellae were lifted out and thinned using an FEI Helios 600 FIB for HAADF-STEM imaging with an FEI Titan 80-300 TEM (300 keV, 240 mm camera length, 17.8 mrad convergence angle, 0.5 nA current), and image intensity profiles were extracted using Gatan DigitalMicrograph software.

For the STEM energy-dispersive X-ray spectroscopy (STEM-EDS) study, a separate lamella from the HAADF-STEM analysis was prepared from a three layer sample according to the same procedure, but using a C (instead of Pt/C) protective cap to avoid elemental interferences from Pt. The cross-sectional STEM-EDS data were collected as spectral images using a JEOL ARM 200 CF STEM (200 keV, 80 mm camera length, 1.0 nA current) equipped with a Thermo Fisher 80 mm^2 SDD (0.98 sr solid angle). The data were processed to obtain integrated intensity profiles using Python scripts written in IPython[52] and incorporating functions from the HyperSpy multi-dimensional data analysis toolbox.[53] STEM-EDS element intensities were quantified using the Cliff-Lorimer method and known film compositions[54] as measured using a quantitative thin film technique for electron probe microanalysis (EPMA).[55]

X-ray photoelectron spectroscopy (XPS) studies were conducted on films annealed to 450 ˚C under either vacuum (~430 mTorr) or ambient air in a stainless steel reaction chamber. The samples were characterized using a PHI 5600 spectrometer equipped with an Al Kα monochromatic X-ray source and a hemispherical analyzer under ultrahigh

vacuum conditions (~10^{-9} Torr). The composition was determined by using XPS peak area analysis in the MultiPak Software.

Medium energy ion scattering (MEIS), a high resolution version of conventional Rutherford Backscattering Spectroscopy (RBS), was conducted using a He^+ beam (190 keV). Backscattered ions were detected in a double alignment configuration, which significantly reduces background contributions to achieve monolayer depth resolutions. Quantitative depth profiles were obtained by analyzing the energy spectrum of backscattered ions. The measured spectrum was simulated with multiple 10 Å layers, and the ratio of La, Zr, and O was allowed to vary for each 10 Å layer until a best fit was obtained for the measured data.[56]

In situ FTIR absorption measurements were performed using a custom-built annealing chamber with a Thermo Nicolet 6700 IR spectrometer equipped with a liquid nitrogen cooled broadband mercury cadmium telluride (MCT-B) detector. All spectra were collected at 74° (Brewster's angle) with the sample positioned at 45 °C under N_2. Films were deposited on double-side polished Si and heated by direct resistive heating. Annealing was performed at successive temperatures for 5 min each under N_2.

Device Fabrication and Testing

Metal-insulator-semiconductor (MIS) devices were fabricated by depositing and annealing single and multilayer LZO films on degenerately doped p-type Si (0.008 to 0.020 Ω cm) and thermally evaporating Al top contacts (0.013 cm^2 dots, ~100 nm thick) onto the LZO films through a shadow mask. Electrical contact to the Si was made by physically scratching the film with a scribe and applying an In/Ga eutectic to the exposed

Si. Dielectric constants and loss tangents were calculated from impedance measurements made using an Agilent 4284A Precision LCR meter (20-10,000 Hz, 500 mV oscillation amplitude). Batch-to-batch variation was examined by fabricating two separate samples for each single or multilayer film architecture and measuring the impedance of five MIS devices per sample. Impedance measurements were done in a dark environment under ambient atmosphere.

Results and Discussion

Previously, we have demonstrated density inhomogeneities in single-layer LZO films.[35] In a separate HAADF-STEM image analysis development study, preliminary data suggested that the density inhomogeneities observed in single-layer films are preserved in stacked multilayer films.[36] To confirm this, XRR was used to probe the electron density profiles of multilayer LZO films of the same approximate thickness (Figure 7.1). Concentration was scaled inversely with the number of coats to give films of approximately the same overall thickness.[57] Kiessig fringe patterns for the multilayer films have modulated periodicity, indicating regular variations in electron density perpendicular to the substrate. The observed modulated periodicity in the fringe intensity is related to the number of deposited layers, with $n - 1$ low-intensity fringes between higher intensity fringes (where n is the number of coats). This is similar to the variations in Kiessig fringe intensity observed in XRR patterns reported for nanolaminate films made from stacked layers of materials with different densities.[16,58]

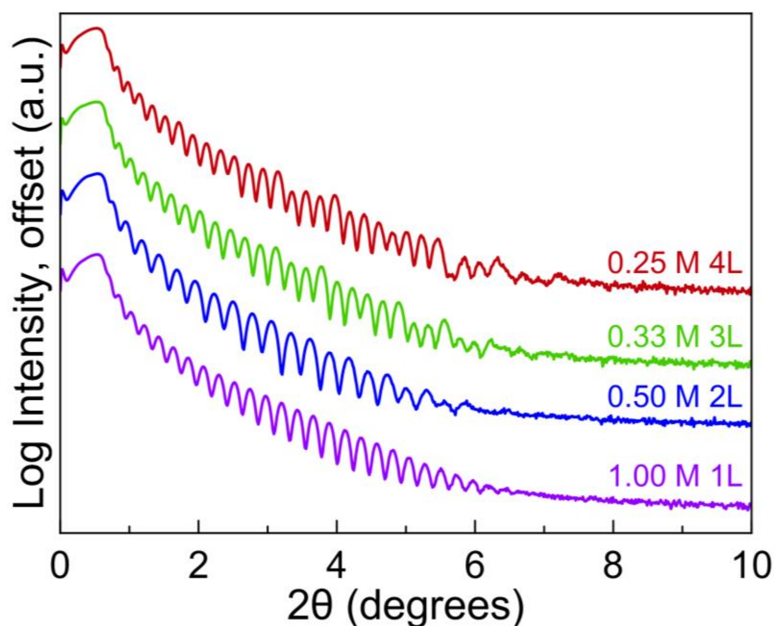

Figure 7.1. XRR patterns of four, three, two, and one layer LZO films deposited from 0.25, 0.33, 0.50, and 1.00 M precursor solutions from top to bottom, respectively.

Because XRR indicates the presence of periodic inhomogeneous electron density in the LZO multilayer films, a homogeneous single layer model will not be appropriate for fitting this data. Indeed, fitting the XRR data with a homogeneous single layer model results in poor fits (Figure AD2, Table AD1). A more complex model is thus required. Incorporating additional fitting parameters often results in improved fits; therefore, additional data from a complementary technique is necessary to determine a physically meaningful model.

HAADF-STEM was used to visualize the films and to examine heavy atom distribution in the same single and multilayer LZO films (Figure 7.2). The images show some variation in individual layer and overall film thickness. Because film thickness is linearly related to concentration,[57] we attribute variations in film thickness to differences in the spin-coater humidity during film deposition, which was not controlled in this

study.[59] Porosity is observed in the lower portion of the single layer LZO film, which we attribute to trapped water and nitrate species. We postulate that porosity is not observed in the multilayer films because nitrate and water can more readily diffuse to the film surface during annealing in the thinner individual layers that comprise the multilayer stack. Notably, the HAADF-STEM images of the multilayer films show distinct bright 'interfaces' between deposited coats, which are absent in the single layer LZO film. Because HAADF-STEM is sensitive to high-Z atoms in the sample, the brighter regions correspond to higher concentrations of heavy atoms (presumably La in this case).

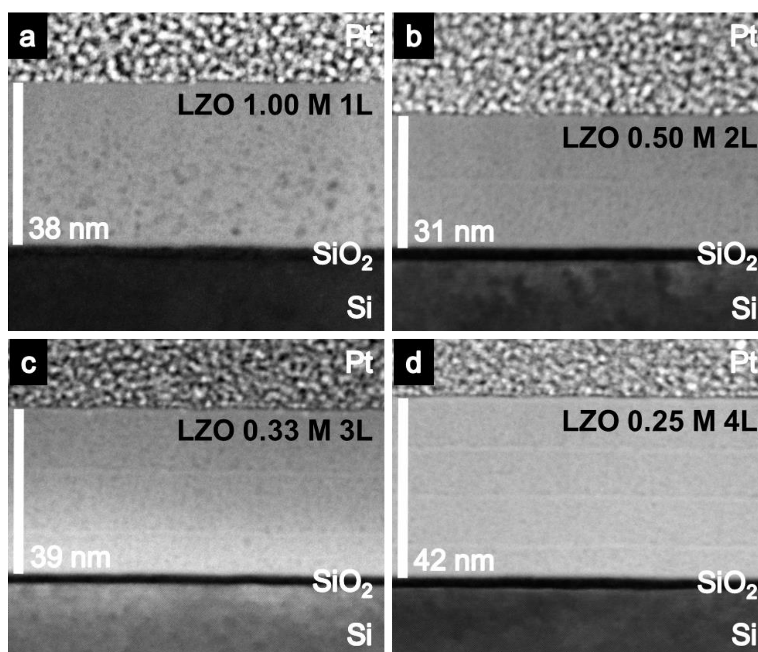

Figure 7.2. HAADF-STEM images of one (a), two (b), three (c), and four (d) layer LZO films deposited from 1.00, 0.50, 0.33, and 0.25 M precursor solutions, respectively. Bright interfaces can be seen in the multilayer films.

Using the HAADF-STEM images as a guide, more complex models with interfacial layers between 'bulk' layers and a thin capping layer (Figure AD3, Table AD2) were fit to the XRR data in Figure 7.1. Although the fit of the informed models were greatly

improved in comparison to the homogeneous single layer models, these more complex models are still likely an oversimplification of the electron density profiles of the films. For example, the abrupt interfaces between the individual layers in the models do not account for density gradients within the films. The "best fit" models are simply one solution (informed by complementary HAADF-STEM data) that provides insight into the amorphous film structure. As noted previously, additional fitting parameters generally improve data fitting, but additional compositional information would be required to justify models with additional fitting parameters.

The chemical nature of the observed electron density inhomogeneities were investigated using HAADF-STEM, MEIS, and XPS experiments. Cross-sectional STEM-EDS provides a means for mapping atomic distributions in the films. Signal-to-noise tends to be an issue because sample volumes are small, and extended collection times can change/damage the sample. In our study we averaged signal from an area of the film to improve signal-to-noise, using a statistical analysis previously developed for averaging HAADF-STEM intensities.[36] The effects of lamellae sample thickness on STEM-EDS intensities were removed by generating the La:Zr atomic ratio profile (Figure 7.3) from the La Lα and Zr Lα intensity profiles (Figure AD4), assuming that the overall La and Zr intensities integrated from the whole film were proportional to the average film compositions measured using EPMA (Table AD3). The STEM-EDS La:Zr atomic ratio profile shows an abrupt increase in the La:Zr ratio at the surface of each deposited layer, which confirms the abrupt interfaces observed by HAADF-STEM. Furthermore, the La:Zr atomic ratio decreases as a function of distance from the surface of each individual layer. Each layer displays approximately the same change in La:Zr ratio. This is

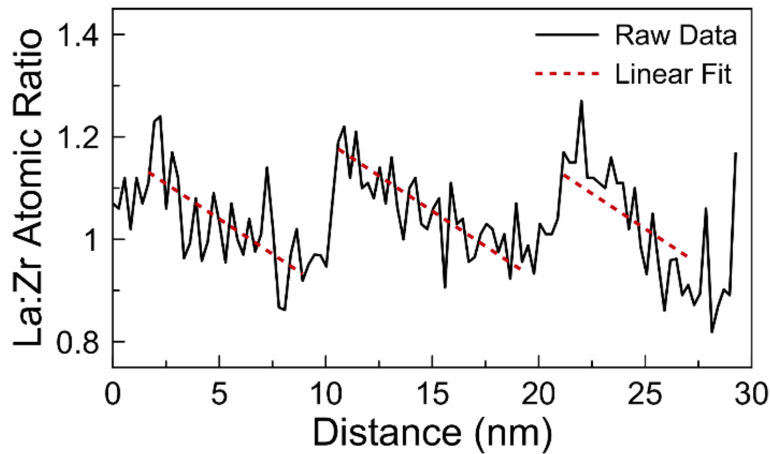

Figure 7.3. La:Zr atomic ratio as a function of distance from the film surface for a three layer film deposited from a 0.33 M precursor solution as determined by STEM-EDS elemental mapping (a distance of zero corresponds to the surface of the film). The dashed red line is a linear fit to the decrease in the La:Zr ratio as a function of distance for the topmost layer (x = 0 to 9 nm). The raw La Lα and Zr Lα intensity profiles can be found in Figure AD4.

highlighted by the red dashed lines in Figure 7.3, which represent a linear fit to the gradient in the topmost layer. The gradient in the La:Zr ratio suggests La enrichment at the surface of each deposited coat in the multilayer film. This enrichment is corroborated by MEIS and XPS data, which show enhanced La concentrations at the film surface (Figure AD5, Table AD4). Collectively, these data suggest that the observed bright interfaces in the HAADF-STEM images are the La-rich surfaces of the sequentially deposited LZO coats that comprise the multilayer films.

The surface of a single coat LZO film was investigated further using XPS. The C 1s and O 1s spectra reveal that there are both C and O associated with carbonate in films annealed in ambient air, but not in films annealed under vacuum (289 eV in the C 1s region and 531.5 eV in the O 1s region, Figure 7.4). Most of the carbonate in the air-annealed films is present only at the surface, dissipating after only 60 s of sputtering with Ar^+ ions at 1 keV (~1 nm).

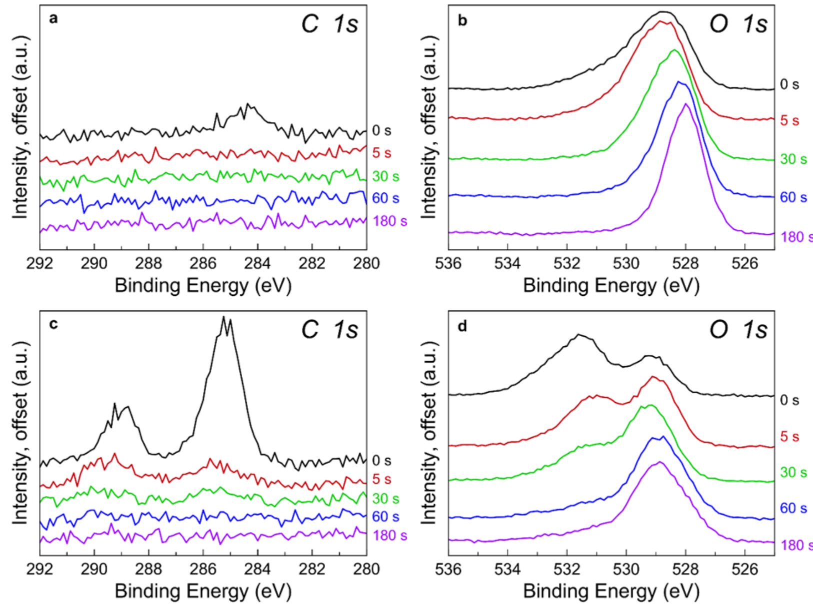

Figure 7.4. (a) C 1s and (b) O 1s XPS spectra of a single-layer LZO film annealed under vacuum and (c) C 1s and (d) O 1s XPS spectra of a LZO film annealed in air for various Ar^{+} (1 keV) sputtering times. Peaks assigned to metal oxides (529 eV) and adventitious carbon (285 eV) are observed in all films studied.

The collective data demonstrate inhomogeneous La and Zr distributions in LZO films, indicating metal atom segregation during film formation. According to glass network theory, small, highly charged ions such as Zr^{4+} act as network formers to form metal oxide networks, whereas larger ions such as La^{3+} act as network modifiers.[60] We postulate that a rigid Zr oxide networks forms relatively early in the film formation process, leaving the La^{3+} ions more mobile within the evolving films. This is supported by previous thermogravimetric analysis studies that indicate that significant mass loss occurs for $ZrO(NO_3)_2$ hydrate powders at much lower temperatures than for $La(NO_3)_3$ hydrate powders.[35] As a film is annealed, water is removed from the film surface. This results in a concentration gradient of La^{3+} ions at the film surface because the rate of evaporation, which concentrates the ions, is apparently faster than the ability of La^{3+} ions to diffuse away from the surface. In multilayer films, this La-rich surface forms for each

individual layer and is 'buried' by the sequential deposition of additional layers. The La-rich surface of the final film absorbs CO_2 from ambient air to form a thin carbonate-containing surface layer either during[61] or after[62] annealing.

As discussed previously, LZO films are of interest as dielectric components for microelectronic devices. To investigate the impact of the observed inhomogeneities on device performance, we fabricated LZO-based MIS devices and used impedance spectroscopy to characterize their dielectric properties (Figure 7.5). In general, dielectric constants increased with increasing number of layers (Figure 7.5a). Loss tangents were similar for all devices studied, although the single-layer devices displayed higher deviations from ideal capacitance at low frequencies (Figure 7.5b).

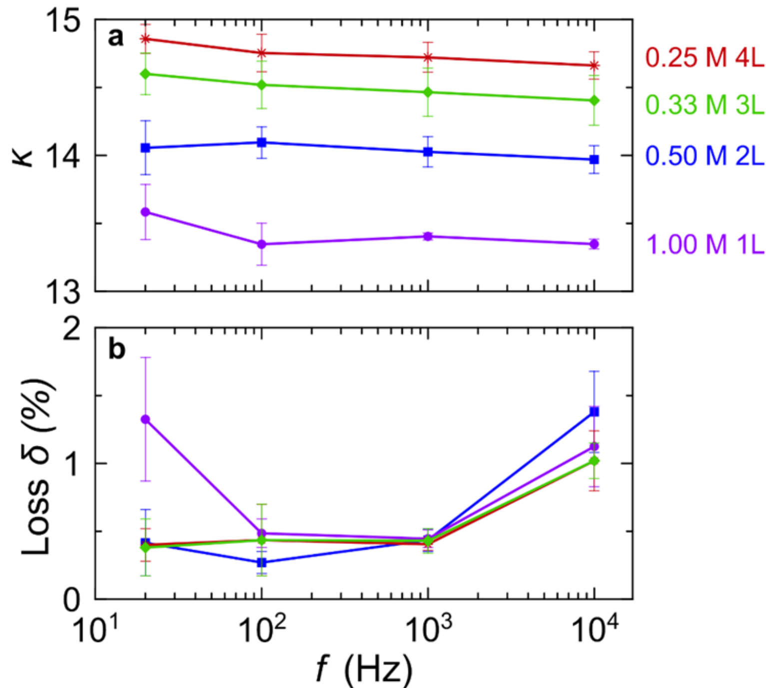

Figure 7.5. (a) Dielectric constants (κ) and (b) loss tangent (loss δ) as a function of frequency for MIS devices made from four, three, two, and one layer LZO films deposited from 0.25, 0.33, 0.50, and 1.00 M precursor solutions, respectively. Error bars were determined from two separate batches of LZO-based devices.

Although multilayer films exhibit enhanced dielectric properties, we are hesitant to attribute this to the increased number of internal interfaces (and inhomogeneities) in these films. The enhanced dielectric properties are likely due to increased condensation and densification of the multilayer films. These films are comprised of multiple thin coats of solution, in which nitrate and water can more readily diffuse to the film surface during the annealing process. In contrast, counterions and water in the single-layer film must diffuse a greater distance to reach the film surface and desorb. In addition, the multilayer films have been annealed cumulatively longer than the single layer film because each individual coat must be "set" with a short anneal. Indeed, XRR modeling indicates that the multilayer films are denser than the single-layer film (Table AD2). Additionally, the HAADF-STEM images and loss tangent data at low frequencies suggest that more mobile species are trapped within the single-layer film. Although we cannot exclude the effects of the internal interfaces, mass transport considerations likely dominate the observed trend in dielectric constants. Regardless of the cause, these results indicate that multilayer films are preferred for optimal device properties.

Conclusion

The composition of non-uniform density profiles was investigated for amorphous multi-metal component LZO dielectrics using a suite of complementary techniques. We observe an inhomogeneous distribution of La and Zr and detail the composition of a La-rich carbonate-containing surface layer in the LZO films. We postulate that the La-rich surface results from concentrating the La^{3+} ions at the film surface as water evaporates, and that a similar effect is not observed for Zr^{4+} ions due to rapid Zr oxide network

formation early in the film formation process. This inhomogeneous distribution of metal components is likely a general phenomenon for multi-metal oxide films deposited from solution. Additionally, because many applications require thicker films than can be prepared with single coats, multilayer films are often used to achieve desired film thicknesses. We show that layering artifacts in multilayer films do not negatively impact dielectric properties, and that the more condensed multilayer films have higher dielectric constants relative to single layer films of the same thickness. Ultimately, understanding the chemical origin and consequences of inhomogeneities will be important for optimizing solution-deposited film properties and their use in devices.

CHAPTER VIII

SUMMARY AND OUTLOOK

This work contributes to the advancement of aqueous deposition methods by addressing major knowledge gaps in three areas. First, all-inorganic aqueous routes to high-quality, high-κ metal oxide dielectrics were developed in Chapters III and IV. Chapter IV also demonstrated the tunability of aqueous approaches, which enables careful optimization of device properties for specific functions. Second, Chapter V detailed the remarkable impact of steam annealing on the evolution of aqueous precursors to the corresponding oxides. This general method reduces residual counterion content in films at annealing temperatures $\leq$ 200 °C via azeotropic evaporation, improves film stability with respect to post-anneal water absorption, and enhances dielectric properties. Third, non-uniform density profiles were linked to composition gradients in single and multi-metal oxides in Chapters VI and VII, respectively. These composition gradients are attributed to enhanced evaporation at the film surface and differences in metal cation network forming ability. Chapter VII also showed that multilayer dielectrics contain less porosity and display higher dielectric constants than single layer films of the same thickness, making them preferred for device applications.

To fully realize the potential advantages of solution-phase deposition over traditional vapor-phase methods, further elucidation and control of the chemistry that occurs during film processing is required. Optimization of deposition and processing conditions will also be important, and development of high-throughput technologies, such as slot die

coating, are critical for widespread incorporation of solution deposition methods into industrial device component manufacturing.

APPENDIX A

CHAPTER III SUPPLEMENTARY INFORMATION

Table AA1: X-ray reflectivity (XRR) best-fit modeling parameters

	Capping Layer			Bulk Layer			Total	
T **(°C)**	***t*** **(nm)**	***D*** **(g cm^{-3})**	***R*** **(nm)**	***t*** **(nm)**	***D*** **(g cm^{-3})**	***R*** **(nm)**	***t*** **(nm)**	***D*** **(g cm^{-3})**
300	0.7	3.33	0.3	50.4	4.35	1.2	51.1	4.35
400	2.1	4.29	0.4	37.8	4.75	0.7	39.9	4.71
500	2.2	4.62	0.4	34.4	5.04	0.6	36.7	4.97
600	1.0	4.37	0.4	32.5	5.30	0.9	33.5	5.27

Table AA1. Best fit XRR modeling parameters for single layer LZO films annealed between 300-600 °C. Best fit models used a two layer fit with a bulk layer capped by a thinner, less dense capping layer. Parameters modeled for the capping and bulk layers were thickness (*t*), density (*D*), and roughness (*R*). Total thickness and the total weighted average density are also shown.

Figure AA1: Dielectric constant dispersion

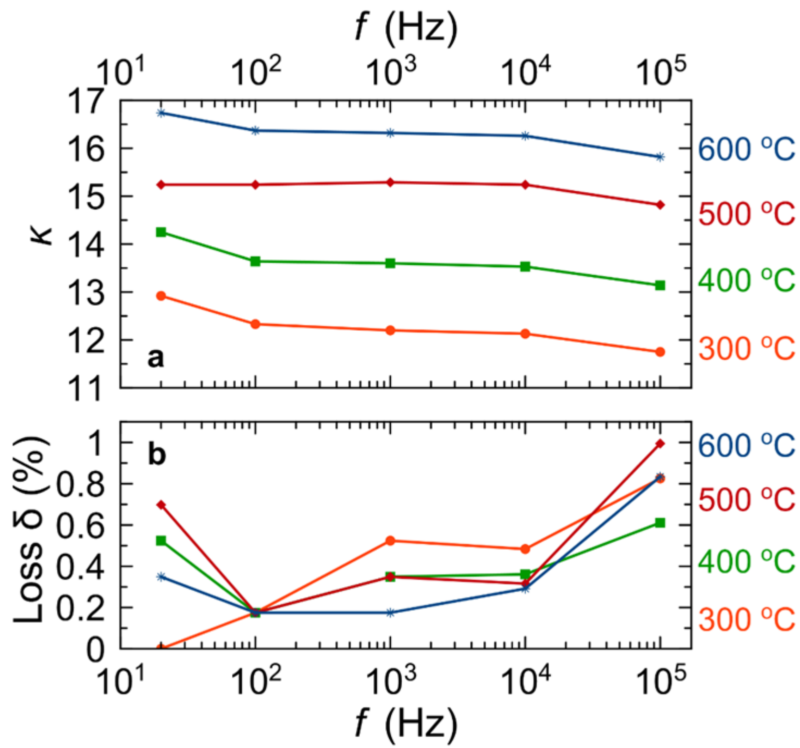

Figure AA1. a) Dielectric constant (κ) as a function of frequency (f) for LZO MIS devices and b) corresponding loss tangents (loss δ) as a function of f.

Figure AA2: Current density-electric field (*J-E*) hysteresis test

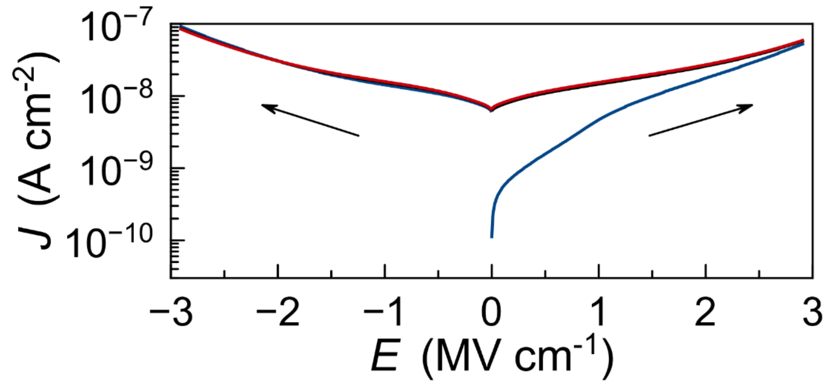

Figure AA2. *J-E* hysteresis test for a MIS device made from a two-coat (~100 nm) LZO film annealed at 500 °C. Voltage was swept from 0 to +30 V, +30 to -30 V, and -30 to 0 V in three successive sweeps. Sweep 1 is shown in blue, sweep 2 is shown in black, and sweep 3 is shown in red (for clarity, only sweeps from 0 to +30 V and from 0 to -30 V are shown).

APPENDIX B

CHAPTER IV SUPPLEMENTARY INFORMATION

Figure AB1: Fourier transform infrared spectroscopy (FTIR) for ZAO films annealed at 300 and 400 °C

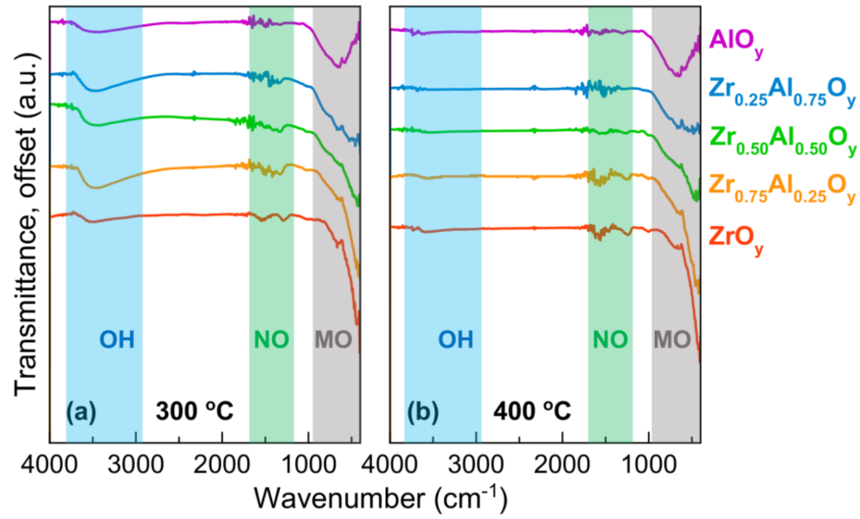

Figure AB1. FTIR spectra of two-coat ZAO films annealed at (a) 300 °C and (b) 400 °C.

Figure AB2: X-ray reflectivity (XRR) spectra and best fit models for ZAO films annealed at 500 °C

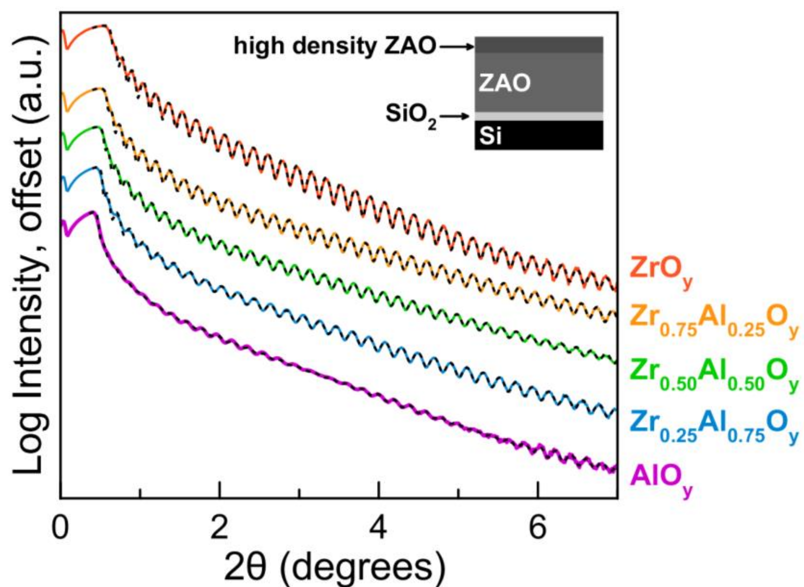

Figure AB2. Representative XRR spectra for single-coat ZAO films annealed at 500 °C (solid, colored) and overlaid best fit models (dashed, black). Best fit models were generated using a two-layer model consisting of a thin (~1-3 nm) capping layer over an underlying bulk layer of different density, consistent with models employed in previous XRR studies on aqueous-derived metal oxides.[1,2]

Figure AB3: Film thickness and density of ZAO films extracted from XRR best fit models

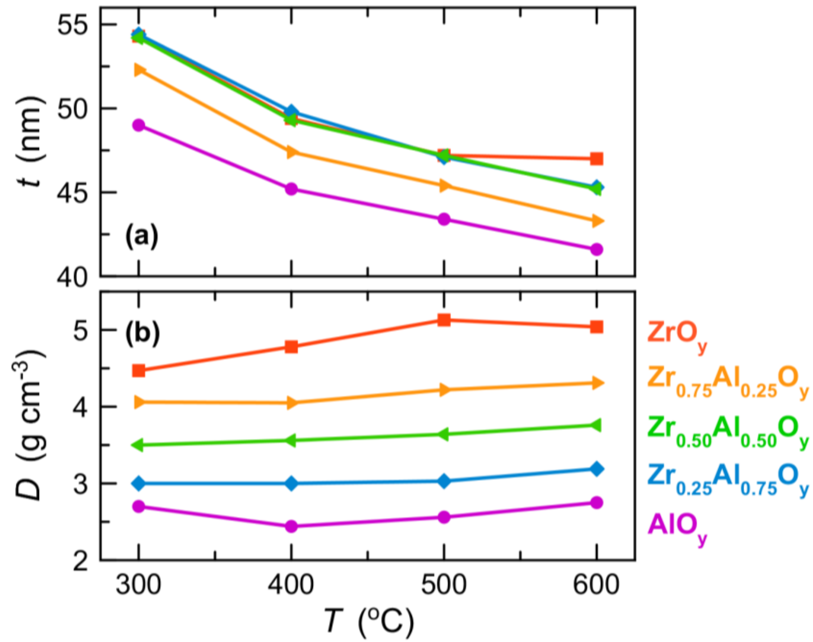

Figure AB3. (a) Film thickness [*t*] and (b) density [*D*] of single-coat ZAO films extracted from XRR best fit, two-layer models. Small differences in film thickness between compositions are attributed to small differences in the humidity of the spin-coating chamber during deposition.[3] Density values are calculated from a weighted average of the capping and bulk layer densities.

Figure AB4: Dielectric constant dispersion

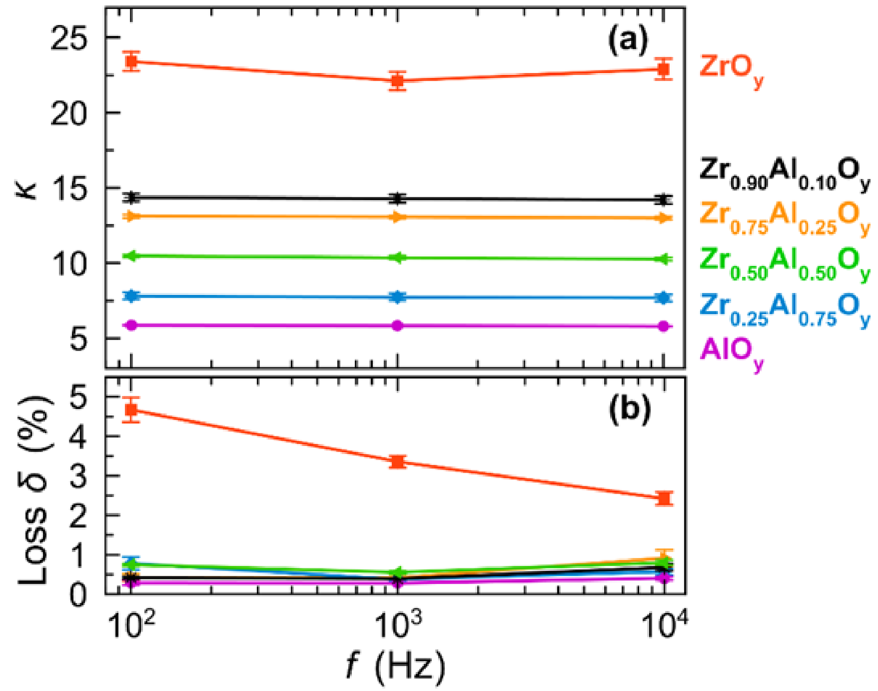

Figure AB4. (a) Dielectric constants [*κ*] as a function of frequency [*f*] for ZAO-based MIS devices and (b) corresponding loss tangents [loss *δ*] as a function of *f*. MIS devices were fabricated from two-coat (~100 nm) ZAO films annealed at 500 °C. Error bars were determined using measurements taken from three separate batches of MIS devices.

APPENDIX C

CHAPTER V SUPPLEMENTARY INFORMATION

Scheme AC1: Steam annealing apparatus

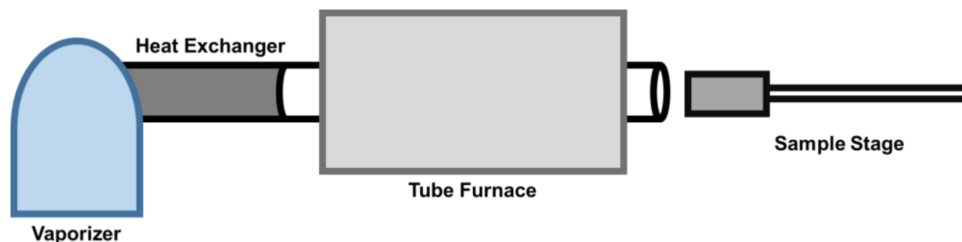

Scheme AC1. A cartoon schematic of the steam annealing apparatus, consisting of a tube furnace equipped with a water vaporizer (connected by Al tubing heated at ~70 °C) and a removable sample heating stage. The tube furnace was kept at 125 °C, while the sample stage was ramped up to the desired annealing temperature (rate = 25 °C min^{-1}). The water vapor content was kept constant with a flow rate of ~5.3 mL min^{-1}.

Figure AC1: Fourier transform infrared (FTIR) spectra for ZnO, YAO, and LZO (NO_3^-) films

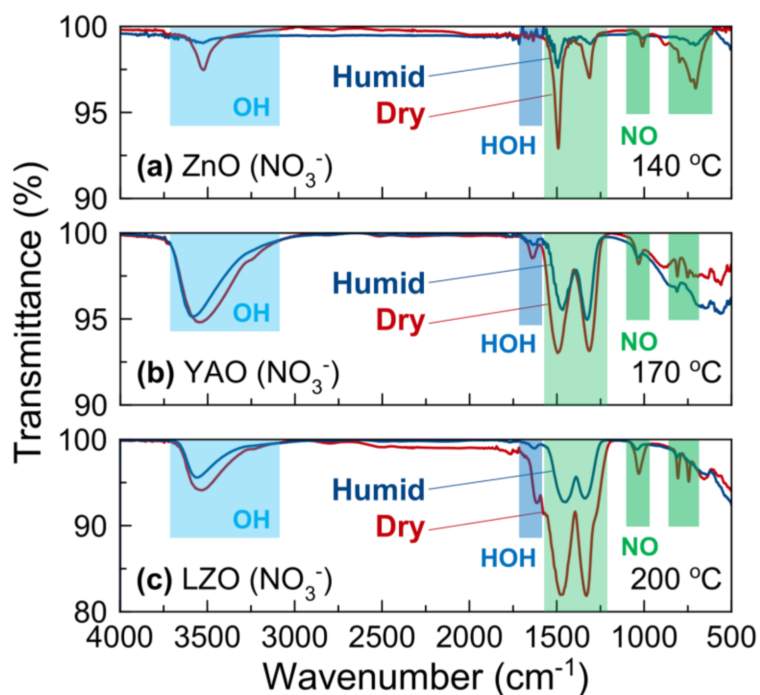

Figure AC1. FTIR spectra of (a) ZnO, (b) YAO, and (c) LZO films deposited from 1.8 M aqueous nitrate precursors and annealed under dry (red) or humid (blue) conditions at various temperatures. Peak assignments (colored bands) are consistent with previous reports.[1–4]

Figure AC2: Photographs of LZO (NO_3^-/Cl^-) films before and after water absorption

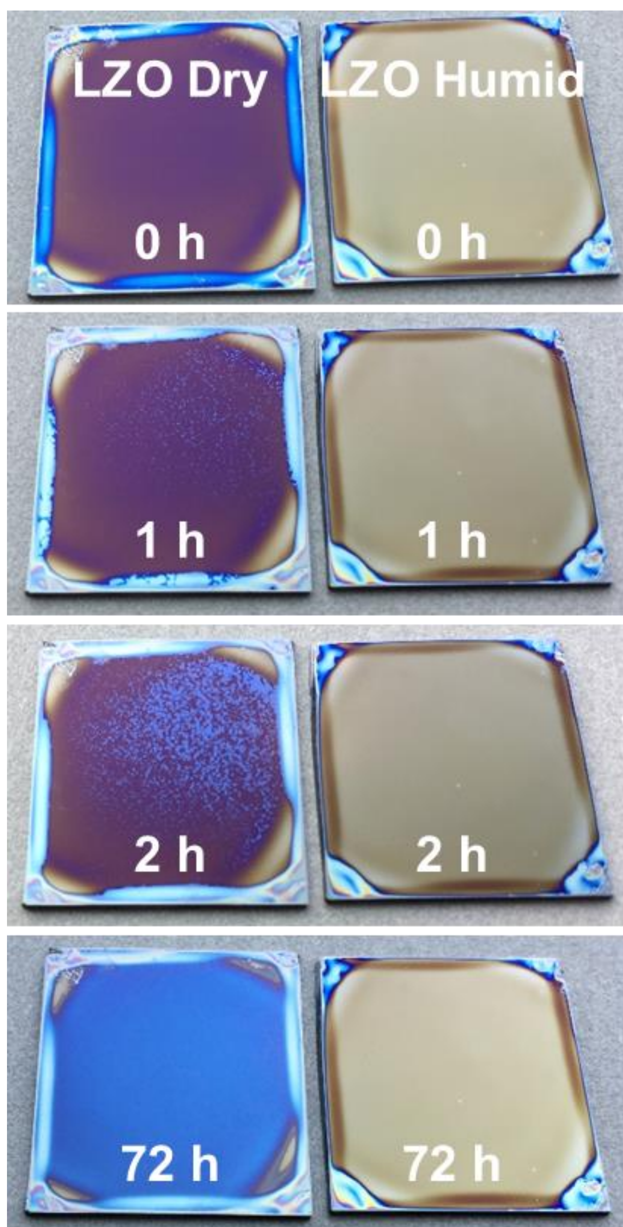

Figure AC2. Photographs of LZO films deposited from a 1.0 M solution (NO_3^-/Cl^- precursors) and annealed under dry or humid conditions at 200 °C. Films were photographed immediately after annealing (0 h) and then after 1, 2, and 72 h of exposure to ambient air. Humid-annealed films retained their visual appearance after >72 h of exposure to air, whereas dry-annealed films changed dramatically. Some variability was observed in dry-annealed films, with some films beginning to visibly change after ~15 min of exposure to air and becoming full cloudy and discolored after ~1 h. This variability is attributed to relative humidity differences in the ambient air.

Figure AC3: Atomic force microscopy (AFM) images of LZO (NO_3^-) films

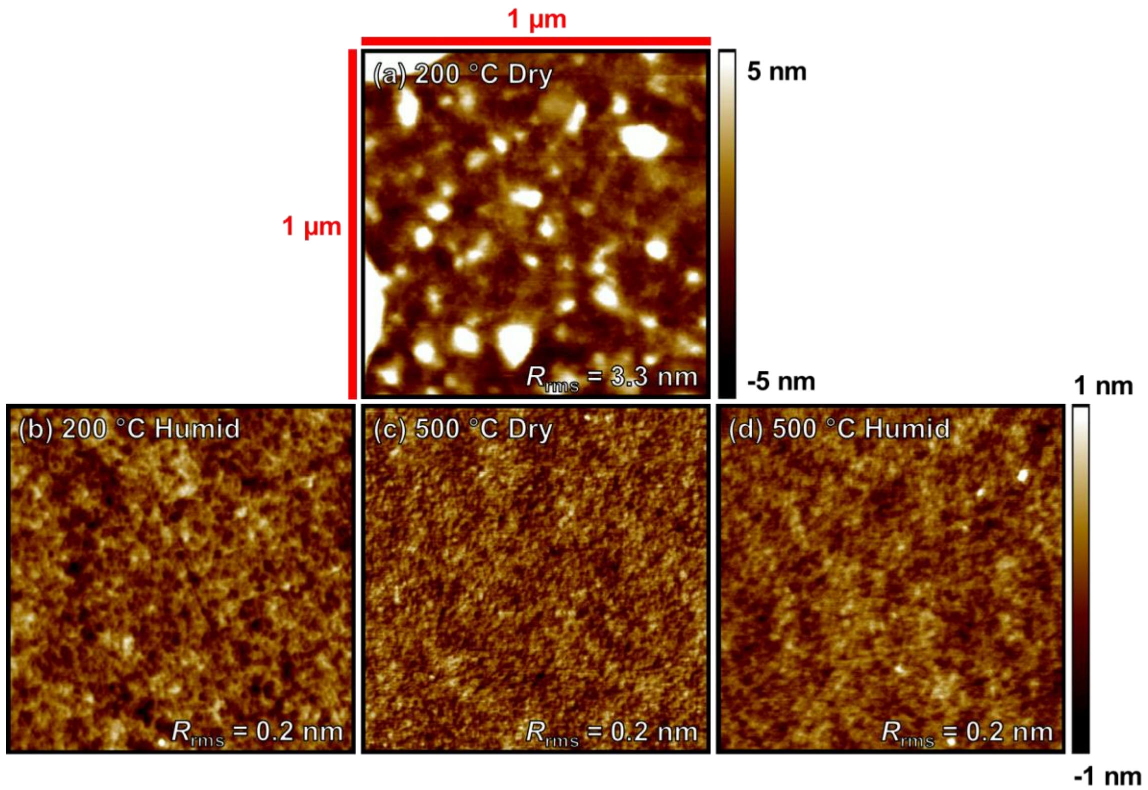

Figure AC3. Representative AFM images (1 X 1 μm^2) taken of LZO films deposited from a 1.0 M solution (NO_3^- precursors). Films were annealed at (a) 200 °C under dry conditions, (b) 200 °C under humid conditions, (c) 500 °C under dry conditions, and (d) 500 °C under humid conditions. Sample height is indicated by color scales, with image (a) having a different scale than images (b-d). The root-mean-square roughness (R_{rms}) for each image is also given.

Figure AC4: FTIR water absorption stability data for LZO (NO_3^-) films

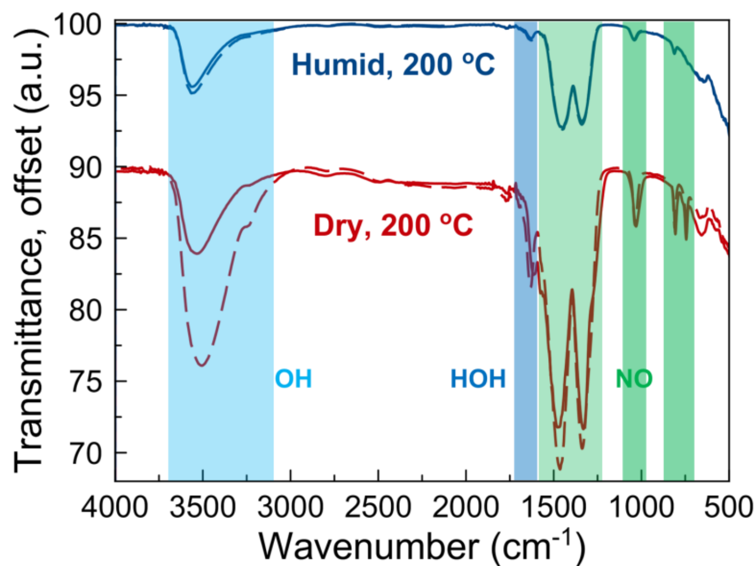

Figure AC4. FTIR spectra of LZO films deposited from a 1.8 M solution (NO_3^- precursors) and annealed under dry (red) or humid (blue) conditions at 200 °C. Solid lines are data taken immediately after annealing and dashed lines are data taken after 1 h in ambient lab air (~45% relative humidity).

X-ray photoelectron (XPS) peak fitting analysis

The C 1s and O 1s XPS spectra were analyzed using Thermo Scientific Avantage 5.94 software to determine differences in carbonate and/or hydroxide content at the film surface for the two different annealing methods. The C 1s spectra were fit with five peaks (linear background), four for adventitious carbon species and one for carbonate species: C-H (peak A) at 284.8 eV, C-O (peak B) at A + 1.5(± 0.3) eV, C=O (peak C) at A + 3.0(± 0.3) eV, O=C-O (peak D) at A + 4.0(± 0.3) eV, and CO_3^{2-} (peak E) at A + 4.5(± 0.3) eV, consistent with energy ranges reported by Moulder et al.[5] All peaks were constrained to have the same FWHM and Lorentzian/Gaussian (L/G) ratio, both of which were fit by the software. The FWHM and L/G ratios obtained for the 200 °C samples were 1.63 and 1.20 for the humid-annealed sample and 1.67 and 0.39 for the dry-annealed sample. The FWHM and L/G ratios obtained for the 500 °C samples were 1.59 and 0.21 for the humid-annealed sample and 1.75 and 0.19 for the dry-annealed sample.

The O 1s spectra was fit with five or four peaks for the 200 and 500 °C samples, respectively. In the case of the 200 °C samples, five peaks were used, without binding energy constraints, starting from low to high binding energy: O^{2-} from La (peak F), O^{2-} from Zr (peak G), O^{2-} from CO_3^{2-} (peak H), O^{2-} from NO_3^- (peak I), and O from adventitious carbon-oxygen species (peak J). In the case of the 500 °C samples, four peaks were used, without binding energy constraints, starting from low to high binding energy: O^{2-} from La (peak F), O^{2-} from Zr (peak G), O^{2-} from CO_3^{2-} (peak H), and O from adventitious carbon-oxygen species (peak J). Peak H was constrained to three times the atomic percentage as peak E, and peak J was constrained to the atomic percentage of peaks B + C + D to account for all carbon-oxygen species. For the 200 °C samples and

for the 500 °C humid sample, peak H was not constrained since a larger atomic percentage was needed to get a reasonable fit, presumably due to the presence of hydroxide adding to the peak intensity. All O 1s peaks were constrained to the same FWHM and L/G ratio, which were fit by the software. The FWHM and L/G ratios obtained for the 200 °C samples were 1.53 and 6.03 for the humid-annealed sample and 1.59 and 10.26 for the dry-annealed sample. The FWHM and L/G ratios obtained for the 500 °C samples were 1.65 and 0.39 for the humid-annealed sample and 1.52 and 0.72 for the dry-annealed sample. The position of the La-O, Zr-O, CO_3^{2-}, N-O, and C-O species are consistent with previous reports.[5–9]

The La 3d spectra of the humid- and dry-annealed 500 °C samples were overlaid and auto-scaled (using Avantage) in order to directly compare peak splitting and intensity ratios. To avoid background subtraction issues, quantification of La for all LZO samples was achieved by using only the La $3d_{5/2}$ peaks.

Figure AC5: XPS C 1s, O 1s, Cl 2s, N 1s, La 3d, and Zr 3d spectra for LZO (NO_3^-/Cl^-) films annealed at 200 °C

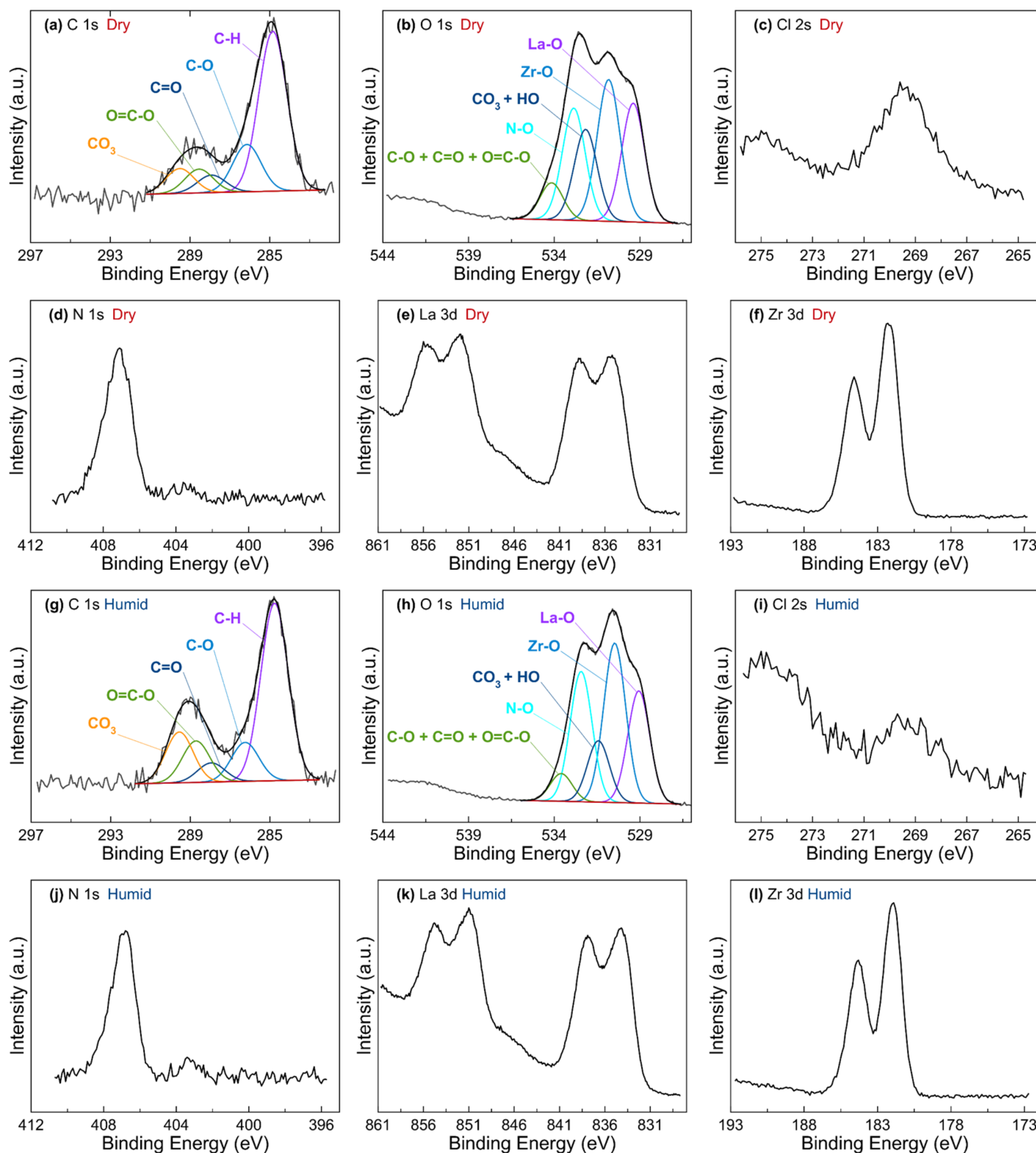

Figure AC5. XPS spectra of LZO films deposited from a 1.0 M solution (NO_3^-/Cl^- precursors) and annealed under dry or humid conditions at 200 °C: C 1s (a,g), O 1s (b,h), Cl 2s (c, i), N 1s (d, j), La 3d (e, k), and Zr 3d (f, l). The C 1s (a, g) and O 1s (b, h) data were fit using Avantage peak fitting software, and raw data are shown in gray, envelope peak fits are shown in black, and linear backgrounds are shown in red. Individual fit peaks corresponding to specific C or O species are labeled and color-coded.

Table AC1: XPS atomic percentages for fitted C 1s and O 1s spectra for LZO (NO_3^-/Cl^-) films annealed at 200 °C

C Species	At. % Dry	At. % Humid	O Species	At. % Dry	At. % Humid
C-H	5.5	6.1	La-O	14.4	14.2
C-O	1.6	1.3	Zr-O	17.2	20.2
C=O	0.6	0.7	CO_3	-	-
O=C-O	0.8	1.4	CO_3 + HO	11.0	7.8
CO_3	0.8	1.7	N-O	13.6	16.5
			C-O + C=O + O=C-O	4.5	3.5

Table AC1. C and O atomic percentages from XPS peak fitting shown in Figure S5 (see Table S2 for a complete list of atomic percentages).

Table AC2: XPS atomic percentages for La, Zr, O, C, Cl, and N species for LZO (NO_3^-/Cl^-) films annealed at 200 °C

	La	**Zr**	**O**	**C**	**Cl**	**N**
At. % Dry	10.3	8.3	60.6	9.4	3.5	7.9
At. % Humid	12.8	6.7	62.2	11.2	0.7	6.4

Table AC2. XPS atomic percentages for LZO films deposited from a 1.0 M solution (NO_3^-/Cl^- precursors) and annealed under dry or humid conditions at 200 °C.

Figure AC6: XPS Cl 2s, N 1s, and Zr 3d spectra for LZO (NO_3^-/Cl^-) films annealed at 500 °C

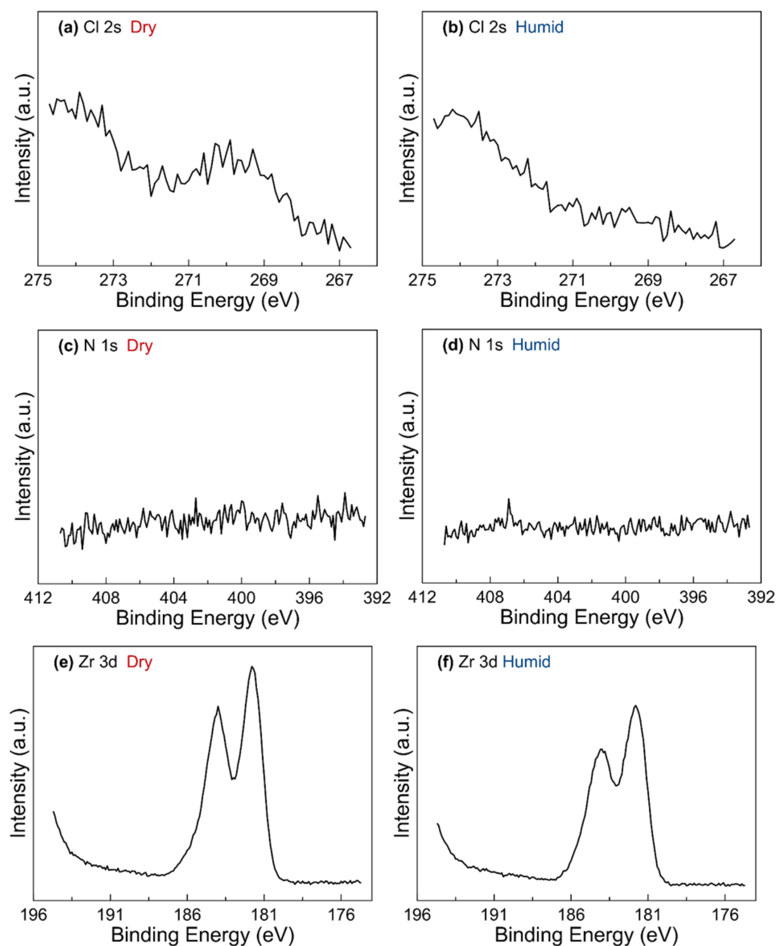

Figure AC6. XPS spectra of LZO films deposited from a 1.0 M solution (NO_3^-/Cl^- precursors) and annealed under dry or humid conditions at 500 °C: Cl 2s (a, b), N 1s (c, d), and Zr 3d (e, f).

Table AC3: XPS atomic percentages for La, Zr, O, C, Cl, and N species for LZO (NO_3^-/Cl^-) films annealed at 500 °C

	La	Zr	O	C	Cl	N
At. % Dry	12.1	11.8	58.3	16.7	1.1	0
At. % Humid	14.9	10.8	61.7	12.6	0	0

Table AC3. XPS atomic percentages for LZO films deposited from a 1.0 M solution (NO_3^-/Cl^- precursors) and annealed under dry and humid conditions at 500 °C.

Figure AC7: Grazing incidence X-ray diffraction (GIXRD) data for LZO (NO_3^-) films

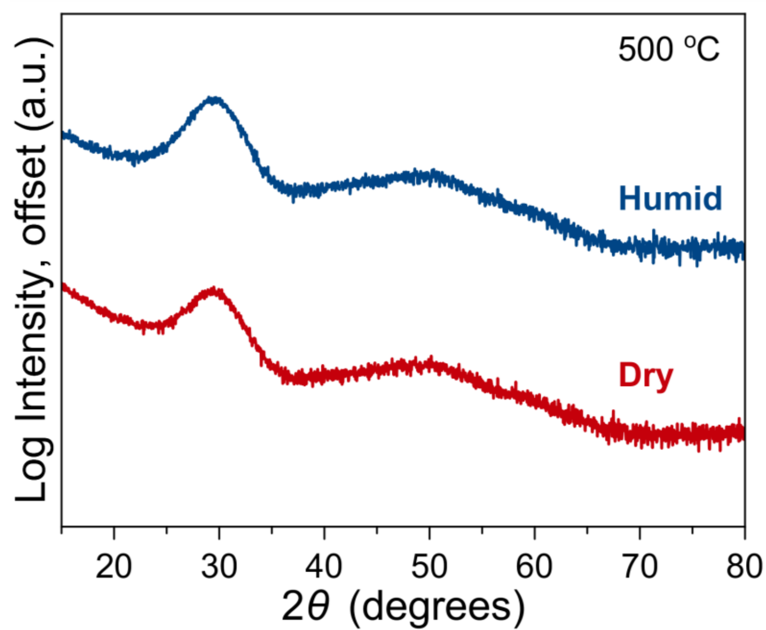

Figure AC7. GIXRD spectra for LZO films deposited from a 1.0 M solution (NO_3^- precursors) and annealed at 500 °C under dry (red) or humid (blue) conditions.

Figure AC8: Scanning electron microscopy (SEM) images of LZO (NO_3^-) films

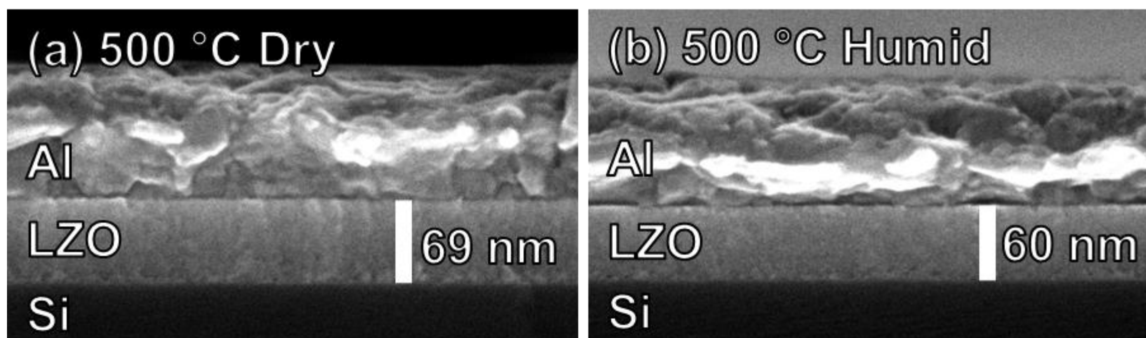

Figure AC8. SEM images of LZO films deposited from a 1.5 M solution (NO_3^- precursors) and annealed at 500 °C under (a) dry or (b) humid conditions.

Figure AC9: Current density-electric field (*J*-*E*) data for LZO-based (NO_3^-) MIS devices

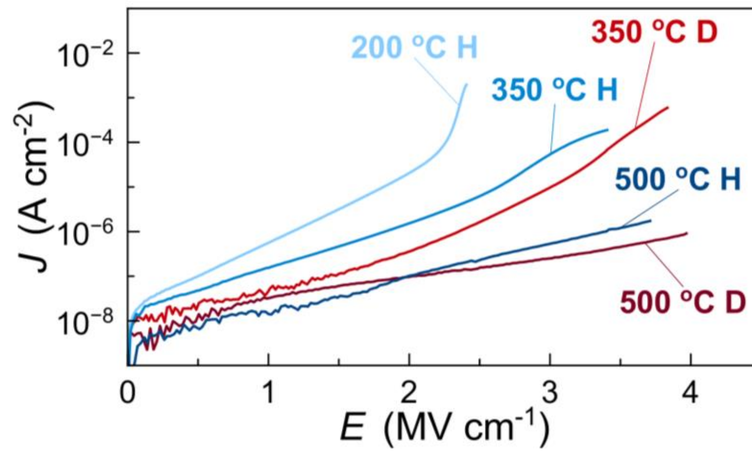

Figure AC9. *J*-*E* data for MIS devices fabricated from two-coat LZO (NO_3^-, 1.0 M) films (~100 nm) annealed under dry (red traces) or humid (blue traces) conditions at various temperatures.

APPENDIX D

CHAPTER VII SUPPLEMENTARY INFORMATION

Figure AD1: Fourier transform infrared (FTIR) spectra

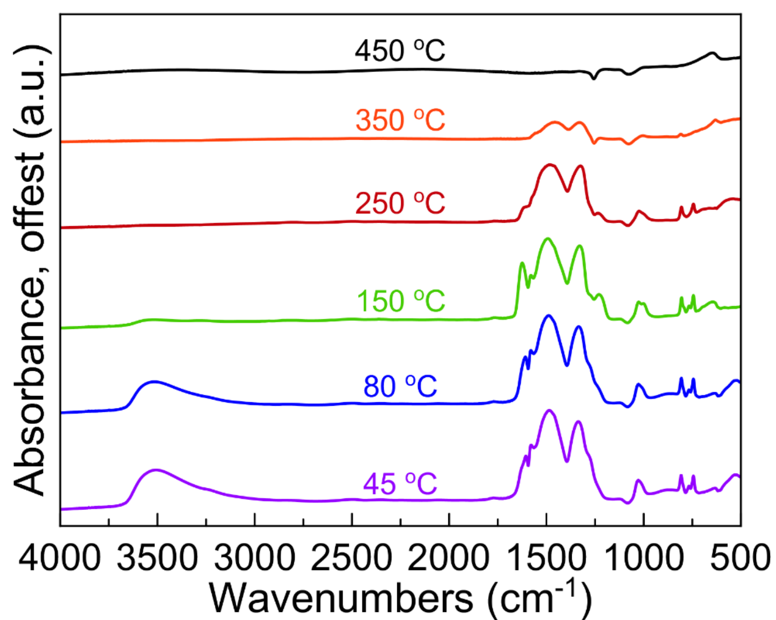

Figure AD1. FTIR spectra of a single layer LZO film deposited from a 1.00 M precursor solution sequentially heated in situ to various annealing temperatures.

X-ray reflectivity (XRR) modeling procedure

The XRR spectra were fit using Bede REFS software, which generates a solution based on an initial model input and a genetic algorithm to minimize residuals. Two types of model inputs were used: a homogeneous, single layer model and a model with multiple layers informed by HAADF-STEM studies. An approximate total thickness of 40 nm was used as an initial starting thickness for each model. For the more complex models, the thickness of the individual layers was approximated from the HAADF-STEM images. In all cases, the thickness, density, and roughness of each individual layers were allowed to vary independently. After producing the best fit, the models were perturbed to ensure that they had each settled in a global minimum. Goodness of Fit (GOF) values were output by the modeling program and indicate the quality of the model fitting.

Figure AD2: XRR homogeneous single layer best fit models

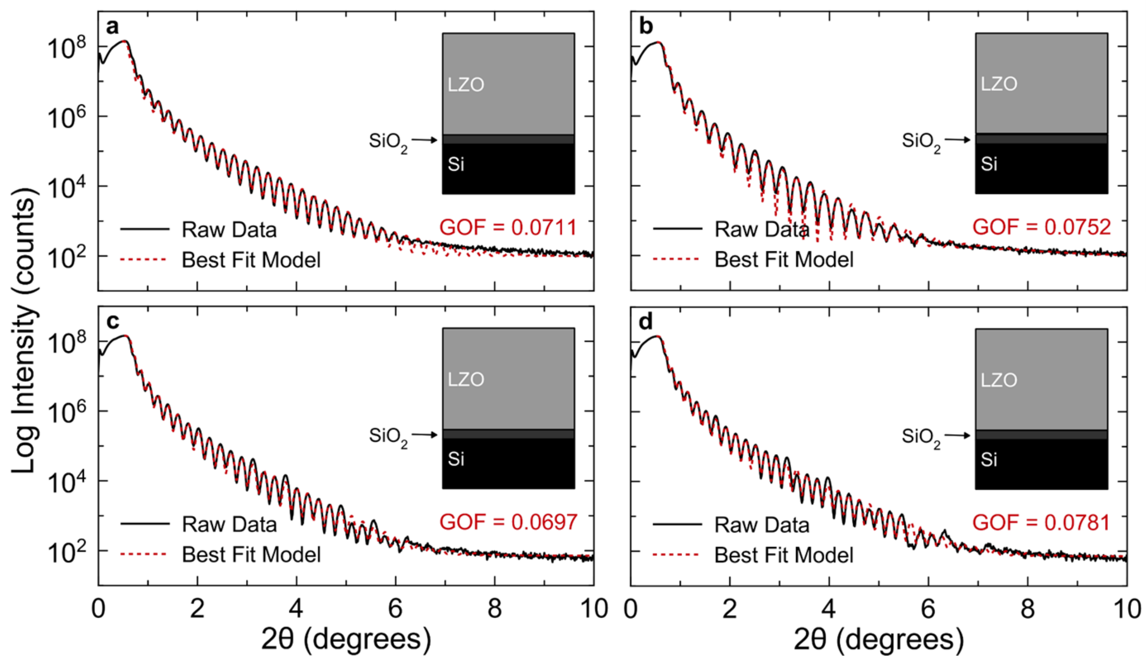

Figure AD2. Single layer models fit to XRR data collected from (a) one, (b) two, (c) three, and (d) four coat films deposited from 1.00, 0.50, 0.33, and 0.25 M precursor solutions, respectively.

Table AD1: XRR single layer best fit model parameters

	Single Layer Best Fit Parameters		
Layer(s)	***t* (nm)**	***D* (g cm^{-3})**	***R* (nm)**
1L Film			
LZO	38.0	5.83	0.3
2L Film			
LZO	31.1	6.04	0.5
3L Film			
LZO	39.2	5.89	0.4
4L Film			
LZO	41.7	5.95	0.4

Table AD1. XRR single layer best fit model parameters [thickness (*t*), density (*D*), roughness(*R*)] for XRR data and models presented in Figure AD2.

Figure AD3: XRR inhomogeneous multilayer best fit models

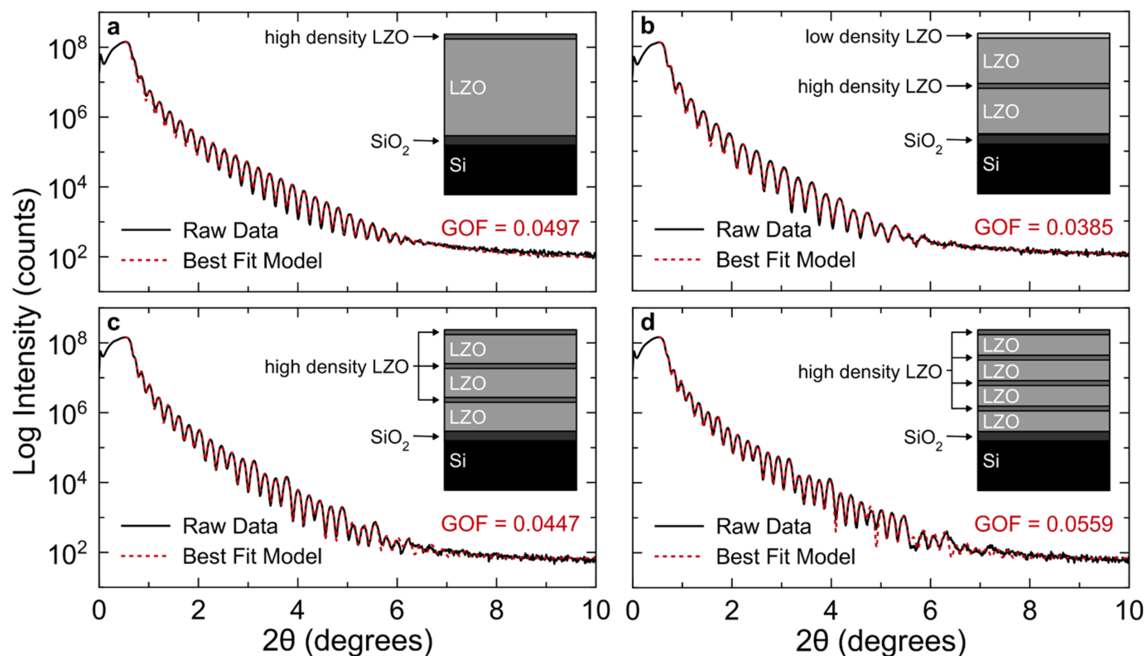

Figure AD3. Multilayer models fit to XRR data collected from (a) one, (b) two, (c) three, and (d) four coat films deposited from 1.00, 0.50, 0.33, and 0.25 M precursor solutions, respectively. Starting models were informed by HAADF-STEM images.

Table AD2: XRR multilayer best fit model parameters

	Multilayer Best Fit Parameters		
Layer(s)	***t* (nm)**	***D* (g cm^{-3})**	***R* (nm)**
1L Film			
LZO 1	1.71	5.79	0.3
LZO 2	36.2	5.36	0.1
2L Film			
LZO 1	0.9	5.02	0.3
LZO 2	13.1	5.85	0.1
LZO 3	1.1	5.71	0.3
LZO 4	16.1	5.89	0.2
3L Film			
LZO 1	1.8	5.89	0.4
LZO 2	12.6	5.71	0.1
LZO 3	1.2	6.02	0.2
LZO 4	13.1	5.78	0.3
LZO 5	1.3	6.04	0.2
LZO 6	9.2	5.86	0.1
4L Film			
LZO 1	1.8	6.03	0.4
LZO 2	9.9	5.63	0.7
LZO 3	1.3	6.00	0.1
LZO 4	9.8	5.62	0.8
LZO 5	1.2	6.00	0.1
LZO 6	10.0	5.69	0.8
LZO 7	1.3	6.04	0.1
LZO 8	6.6	5.91	0.3

Table AD2. XRR multilayer best fit model parameters [thickness (*t*), density (*D*), roughness(*R*)] for XRR data and models presented in Figure AD3.

Figure AD4: Energy-dispersive X-ray spectroscopy (EDS) measurements

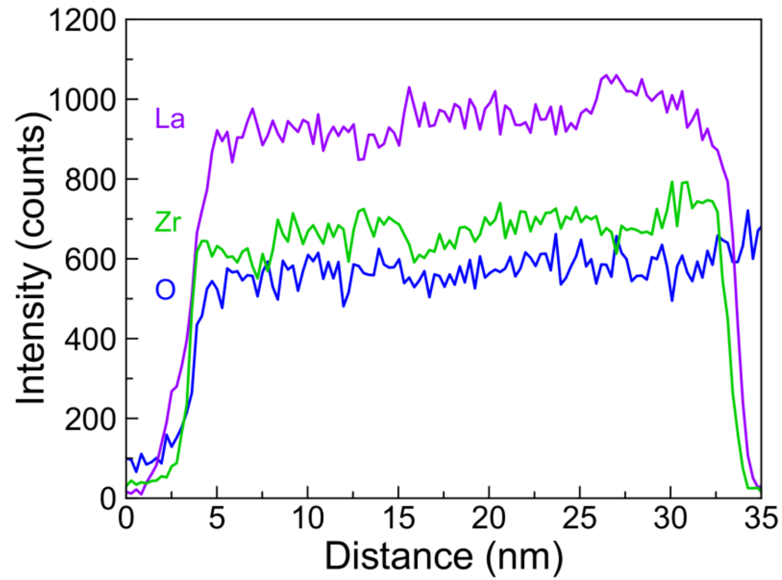

Figure AD4. Cross-sectional STEM-EDS profiles from a three layer LZO film deposited from a 0.33 M precursor solution. Intensity profiles plotted are the O Kα, La Lα, and Zr Lα signals vs. distance from the film surface (where a distance of zero is the film surface).

Table AD3: Electron probe microanalysis (EPMA) measurements

Precursor Molarity	Layers	La at%	Zr at%	N at%	O at%	La/Zr	(La+Zr)/O	(La+Zr)/(O+N)
1.00	1	14.8(1)	14.6(1)	5.6(5)	65.1(3)	1.01(1)	0.45(1)	0.42(1)
0.50	2	15.3(2)	15.2(1)	3.8(6)	65.7(4)	1.01(2)	0.46(1)	0.44(1)
0.33	3	15.5(1)	15.1(1)	2.9(4)	66.5(3)	1.03(1)	0.46(1)	0.44(1)
0.25	4	15.9(1)	15.6(1)	2.4(6)	66.2(6)	1.02(1)	0.48(1)	0.46(1)

Table AD3. Atomic ratios measured using EPMA with 95% confidence intervals from 5 EPMA measurements (uncertainty indicated in parentheses).

Figure AD5: Medium energy ion scattering (MEIS) data and best fit model

He ions that scatter from larger masses are detected at higher energies. Therefore, the highest energy peak corresponds to ions backscattered from La in the film, while the lower energy peak corresponds to ions backscattered from Zr.

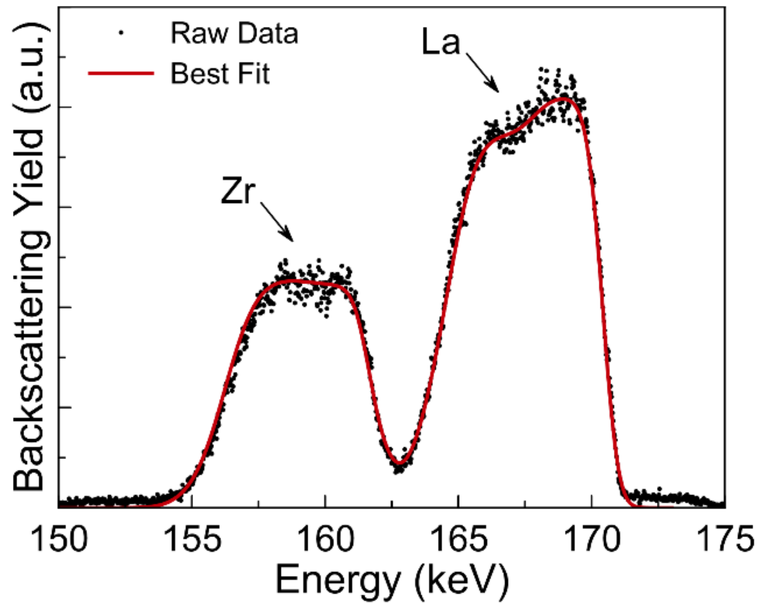

Figure AD5. MEIS experimental data (black) collected from a thin two layer (~8 nm) film overlaid with the best fit model (red) indicates a surface enrichment of La whereas the amount of Zr throughout the film is essentially constant.

Table AD4: X-ray photoelectron spectroscopy (XPS) measurements

Films were sputtered with 1 keV Ar^+ ions for a total of three minutes (~3-4 nm). The composition was determined by using XPS peak area analysis in the MultiPak Software.

	Air-Annealed LZO film	
Sputter (s)	**La 3d (%)**	**Zr 3d (%)**
0	57.5	42.5
5	62.6	37.4
30	62.1	37.9
60	59.4	40.6
180	57.2	42.8

Figure AD4. Relative La and Zr atomic percentages for a one layer LZO film deposited from a 0.33 M precursor solution and annealed to 450 °C in an ambient environment.

REFERENCES CITED

Chapter I

(1) Yu, X.; Marks, T. J.; Facchetti, A. Metal Oxides for Optoelectronic Applications. *Nat. Mater.* **2016**, *15*, 383–396.

(2) Trotochaud, L.; Boettcher, S. W. Precise Oxygen Evolution Catalysts: Status and Opportunities. *Scr. Mater.* **2014**, *74*, 25–32.

(3) Burke, M. S.; Zou, S.; Enman, L. J.; Kellon, J. E.; Gabor, C. A.; Pledger, E.; Boettcher, S. W. Revised Oxygen Evolution Reaction Activity Trends for First-Row Transition-Metal (Oxy)hydroxides in Alkaline Media. *J. Phys. Chem. Lett.* **2015**, *6*, 3737–3742.

(4) Whittingham, M. S. Lithium Batteries and Cathode Materials. *Chem. Rev.* **2004**, *104*, 4271–4301.

(5) Thangadurai, V.; Narayanan, S.; Pinzaru, D. Garnet-Type Solid-State Fast Li Ion Conductors for Li Batteries: Critical Review. *Chem. Soc. Rev.* **2014**, *43*, 4714–4727.

(6) Niklasson, G. A.; Granqvist, C. G. Electrochromics for Smart Windows: Thin Films of Tungsten Oxide and Nickel Oxide, and Devices Based on These. *J. Mater. Chem.* **2007**, *17*, 127–156.

(7) Granqvist, C. G. Electrochromics for Smart Windows: Oxide-Based Thin Films and Devices. *Thin Solid Films* **2014**, *564*, 1–38.

(8) Street, R. A. Thin-Film Transistors. *Adv. Mater.* **2009**, *21*, 2007–2022.

(9) Park, J. S.; Maeng, W.-J.; Kim, H.-S.; Park, J.-S. Review of Recent Developments in Amorphous Oxide Semiconductor Thin-Film Transistor Devices. *Thin Solid Films* **2012**, *520*, 1679–1693.

(10) Fortunato, E.; Barquinha, P.; Martins, R. Oxide Semiconductor Thin-Film Transistors: A Review of Recent Advances. *Adv. Mater.* **2012**, *24*, 2945–2986.

(11) Kuo, Y. Thin Film Transistor Technology—Past, Present, and Future. *Electrochem. Soc. Interface* **2013**, *22*, 55–61.

(12) Robertson, J.; Wallace, R. M. High-K Materials and Metal Gates for CMOS Applications. *Mater. Sci. Eng. R* **2015**, *88*, 1–41.

(13) George, S. M. Atomic Layer Deposition: An Overview. *Chem. Rev.* **2010**, *110*, 111–131.

(14) Mattox, D. M. Physical Vapor Deposition (PVD) Processes. *Met. Finish.* **1995**, *93*, 387–400.

(15) Christen, H. M.; Eres, G. Recent Advances in Pulsed-Laser Deposition of Complex Oxides. *J. Phys. Condens. Matter* **2008**, *20*, 264005.

(16) Bräuer, G.; Szyszka, B.; Vergöhl, M.; Bandorf, R. Magnetron Sputtering – Milestones of 30 Years. *Vacuum* **2010**, *84*, 1354–1359.

(17) Thompson, A. G. MOCVD Technology for Semiconductors. *Mater. Lett.* **1997**, *30*, 255–263.

(18) Leskelä, M.; Ritala, M. Atomic Layer Deposition (ALD): From Precursors to Thin Film Structures. *Thin Solid Films* **2002**, *409*, 138–146.

(19) Kim, J.-H.; Kim, J.-Y.; Kang, S.-W. Film Growth Model of Atomic Layer Deposition for Multicomponent Thin Films. *J. Appl. Phys.* **2005**, *97*, 93505.

(20) Nilsen, O.; Rauwel, E.; Fjellvåg, H.; Kjekshus, A. Growth of $La_{1-x}Ca_xMnO_3$ Thin Films by Atomic Layer Deposition. *J. Mater. Chem.* **2007**, *17*, 1466–1475.

(21) Thomas, S. R.; Pattanasattayavong, P.; Anthopoulos, T. D. Solution-Processable Metal Oxide Semiconductors for Thin-Film Transistor Applications. *Chem. Soc. Rev.* **2013**, *42*, 6910–6923.

(22) Park, S.; Kim, C.-H.; Lee, W.-J.; Sung, S.; Yoon, M.-H. Sol-Gel Metal Oxide Dielectrics for All-Solution-Processed Electronics. *Mater. Sci. Eng., R* **2017**, *114*, 1–22.

(23) Gaskell, J. M.; Jones, A. C.; Aspinall, H. C.; Taylor, S.; Taechakumput, P.; Chalker, P. R.; Heys, P. N.; Odedra, R. Deposition of Lanthanum Zirconium Oxide High-κ Films by Liquid Injection Atomic Layer Deposition. *Appl. Phys. Lett.* **2007**, *91*, 112912.

(24) Gaskell, J. M.; Jones, A. C.; Chalker, P. R.; Werner, M.; Aspinall, H. C.; Taylor, S.; Taechakumput, P.; Heys, P. N. Deposition of Lanthanum Zirconium Oxide High-κ Films by Liquid Injection ALD and MOCVD. *Chem. Vap. Depos.* **2007**, *13*, 684–690.

(25) Alessandri, M.; Del Vitto, A.; Piagge, R.; Sebastiani, A.; Scozzari, C.; Wiemer, C.; Lamagna, L.; Perego, M.; Ghidini, G.; Fanciulli, M. Rare Earth-Based High-κ Materials for Non-Volatile Memory Applications. *Microelectron. Eng.* **2010**, *87*, 290–293.

(26) Je, S. Y.; Son, B.-G.; Kim, H.-G.; Park, M.-Y.; Do, L.-M.; Choi, R.; Jeong, J. K. Solution-Processable $LaZrO_x/SiO_2$ Gate Dielectric at Low Temperature of 180 °C for High-Performance Metal Oxide Field-Effect Transistors. *ACS Appl. Mater. Interfaces* **2014**, *6*, 18693–18703.

(27) Woods, K. N.; Chiang, T.-H.; Plassmeyer, P. N.; Kast, M. G.; Lygo, A. C.; Grealish, A. K.; Boettcher, S. W.; Page, C. J. High-κ Lanthanum Zirconium Oxide Thin Film Dielectrics from Aqueous Solution Precursors. *ACS Appl. Mater. Interfaces* **2017**, *9*, 10897–10903.

(28) Suchanek, W. L.; Watanabe, T.; Sakurai, B.; Kumagai, N.; Yoshimura, M. A Solution Flow System for Hydrothermal–Electrochemical Growth of Multilayered Thin Films. *Rev. Sci. Instrum.* **1999**, *70*, 2432–2437.

(29) Weidman, T.; Lu, Y.; Nault, M. P.; Barnes, M.; Moghadam, F. Ultrasonic Spray Coating of Liquid Precursor for Low κ Dielectric Coatings. U.S. Patent 6,583,071, 2003.

(30) Lee, W.-J.; Park, W.-T.; Park, S.; Sung, S.; Noh, Y.-Y.; Yoon, M.-H. Large-Scale Precise Printing of Ultrathin Sol-Gel Oxide Dielectrics for Directly Patterned Solution-Processed Metal Oxide Transistor Arrays. *Adv. Mater.* **2015**, *27*, 5043–5048.

(31) Adamopoulos, G.; Bashir, A.; Gillin, W. P.; Georgakopoulos, S.; Shkunov, M.; Baklar, M. A.; Stingelin, N.; Bradley, D. D. C.; Anthopoulos, T. D. Structural and Electrical Characterization of ZnO Films Grown by Spray Pyrolysis and Their Application in Thin-Film Transistors. *Adv. Funct. Mater.* **2011**, *21*, 525–531.

(32) Takata, R.; Neumann, A.; Weber, D.; Pham, D.-V.; Anselmann, R.; Kitamura, Y.; Kakimura, T.; Suzuki, S.; Minami, S.; Kodama, M. Scalability and Homogeneity of Slot Die-Coated Metal Oxide Semiconductor for TFTs. *J. Soc. Inf. Disp.* **2016**, *24*, 381–385.

(33) Fukuda, K.; Someya, T. Recent Progress in the Development of Printed Thin-Film Transistors and Circuits with High-Resolution Printing Technology. *Adv. Mater.* **2017**, *29*, 1602736.

(34) Kast, M. G.; Cochran, E. A.; Enman, L. J.; Mitchson, G.; Ditto, J.; Siefe, C.; Plassmeyer, P. N.; Greenaway, A. L.; Johnson, D. C.; Page, C. J.; Boettcher, S. W. Amorphous Mixed-Metal Oxide Thin Films from Aqueous Solution Precursors with Near-Atomic Smoothness. *J. Am. Chem. Soc.* **2016**, *138*, 16800–16808.

(35) Danks, A. E.; Hall, S. R.; Schnepp, Z. The Evolution of "Sol–Gel" Chemistry as a Technique for Materials Synthesis. *Mater. Horiz.* **2016**, *3*, 91–112.

(36) Brinker, C. J.; Scherer, G. W. *Sol-Gel Science: The Physics and Chemistry of Sol-Gel Processing*; Academic Press: San Diego, CA, USA, **1990**.

(37) Hench, L. L.; West, J. K. The Sol-Gel Process. *Chem. Rev.* **1990**, *90*, 33–72.

(38) Wen, J.; Wilkes, G. L. Organic/Inorganic Hybrid Network Materials by the Sol−Gel Approach. *Chem. Mater.* **1996**, *8*, 1667–1681.

(39) Fan, Q.; McQuillin, B.; Ray, A. K.; Turner, M. L.; Seddon, A. B. High Density, Non-Porous Anatase Titania Thin Films for Device Applications. *J. Phys. D. Appl. Phys.* **2000**, *33*, 2683–2686.

(40) Wang, Z.; Helmersson, U.; Käll, P.-O. Optical Properties of Anatase TiO_2 Thin Films Prepared by Aqueous Sol–Gel Process at Low Temperature. *Thin Solid Films* **2002**, *405*, 50–54.

(41) Ong, R. J.; Payne, D. A.; Sottos, N. R. Processing Effects for Integrated PZT: Residual Stress, Thickness, and Dielectric Properties. *J. Am. Ceram. Soc.* **2005**, *88*, 2839–2847.

(42) Kim, K. M.; Kim, C. W.; Heo, J. S.; Na, H.; Lee, J. E.; Park, C. B.; Bae, J.-U.; Kim, C.-D.; Jun, M.; Hwang, Y. K.; Meyers, S. T.; Grenville, A.; Keszler, D. A. Competitive Device Performance of Low-Temperature and All-Solution-Processed Metal-Oxide Thin-Film Transistors. *Appl. Phys. Lett.* **2011**, *99*, 242109.

(43) Jiang, K.; Anderson, J. T.; Hoshino, K.; Li, D.; Wager, J. F.; Keszler, D. A. Low-Energy Path to Dense HfO_2 Thin Films with Aqueous Precursor. *Chem. Mater.* **2011**, *23*, 945–952.

(44) Liu, A.; Liu, G. X.; Zhu, H. H.; Xu, F.; Fortunato, E.; Martins, R.; Shan, F. K. Fully Solution-Processed Low-Voltage Aqueous In_2O_3 Thin-Film Transistors Using an Ultrathin ZrO_x Dielectric. *ACS Appl. Mater. Interfaces* **2014**, *6*, 17364–17369.

(45) Rim, Y. S.; Chen, H.; Song, T.-B.; Bae, S.-H.; Yang, Y. Hexaaqua Metal Complexes for Low-Temperature Formation of Fully Metal Oxide Thin-Film Transistors. *Chem. Mater.* **2015**, *27*, 5808–5812.

(46) Liu, G.; Liu, A.; Zhu, H.; Shin, B.; Fortunato, E.; Martins, R.; Wang, Y.; Shan, F. Low-Temperature, Nontoxic Water-Induced Metal-Oxide Thin Films and Their Application in Thin-Film Transistors. *Adv. Funct. Mater.* **2015**, *25*, 2564–2572.

(47) Liu, A.; Liu, G.; Zhu, H.; Shin, B.; Fortunato, E.; Martins, R.; Shan, F. Eco-Friendly Water-Induced Aluminum Oxide Dielectrics and Their Applications in Hybrid Metal Oxide/Polymer TFT. *RSC Adv.* **2015**, *5*, 86606–86613.

(48) Liu, A.; Liu, G.; Zhu, H.; Song, H.; Shin, B.; Fortunato, E.; Martins, R.; Shan, F. Water-Induced Scandium Oxide Dielectric for Low-Operating Voltage n- and p-Type Metal-Oxide Thin-Film Transistors. *Adv. Funct. Mater.* **2015**, *25*, 7180–7188.

(49) Zhu, C.; Liu, A.; Liu, G.; Jiang, G.; Meng, Y.; Fortunato, E.; Martins, R.; Shan, F. Low-Temperature, Nontoxic Water-Induced High-κ Zirconium Oxide Dielectrics for Low-Voltage, High-Performance Oxide Thin-Film Transistors. *J. Mater. Chem. C* **2016**, *4*, 10715–10721.

(50) Xu, W.; Long, M.; Zhang, T.; Liang, L.; Cao, H.; Zhu, D.; Xu, J.-B. Fully Solution-Processed Metal Oxide Thin-Film Transistors via a Low-Temperature Aqueous Route. *Ceram. Int.* **2017**, *43*, 6130–6137.

(51) Richter, P.; Plassmeyer, P. N.; Harzdorf, J.; Rüffer, T.; Lang, H.; Kalbacova, J.; Jöhrmann, N.; Schulze, S.; Hietschold, M.; Arekapudi, S. S. P. K.; Albrecht, M.; Zahn, D. R. T.; Page, C. J.; Salvan, G. High Quality Magnetic Oxide Thin Films Prepared via Aqueous Solution Processing. *Chem. Mater.* **2016**, *28*, 4917–4927.

(52) Zhang, D.-S.; Ma, B.-Q.; Jin, T.-Z.; Gao, S.; Yan, C.-H.; Mak, T. C. W. Oxo-Centered Regular Octahedral Lanthanide Clusters. *New J. Chem.* **2000**, *24*, 61–62.

(53) Wang, R.; Carducci, M. D.; Zheng, Z. Direct Hydrolytic Route to Molecular Oxo−Hydroxo Lanthanide Clusters. *Inorg. Chem.* **2000**, *39*, 1836–1837.

(54) Nadarajah, A.; Carnes, M. E.; Kast, M. G.; Johnson, D. W.; Boettcher, S. W. Aqueous Solution Processing of F-Doped SnO_2 Transparent Conducting Oxide Films Using a Reactive Tin(II) Hydroxide Nitrate Nanoscale Cluster. *Chem. Mater.* **2013**, *25*, 4080–4087.

(55) Wang, W.; Liu, W.; Chang, I.-Y.; Wills, L. A.; Zakharov, L. N.; Boettcher, S. W.; Cheong, P. H.-Y.; Fang, C.; Keszler, D. A. Electrolytic Synthesis of Aqueous Aluminum Nanoclusters and In Situ Characterization by Femtosecond Raman Spectroscopy and Computations. *Proc. Natl. Acad. Sci.* **2013**, *110*, 18397–18401.

(56) Carnes, M. E.; Knutson, C. C.; Nadarajah, A.; Jackson Jr., M. N.; Oliveri, A. F.; Norelli, K. M.; Crockett, B. M.; Bauers, S. R.; Moreno-Luna, H. A.; Taber, B. N.; Pacheco, D. J.; Olson, J. Z.; Brevick, K. R.; Sheehan, C. E.; Johnson, D. W.; Boettcher, S. W. Electrochemical Synthesis of Flat-$[Ga_{13-x}In_x(\mu_3\text{-}OH)_6(\mu\text{-}OH)_{18}(H_2O)_{24}(NO_3)_{15}]$ Clusters as Aqueous Precursors for Solution-Processed Semiconductors. *J. Mater. Chem. C* **2014**, *2*, 8492–8496.

(57) Ruther, R. E.; Baker, B. M.; Son, J.-H.; Casey, W. H.; Nyman, M. Hafnium Sulfate Prenucleation Clusters and the Hf_{18} Polyoxometalate Red Herring. *Inorg. Chem.* **2014**, *53*, 4234–4242.

(58) Nadarajah, A.; Wu, M. Z. B.; Archila, K.; Kast, M. G.; Smith, A. M.; Chiang, T. H.; Keszler, D. A.; Wager, J. F.; Boettcher, S. W. Amorphous In–Ga–Zn Oxide Semiconducting Thin Films with High Mobility from Electrochemically Generated Aqueous Nanocluster Inks. *Chem. Mater.* **2015**, *27*, 5587–5596.

(59) Plassmeyer, P. N.; Archila, K.; Wager, J. F.; Page, C. J. Lanthanum Aluminum Oxide Thin-Film Dielectrics from Aqueous Solution. *ACS Appl. Mater. Interfaces* **2015**, *7*, 1678–1684.

(60) Kim, Y.-H.; Heo, J.-S.; Kim, T.-H.; Park, S.; Yoon, M.-H.; Kim, J.; Oh, M. S.; Yi, G.-R.; Noh, Y.-Y.; Park, S. K. Flexible Metal-Oxide Devices Made by Room-Temperature Photochemical Activation of Sol–Gel Films. *Nature* **2012**, *489*, 128–132.

(61) Han, S.-Y.; Herman, G. S.; Chang, C. Low-Temperature, High-Performance, Solution-Processed Indium Oxide Thin-Film Transistors. *J. Am. Chem. Soc.* **2011**, *133*, 5166–5169.

(62) Jun, T.; Song, K.; Jeong, Y.; Woo, K.; Kim, D.; Bae, C.; Moon, J. High-Performance Low-Temperature Solution-Processable ZnO Thin Film Transistors by Microwave-Assisted Annealing. *J. Mater. Chem.* **2011**, *21*, 1102–1108.

(63) Varma, A.; Mukasyan, A. S.; Rogachev, A. S.; Manukyan, K. V. Solution Combustion Synthesis of Nanoscale Materials. *Chem. Rev.* **2016**, *116*, 14493–14586.

(64) Kim, M.-G.; Kanatzidis, M. G.; Facchetti, A.; Marks, T. J. Low-Temperature Fabrication of High-Performance Metal Oxide Thin-Film Electronics via Combustion Processing. *Nat. Mater.* **2011**, *10*, 382–388.

(65) Manukyan, K. V.; Cross, A.; Roslyakov, S.; Rouvimov, S.; Rogachev, A. S.; Wolf, E. E.; Mukasyan, A. S. Solution Combustion Synthesis of Nano-Crystalline Metallic Materials: Mechanistic Studies. *J. Phys. Chem. C* **2013**, *117*, 24417–24427.

(66) Sanchez-Rodriguez, D.; Farjas, J.; Roura, P.; Ricart, S.; Mestres, N.; Obradors, X.; Puig, T. Thermal Analysis for Low Temperature Synthesis of Oxide Thin Films from Chemical Solutions. *J. Phys. Chem. C* **2013**, *117*, 20133–20138.

(67) Sánchez-Rodríguez, D.; Eloussifi, H.; Farjas, J.; Roura, P.; Dammak, M. Thermal Gradients in Thermal Analysis Experiments: Criterions to Prevent Inaccuracies When Determining Sample Temperature and Kinetic Parameters. *Thermochim. Acta* **2014**, *589*, 37–46.

(68) Roura, P.; Farjas, J.; Eloussifi, H.; Carreras, L.; Ricart, S.; Puig, T.; Obradors, X. Thermal Analysis of Metal Organic Precursors for Functional Oxide Preparation: Thin Films versus Powders. *Thermochim. Acta* **2015**, *601*, 1–8.

(69) Banger, K. K.; Yamashita, Y.; Mori, K.; Peterson, R. L.; Leedham, T.; Rickard, J.; Sirringhaus, H. Low-Temperature, High-Performance Solution-Processed Metal Oxide Thin-Film Transistors Formed by a "Sol–Gel on Chip" Process. *Nat. Mater.* **2011**, *10*, 45–50.

(70) Hwang, Y. H.; Jeon, J.-H.; Bae, B.-S. Post-Humid Annealing of Low-Temperature Solution-Processed Indium Based Metal Oxide TFTs. *Electrochem. Solid-State Lett.* **2011**, *14*, H303–H305.

(71) Park, W.-T.; Son, I.; Park, H.-W.; Chung, K.-B.; Xu, Y.; Lee, T.; Noh, Y.-Y. Facile Routes to Improve Performance of Solution-Processed Amorphous Metal Oxide Thin Film Transistors by Water Vapor Annealing. *ACS Appl. Mater. Interfaces* **2015**, *7*, 13289–13294.

(72) Zhao, Y.; Toyama, M.; Kita, K.; Kyuno, K.; Toriumi, A. Moisture-Absorption-Induced Permittivity Deterioration and Surface Roughness Enhancement of Lanthanum Oxide Films on Silicon. *Appl. Phys. Lett.* **2006**, *88*, 72904.

(73) Anderson, J. T.; Wang, W.; Jiang, K.; Gustafsson, T.; Xu, C.; Garfunkel, E. L.; Keszler, D. A. Chemically Amplified Dehydration of Thin Oxide Films. *ACS Sustain. Chem. Eng.* **2015**, *3*, 1081–1085.

(74) Perkins, C. K.; Mansergh, R. H.; Park, D.-H.; Nanayakkara, C. E.; Ramos, J. C.; Decker, S. R.; Huang, Y.; Chabal, Y. J.; Keszler, D. A. Aqueous Process to Limit Hydration of Thin-Film Inorganic Oxides. *Solid State Sci.* **2016**, *61*, 106–110.

(75) Cairncross, R. A.; Schunk, P. R.; Chen, K. S.; Prakash, S. S.; Samuel, J.; Hurd, A. J.; Brinker, C. J. Pore Evolution and Solvent Transport During Drying of Gelled Sol-Gel Coatings: Predicting "Springback." *Dry. Technol.* **1997**, *15*, 1815–1825.

(76) Teodorescu, V. S.; Blanchin, M.-G. In *Microscopy: Advances in Scientific Research and Education*; Méndez-Vilas, A., Ed.; FORMATEX: Badajoz, Spain, **2014**.

(77) Gutmann, E.; Meyer, D. C.; Levin, A. A.; Paufler, P. Density-Modulated Alumina-Based Nanometre Films Prepared by Sol-Gel Technique. *Appl. Phys. A Mater. Sci. Process.* **2005**, *81*, 249–259.

(78) Morelhão, S. L.; Brito, G. E. S.; Abramof, E. Nanostructure of Sol–Gel Films by X-Ray Specular Reflectivity. *Appl. Phys. Lett.* **2002**, *80*, 407–409.

(79) Loke, V. L. Y.; Riefler, N.; Mehner, A.; Prenzel, T.; Hoja, T.; Wriedt, T.; Mädler, L. Multilayer Model for Determining the Thickness and Refractive Index of Sol-Gel Coatings via Laser Ellipsometry. *Thin Solid Films* **2013**, *531*, 93–98.

Chapter II

(1) Sanchez-Rodriguez, D.; Farjas, J.; Roura, P.; Ricart, S.; Mestres, N.; Obradors, X.; Puig, T. Thermal Analysis for Low Temperature Synthesis of Oxide Thin Films from Chemical Solutions. *J. Phys. Chem. C* **2013**, *117*, 20133–20138.

(2) Sánchez-Rodríguez, D.; Eloussifi, H.; Farjas, J.; Roura, P.; Dammak, M. Thermal Gradients in Thermal Analysis Experiments: Criterions to Prevent Inaccuracies When Determining Sample Temperature and Kinetic Parameters. *Thermochim. Acta* **2014**, *589*, 37–46.

(3) Roura, P.; Farjas, J.; Eloussifi, H.; Carreras, L.; Ricart, S.; Puig, T.; Obradors, X. Thermal Analysis of Metal Organic Precursors for Functional Oxide Preparation: Thin Films versus Powders. *Thermochim. Acta* **2015**, *601*, 1–8.

(4) Wood, S. R.; Woods, K. N.; Plassmeyer, P. N.; Marsh, D. A.; Johnson, D. W.; Page, C. J.; Jensen, K. M. Ø.; Johnson, D. C. Same Precursor, Two Different Products: Comparing the Structural Evolution of In–Ga–O "Gel-Derived" Powders and Solution-Cast Films Using Pair Distribution Function Analysis. *J. Am. Chem. Soc.* **2017**, *139*, 5607–5613.

(5) Jiang, K.; Anderson, J. T.; Hoshino, K.; Li, D.; Wager, J. F.; Keszler, D. A. Low-Energy Path to Dense HfO_2 Thin Films with Aqueous Precursor. *Chem. Mater.* **2011**, *23*, 945–952.

(6) Jung, Y.; Kline, R. J.; Fischer, D. A.; Lin, E. K.; Heeney, M.; McCulloch, I.; DeLongchamp, D. M. The Effect of Interfacial Roughness on the Thin Film Morphology and Charge Transport of High-Performance Polythiophenes. *Adv. Funct. Mater.* **2008**, *18*, 742–750.

(7) Lee, J.-M.; Choi, B.-H.; Ji, M.-J.; Park, J.-H.; Kwon, J.-H.; Ju, B.-K. The Improved Performance of a Transparent ZnO Thin-Film Transistor with AlN/Al_2O_3 Double Gate Dielectrics. *Semicond. Sci. Technol.* **2009**, *24*, 55008.

(8) Alimardani, N.; Cowell III, E. W.; Wager, J. F.; Conley Jr., J. F.; Evans, D. R.; Chin, M.; Kilpatrick, S. J.; Dubey, M. Impact of Electrode Roughness on Metal-Insulator-Metal Tunnel Diodes with Atomic Layer Deposited Al_2O_3 Tunnel Barriers. *J. Vac. Sci. Technol., A* **2012**, *30*, 01A113.

(9) Kojima, I.; Li, B. Structural Characterization of Thin Films by X-Ray. *Rigaku J.* **1999**, *16*, 31–42.

(10) Phung, T. M.; Jensen, J. M.; Johnson, D. C.; Donovan, J. J.; McBurnett, B. G. Determination of the Composition of Ultra-Thin Ni-Si Films on Si: Constrained Modeling of Electron Probe Microanalysis and X-Ray Reflectivity Data. *X-Ray Spectrom.* **2008**, *37*, 608–614.

(11) Anderson, J. T.; Munsee, C. L.; Hung, C. M.; Phung, T. M.; Herman, G. S.; Johnson, D. C.; Wager, J. F.; Keszler, D. A. Solution-Processed HafSOx and ZircSO$_x$ Inorganic Thin-Film Dielectrics and Nanolaminates. *Adv. Funct. Mater.* **2007**, *17*, 2117–2124.

(12) Jiang, K.; Meyers, S. T.; Anderson, M. D.; Johnson, D. C.; Keszler, D. A. Functional Ultrathin Films and Nanolaminates from Aqueous Solutions. *Chem. Mater.* **2013**, *25*, 210–214.

(13) Wormington, M.; Panaccione, C.; Matney, K. M.; Bowen, D. K. Characterization of Structures from X-Ray Scattering Data Using Genetic Algorithms. *Philos. Trans. R. Soc., A* **1999**, *357*, 2827–2848.

(14) Giessibl, F. J. Advances in Atomic Force Microscopy. *Rev. Mod. Phys.* **2003**, *75*, 949–983.

(15) Zhao, Y.; Toyama, M.; Kita, K.; Kyuno, K.; Toriumi, A. Moisture-Absorption-Induced Permittivity Deterioration and Surface Roughness Enhancement of Lanthanum Oxide Films on Silicon. *Appl. Phys. Lett.* **2006**, *88*, 72904.

(16) Ko, J.; Kim, J.; Park, S. Y.; Lee, E.; Kim, K.; Lim, K.-H.; Kim, Y. S. Solution-Processed Amorphous Hafnium-Lanthanum Oxide Gate Insulator for Oxide Thin-Film Transistors. *J. Mater. Chem. C* **2014**, *2*, 1050–1056.

(17) Esro, M.; Mazzocco, R.; Vourlias, G.; Kolosov, O.; Krier, A.; Milne, W. I.; Adamopoulos, G. Solution Processed Lanthanum Aluminate Gate Dielectrics for Use in Metal Oxide-Based Thin Film Transistors. *Appl. Phys. Lett.* **2015**, *106*, 203507.

(18) Kast, M. G.; Cochran, E. A.; Enman, L. J.; Mitchson, G.; Ditto, J.; Siefe, C.; Plassmeyer, P. N.; Greenaway, A. L.; Johnson, D. C.; Page, C. J.; Boettcher, S. W. Amorphous Mixed-Metal Oxide Thin Films from Aqueous Solution Precursors with Near-Atomic Smoothness. *J. Am. Chem. Soc.* **2016**, *138*, 16800–16808.

(19) Jin, L.; Yu, Z.; Zhang, Y.; Wang, Y.; Yan, G.; Li, C.; Lu, Y. Effect of $La_2Zr_2O_7$-Buffered YSZ Substrate on $YBa_2Cu_3O_y$ Thin Films by Chemical Solution Deposition. *Phys. C* **2010**, *470*, 602–605.

(20) Nadarajah, A.; Carnes, M. E.; Kast, M. G.; Johnson, D. W.; Boettcher, S. W. Aqueous Solution Processing of F-Doped SnO_2 Transparent Conducting Oxide Films Using a Reactive Tin(II) Hydroxide Nitrate Nanoscale Cluster. *Chem. Mater.* **2013**, *25*, 4080–4087.

(21) Kast, M. G.; Enman, L. J.; Gurnon, N. J.; Nadarajah, A.; Boettcher, S. W. Solution-Deposited F:SnO_2/TiO_2 as a Base-Stable Protective Layer and Antireflective Coating for Microtextured Buried-Junction H_2-Evolving Si Photocathodes. *ACS Appl. Mater. Interfaces* **2014**, *6*, 22830–22837.

(22) Nadarajah, A.; Wu, M. Z. B.; Archila, K.; Kast, M. G.; Smith, A. M.; Chiang, T. H.; Keszler, D. A.; Wager, J. F.; Boettcher, S. W. Amorphous In–Ga–Zn Oxide Semiconducting Thin Films with High Mobility from Electrochemically Generated Aqueous Nanocluster Inks. *Chem. Mater.* **2015**, *27*, 5587–5596.

(23) Plassmeyer, P. N.; Archila, K.; Wager, J. F.; Page, C. J. Lanthanum Aluminum Oxide Thin-Film Dielectrics from Aqueous Solution. *ACS Appl. Mater. Interfaces* **2015**, *7*, 1678–1684.

(24) Greenaway, A. L.; Sharps, M. C.; Boucher, J. W.; Strange, L. E.; Kast, M. G.; Aloni, S.; Boettcher, S. W. Selective Area Epitaxy of GaAs Microstructures by Close-Spaced Vapor Transport for Solar Energy Conversion Applications. *ACS Energy Lett.* **2016**, *1*, 402–408.

(25) Kim, K. H.; Akase, Z.; Suzuki, T.; Shindo, D. Charging Effects on SEM/SIM Contrast of Metal/Insulator System in Various Metallic Coating Conditions. *Mater. Trans.* **2010**, *51*, 1080–1083.

(26) Joy, D. C.; Joy, C. S. Low Voltage Scanning Electron Microscopy. *Micron* **1996**, *27*, 247–263.

(27) Smith, S. W.; Wang, W.; Keszler, D. A.; Conley, J. F. Solution Based Prompt Inorganic Condensation and Atomic Layer Deposition of Al_2O_3 Films: A Side-by-Side Comparison. *J. Vac. Sci. Technol., A* **2014**, *32*, 41501.

(28) Anderson, J. T.; Wang, W.; Jiang, K.; Gustafsson, T.; Xu, C.; Garfunkel, E. L.; Keszler, D. A. Chemically Amplified Dehydration of Thin Oxide Films. *ACS Sustain. Chem. Eng.* **2015**, *3*, 1081–1085.

(29) Perkins, C. K.; Mansergh, R. H.; Park, D.-H.; Nanayakkara, C. E.; Ramos, J. C.; Decker, S. R.; Huang, Y.; Chabal, Y. J.; Keszler, D. A. Aqueous Process to Limit Hydration of Thin-Film Inorganic Oxides. *Solid State Sci.* **2016**, *61*, 106–110.

(30) Giannuzzi, L. A.; Stevie, F. A. A Review of Focused Ion Beam Milling Techniques for TEM Specimen Preparation. *Micron* **1999**, *30*, 197–204.

(31) Giannuzzi, L. A.; Kempshall, B. W.; Schwarz, S. M.; Lomness, J. K.; Prenitzer, B. I.; Stevie, F. A. In *Introduction to Focused Ion Beams*; Giannuzzi, L. A.; Stevie, F. A., Eds.; Springer: Boston, MA, **2005**; pp. 201–228.

(32) Wang, Z. L. New Developments in Transmission Electron Microscopy for Nanotechnology. *Adv. Mater.* **2003**, *15*, 1497–1514.

(33) Lin, Y.; McCarthy, J. A.; Poeppelmeier, K. R.; Marks, L. D. In *Catalysis by Materials with Well-Defined Structures*; Wu, Z.; Overbury, S. H., Eds.; Elsevier: Amsterdam, Netherlands, **2015**; pp. 193–238.

(34) Inada, H.; Su, D.; Egerton, R. F.; Konno, M.; Wu, L.; Ciston, J.; Wall, J.; Zhu, Y. Atomic Imaging Using Secondary Electrons in a Scanning Transmission Electron Microscope: Experimental Observations and Possible Mechanisms. *Ultramicroscopy* **2011**, *111*, 865–876.

(35) Egerton, R. F.; Li, P.; Malac, M. Radiation Damage in the TEM and SEM. *Micron* **2004**, *35*, 399–409.

(36) McCaffrey, J. P.; Phaneuf, M. W.; Madsen, L. D. Surface Damage Formation During Ion-Beam Thinning of Samples for Transmission Electron Microscopy. *Ultramicroscopy* **2001**, *87*, 97–104.

(37) Chi, Y.; Chuang, S. S. C. Infrared and TPD Studies of Nitrates Adsorbed on Tb_4O_7, La_2O_3, BaO, and MgO/γ-Al_2O_3. *J. Phys. Chem. B* **2000**, *104*, 4673–4683.

(38) Prinetto, F.; Ghiotti, G.; Nova, I.; Lietti, L.; Tronconi, E.; Forzatti, P. FT-IR and TPD Investigation of the NO_x Storage Properties of BaO/Al_2O_3 and Pt−BaO/Al_2O_3 Catalysts. *J. Phys. Chem. B* **2001**, *105*, 12732–12745.

(39) Al-Abadleh, H. A.; Grassian, V. H. FT-IR Study of Water Adsorption on Aluminum Oxide Surfaces. *Langmuir* **2003**, *19*, 341–347.

(40) Meyers, S. T.; Anderson, J. T.; Hong, D.; Hung, C. M.; Wager, J. F.; Keszler, D. A. Solution-Processed Aluminum Oxide Phosphate Thin-Film Dielectrics. *Chem. Mater.* **2007**, *19*, 4023–4029.

(41) Chen, H. S.; Kumar, R. V.; Glowacki, B. A. Chemical Solution Deposited Lanthanum Zirconium Oxide Thin Films: Synthesis and Chemistry. *Mater. Chem. Phys.* **2010**, *122*, 305–310.

(42) Zhang, X.; He, H.; Gao, H.; Yu, Y. Experimental and Theoretical Studies of Surface Nitrate Species on Ag/Al_2O_3 Using DRIFTS and DFT. *Spectrochim. Acta, Part A* **2008**, *71*, 1446–1451.

(43) Egashira, M.; Nakashima, M.; Kawasumi, S.; Selyama, T. Temperature Programmed Desorption Study of Water Adsorbed on Metal Oxides. 2. Tin Oxide Surfaces. *J. Phys. Chem.* **1981**, *85*, 4125–4130.

(44) Mansergh, R. H.; Fullmer, L. B.; Park, D. H.; Nyman, M.; Keszler, D. A. Reaction Pathway: Aqueous Hexatantalate Clusters to High-Density Tantalum Oxide Nanofilms. *Chem. Mater.* **2016**, *28*, 1553–1558.

(45) Moulder, J. F.; Stickle, W. F.; Sobol, P. E.; Bomben, K. D. *Handbook of X-Ray Photoelectron Spectroscopy: A Reference Book of Standard Spectra for Identification and Interpretation of XPS Data*; Chastain, J., Ed.; Perkin-Elmer: Eden Prairie, MN, **1992**.

(46) Howng, W.-Y.; Thorn, R. J. Investigation of the Electronic Structure of $La_{1-x}(M^{2+})_xCrO_3$, Cr_2O_3 and La_2O_3 by X-Ray Photoelectron Spectroscopy. *J. Phys. Chem. Solids* **1980**, *41*, 75–81.

(47) Majumdar, D.; Chatterjee, D. X-Ray Photoelectron Spectroscopic Studies on Yttria, Zirconia, and Yttria-Stabilized Zirconia. *J. Appl. Phys.* **1991**, *70*, 988–992.

(48) Biesinger, M. C.; Lau, L. W. M.; Gerson, A. R.; Smart, R. S. C. Resolving Surface Chemical States in XPS Analysis of First Row Transition Metals, Oxides and Hydroxides: Sc, Ti, V, Cu and Zn. *Appl. Surf. Sci.* **2010**, *257*, 887–898.

(49) Goncharova, L. V.; Dalponte, M.; Feng, T.; Gustafsson, T.; Garfunkel, E.; Lysaght, P. S.; Bersuker, G. Diffusion and Interface Growth in Hafnium Oxide and Silicate Ultrathin Films on Si(001). *Phys. Rev. B* **2011**, *83*, 115329.

(50) Fenter, P.; Gustafsson, T. Structural Analysis of the Pt(110)-(1×2) Surface Using Medium-Energy Ion Scattering. *Phys. Rev. B* **1988**, *38*, 10197–10204.

(51) Mitchson, G.; Ditto, J.; Woods, K. N.; Westover, R.; Page, C. J.; Johnson, D. C. Application of HAADF STEM Image Analysis to Structure Determination in Rotationally Disordered and Amorphous Multilayered Films. *Semicond. Sci. Technol.* **2016**, *31*, 84003.

(52) Parish, C. M.; Brewer, L. N. Multivariate Statistics Applications in Phase Analysis of STEM-EDS Spectrum Images. *Ultramicroscopy* **2010**, *110*, 134–143.

(53) Donovan, J. J.; Tingle, T. N. An Improved Mean Atomic Number Background Correction for Quantitative Microanalysis. *Microsc. Microanal.* **1996**, *2*, 1–7.

(54) Street, R. A. Thin-Film Transistors. *Adv. Mater.* **2009**, *21*, 2007–2022.

(55) Park, J. S.; Maeng, W.-J.; Kim, H.-S.; Park, J.-S. Review of Recent Developments in Amorphous Oxide Semiconductor Thin-Film Transistor Devices. *Thin Solid Films* **2012**, *520*, 1679–1693.

(56) Fortunato, E.; Barquinha, P.; Martins, R. Oxide Semiconductor Thin-Film Transistors: A Review of Recent Advances. *Adv. Mater.* **2012**, *24*, 2945–2986.

(57) Kuo, Y. Thin Film Transistor Technology—Past, Present, and Future. *Electrochem. Soc. Interface* **2013**, *22*, 55–61.

(58) Robertson, J.; Wallace, R. M. High-κ Materials and Metal Gates for CMOS Applications. *Mater. Sci. Eng. R* **2015**, *88*, 1–41.

(59) Wilk, G. D.; Wallace, R. M.; Anthony, J. M. High-K Gate Dielectrics: Current Status and Materials Properties Considerations. *J. Appl. Phys.* **2001**, *89*, 5243–5275.

(60) Robertson, J. High Dielectric Constant Gate Oxides for Metal Oxide Si Transistors. *Rep. Prog. Phys.* **2006**, *69*, 327–396.

(61) Norelli, K. M.; Plassmeyer, P. N.; Woods, K. N.; Glassy, B. A.; Knutson, C. C.; Beekman, M.; Page, C. J. Influence of Composition and Processing Parameters on the Properties of Solution-Processed Aluminum Phosphate Oxide (AlPO) Thin Films. *Solid State Sci.* **2016**, *55*, 8–12.

(62) Aoki, Y.; Kunitake, T. Solution-Based Fabrication of High-κ Gate Dielectrics for Next-Generation Metal-Oxide Semiconductor Transistors. *Adv. Mater.* **2004**, *16*, 118–123.

(63) Lichtenwalner, D. J.; Jur, J. S.; Kingon, A. I.; Agustin, M. P.; Yang, Y.; Stemmer, S.; Goncharova, L. V.; Gustafsson, T.; Garfunkel, E. Lanthanum Silicate Gate Dielectric Stacks with Subnanometer Equivalent Oxide Thickness Utilizing an Interfacial Silica Consumption Reaction. *J. Appl. Phys.* **2005**, *98*, 24314.

Chapter III

(1) Robertson, J. High Dielectric Constant Gate Oxides for Metal Oxide Si Transistors. *Rep. Prog. Phys.* **2006**, *69*, 327–396.

(2) Fortunato, E.; Barquinha, P.; Martins, R. Oxide Semiconductor Thin-Film Transistors: A Review of Recent Advances. *Adv. Mater.* **2012**, *24*, 2945–2986.

(3) Wilk, G. D.; Wallace, R. M.; Anthony, J. M. High-κ Gate Dielectrics: Current Status and Materials Properties Considerations. *J. Appl. Phys.* **2001**, *89*, 5243–5275.

(4) Maria, J. P.; Wicaksana, D.; Kingon, A. I.; Busch, B.; Schulte, H.; Garfunkel, E.; Gustafsson, T. High Temperature Stability in Lanthanum and Zirconia-Based Gate Dielectrics. *J. Appl. Phys.* **2001**, *90*, 3476–3482.

(5) Kukli, K.; Forsgren, K.; Ritala, M.; Leskelä, M.; Aarik, J.; Hårsta, A. Dielectric Properties of Zirconium Oxide Grown by Atomic Layer Deposition from Iodide Precursor. *J. Electrochem. Soc.* **2001**, *148*, F227–F232.

(6) Adamopoulos, G.; Thomas, S.; Wöbkenberg, P. H.; Bradley, D. D. C.; McLachlan, M. A.; Anthopoulos, T. D. High-Mobility Low-Voltage ZnO and Li-Doped ZnO Transistors Based on ZrO_2 High-κ Dielectric Grown by Spray Pyrolysis in Ambient Air. *Adv. Mater.* **2011**, *23*, 1894–1898.

(7) Xifeng, L.; Enlong, X.; Jianhua, Z. Low-Temperature Solution-Processed Zirconium Oxide Gate Insulators for Thin-Film Transistors. *IEEE Trans. Electron Devices* **2013**, *60*, 3413–3416.

(8) Park, J. H.; Yoo, Y. B.; Lee, K. H.; Jang, W. S.; Oh, J. Y.; Chae, S. S.; Baik, H. K. Low-Temperature, High-Performance Solution-Processed Thin-Film Transistors with Peroxo-Zirconium Oxide Dielectric. *ACS Appl. Mater. Interfaces* **2013**, *5*, 410–417.

(9) Park, Y. M.; Desai, A.; Salleo, A.; Jimison, L. Solution-Processable Zirconium Oxide Gate Dielectrics for Flexible Organic Field Effect Transistors Operated at Low Voltages. *Chem. Mater.* **2013**, *25*, 2571–2579.

(10) Jang, J.; Kitsomboonloha, R.; Swisher, S. L.; Park, E. S.; Kang, H.; Subramanian, V. Transparent High-Performance Thin Film Transistors from Solution-Processed SnO_2/ZrO_2 Gel-like Precursors. *Adv. Mater.* **2013**, *25*, 1042–1047.

(11) Liu, A.; Liu, G. X.; Zhu, H. H.; Xu, F.; Fortunato, E.; Martins, R.; Shan, F. K. Fully Solution-Processed Low-Voltage Aqueous In_2O_3 Thin-Film Transistors Using an Ultrathin ZrOx Dielectric. *ACS Appl. Mater. Interfaces* **2014**, *6*, 17364–17369.

(12) Yamada, H.; Shimizu, T.; Kurokawa, A.; Ishii, K.; Suzuki, E. MOCVD of High-Dielectric-Constant Lanthanum Oxide Thin Films. *J. Electrochem. Soc.* **2003**, *150*, G429–G435.

(13) He, W.; Schuetz, S.; Solanki, R.; Belot, J.; McAndrew, J. Atomic Layer Deposition of Lanthanum Oxide Films for High-κ Gate Dielectrics. *Electrochem. Solid-State Lett.* **2004**, *7*, G131–G133.

(14) Kukli, K.; Ritala, M.; Pore, V.; Leskelä, M.; Sajavaara, T.; Hegde, R. I.; Gilmer, D. C.; Tobin, P. J.; Jones, A. C.; Aspinall, H. C. Atomic Layer Deposition and Properties of Lanthanum Oxide and Lanthanum-Aluminum Oxide Films. *Chem. Vap. Depos.* **2006**, *12*, 158–164.

(15) Zhuang, J.; Sun, Q.-J.; Zhou, Y.; Han, S.-T.; Zhou, L.; Yan, Y.; Peng, H.; Venkatesh, S.; Wu, W.; Li, R. K. Y.; Roy, V. A. L. Solution-Processed Rare-Earth Oxide Thin Films for Alternative Gate Dielectric Application. *ACS Appl. Mater. Interfaces* **2016**, *8*, 31128–31135.

(16) Kingon, A. I.; Maria, J.-P.; Streiffer, S. K. Alternative Dielectrics to Silicon Dioxide for Memory and Logic Devices. *Nature* **2000**, *406*, 1032–1038.

(17) De Asha, A. M.; Critchley, J. T. S.; Nix, R. M. Molecular Adsorption Characteristics of Lanthanum Oxide Surfaces: The Interaction of Water with Oxide Overlayers Grown on Cu(111). *Surf. Sci.* **1998**, *405*, 201–214.

(18) Nieminen, M.; Putkonen, M.; Niinistö, L. Formation and Stability of Lanthanum Oxide Thin Films Deposited from β-Diketonate Precursor. *Appl. Surf. Sci.* **2001**, *174*, 155–165.

(19) Gougousi, T.; Niu, D.; Ashcraft, R. W.; Parsons, G. N. Carbonate Formation During Post-Deposition Ambient Exposure of High-κ Dielectrics. *Appl. Phys. Lett.* **2003**, *83*, 3543–3545.

(20) Zhao, Y.; Toyama, M.; Kita, K.; Kyuno, K.; Toriumi, A. Moisture-Absorption-Induced Permittivity Deterioration and Surface Roughness Enhancement of Lanthanum Oxide Films on Silicon. *Appl. Phys. Lett.* **2006**, *88*, 72904.

(21) Wang, C.; Fabrichnaya, O.; Zinkevich, M.; Du, Y.; Aldinger, F. Experimental Study and Thermodynamic Modelling of the ZrO_2–$LaO_{1.5}$ System. *Calphad* **2008**, *32*, 111–120.

(22) Chirayil, T. G.; Paranthaman, M.; Beach, D. B.; Lee, D. F.; Goyal, A.; Williams, R. K.; Cui, X.; Kroeger, D. M.; Feenstra, R.; Verebelyi, D. T.; Christen, D. K. Epitaxial Growth of $La_2Zr_2O_7$ Thin Films on Rolled Ni-Substrates by Sol–gel Process for High Tc Superconducting Tapes. *Phys. C* **2000**, *336*, 63–69.

(23) Sathyamurthy, S.; Paranthaman, M.; Aytug, T.; Kang, B. W.; Martin, P. M.; Goyal, A.; Kroeger, D. M.; Christen, D. K. Chemical Solution Deposition of Lanthanum Zirconate Buffer Layers on Biaxially Textured Ni–1.7% Fe–3% W Alloy Substrates for Coated-Conductor Fabrication. *J. Mater. Res.* **2002**, *17*, 1543–1549.

(24) Sathyamurthy, S.; Paranthaman, M.; Zhai, H.-Y.; Christen, H. M.; Martin, P. M.; Goyal, A. Lanthanum Zirconate: A Single Buffer Layer Processed by Solution Deposition for Coated Conductor Fabrication. *J. Mater. Res.* **2002**, *17*, 2181–2184.

(25) Knoth, K.; Schlobach, B.; Hühne, R.; Schultz, L.; Holzapfel, B. La2Zr2O7 and Ce–Gd–O Buffer Layers for YBCO Coated Conductors Using Chemical Solution Deposition. *Phys. C* **2005**, *426–431*, 979–984.

(26) Sathyamurthy, S.; Paranthaman, M.; Heatherly, L.; Martin, P. M.; Specht, E. D.; Goyal, A.; Kodenkandath, T.; Li, X.; Rupich, M. W. Solution-Processed Lanthanum Zirconium Oxide as a Barrier Layer for High I_c-Coated Conductors. *J. Mater. Res.* **2006**, *21*, 910–914.

(27) Jin, L.; Yu, Z.; Zhang, Y.; Wang, Y.; Yan, G.; Li, C.; Lu, Y. Effect of $La_2Zr_2O_7$-Buffered YSZ Substrate on $YBa_2Cu_3O_y$ Thin Films by Chemical Solution Deposition. *Phys. C* **2010**, *470*, 602–605.

(28) Chen, H. S.; Kumar, R. V.; Glowacki, B. A. Chemical Solution Deposited Lanthanum Zirconium Oxide Thin Films: Synthesis and Chemistry. *Mater. Chem. Phys.* **2010**, *122*, 305–310.

(29) Molina-Luna, L.; Egoavil, R.; Turner, S.; Thersleff, T.; Verbeeck, J.; Holzapfel, B.; Eibl, O.; Van Tendeloo, G. Interlayer Structure in YBCO-Coated Conductors Prepared by Chemical Solution Deposition. *Supercond. Sci. Technol.* **2013**, *26*, 75016.

(30) Gaskell, J. M.; Jones, A. C.; Aspinall, H. C.; Taylor, S.; Taechakumput, P.; Chalker, P. R.; Heys, P. N.; Odedra, R. Deposition of Lanthanum Zirconium Oxide High-κ Films by Liquid Injection Atomic Layer Deposition. *Appl. Phys. Lett.* **2007**, *91*, 112912.

(31) Gaskell, J. M.; Jones, A. C.; Chalker, P. R.; Werner, M.; Aspinall, H. C.; Taylor, S.; Taechakumput, P.; Heys, P. N. Deposition of Lanthanum Zirconium Oxide High-K Films by Liquid Injection ALD and MOCVD. *Chem. Vap. Depos.* **2007**, *13*, 684–690.

(32) Alessandri, M.; Del Vitto, A.; Piagge, R.; Sebastiani, A.; Scozzari, C.; Wiemer, C.; Lamagna, L.; Perego, M.; Ghidini, G.; Fanciulli, M. Rare Earth-Based High-κ Materials for Non-Volatile Memory Applications. *Microelectron. Eng.* **2010**, *87*, 290–293.

(33) Tue, P. T.; Li, J.; Miyasako, T.; Inoue, S.; Shimoda, T. Low-Temperature All-Solution-Derived Amorphous Oxide Thin-Film Transistors. *IEEE Electron Device Lett.* **2013**, *34*, 1536–1538.

(34) Tue, P. T.; Miyasako, T.; Li, J.; Tu, H. T. C.; Inoue, S.; Tokumitsu, E.; Shimoda, T. High-Performance Solution-Processed ZrInZnO Thin-Film Transistors. *IEEE Trans. Electron Devices* **2013**, *60*, 320–326.

(35) Je, S. Y.; Son, B.-G.; Kim, H.-G.; Park, M.-Y.; Do, L.-M.; Choi, R.; Jeong, J. K. Solution-Processable $LaZrO_x/SiO_2$ Gate Dielectric at Low Temperature of 180 °C for High-Performance Metal Oxide Field-Effect Transistors. *ACS Appl. Mater. Interfaces* **2014**, *6*, 18693–18703.

(36) Li, J.; Zhu, P.; Hirose, D.; Kohara, S.; Shimoda, T. Hybrid Cluster Precursors of the LaZrO Insulator for Transistors: Properties of High-Temperature-Processed Films and Structures of Solutions, Gels, and Solids. *Sci. Rep.* **2016**, *6*, 29682.

(37) Niinistö, L.; Päiväsaari, J.; Niinistö, J.; Putkonen, M.; Nieminen, M. Advanced Electronic and Optoelectronic Materials by Atomic Layer Deposition: An Overview with Special Emphasis on Recent Progress in Processing of High-κ Dielectrics and Other Oxide Materials. *Phys. Status Solidi A* **2004**, *201*, 1443–1452.

(38) Jones, A. C.; Aspinall, H. C.; Chalker, P. R.; Potter, R. J.; Kukli, K.; Rahtu, A.; Ritala, M.; Leskela, M. Some Recent Developments in the MOCVD and ALD of High-κ Dielectric Oxides. *J. Mater. Chem.* **2004**, *14*, 3101–3112.

(39) Jones, A. C.; Chalker, P. R. Some Recent Developments in the Chemical Vapour Deposition of Electroceramic Oxides. *J. Phys. D. Appl. Phys.* **2003**, *36*, R80–R95.

(40) Christen, H. M.; Eres, G. Recent Advances in Pulsed-Laser Deposition of Complex Oxides. *J. Phys. Condens. Matter* **2008**, *20*, 264005.

(41) Ong, B. S.; Li, C.; Li, Y.; Wu, Y.; Loutfy, R. Stable, Solution-Processed, High-Mobility ZnO Thin-Film Transistors. *J. Am. Chem. Soc.* **2007**, *129*, 2750–2751.

(42) Jeong, Y.; Kim, D.; Song, K.; Jun, T.; Woo, K.; Moon, J. Solution-Processed Stable Zinc Oxide Semiconductor for Thin-Film Transistors. *J. Phys. Chem. C* **2008**, *112*, 11082–11085.

(43) Pal, B. N.; Trottman, P.; Sun, J.; Katz, H. E. Solution-Deposited Zinc Oxide and Zinc Oxide/Pentacene Bilayer Transistors: High Mobility N-Channel, Ambipolar, and Nonvolatile Devices. *Adv. Funct. Mater.* **2008**, *18*, 1832–1839.

(44) Meyers, S. T.; Anderson, J. T.; Hung, C. M.; Thompson, J.; Wager, J. F.; Keszler, D. A. Aqueous Inorganic Inks for Low-Temperature Fabrication of ZnO TFTs. *J. Am. Chem. Soc.* **2008**, *130*, 17603–17609.

(45) Adamopoulos, G.; Bashir, A.; Gillin, W. P.; Georgakopoulos, S.; Shkunov, M.; Baklar, M. A.; Stingelin, N.; Bradley, D. D. C.; Anthopoulos, T. D. Structural and Electrical Characterization of ZnO Films Grown by Spray Pyrolysis and Their Application in Thin-Film Transistors. *Adv. Funct. Mater.* **2011**, *21*, 525–531.

(46) Thomas, S. R.; Pattanasattayavong, P.; Anthopoulos, T. D. Solution-Processable Metal Oxide Semiconductors for Thin-Film Transistor Applications. *Chem. Soc. Rev.* **2013**, *42*, 6910–6923.

(47) Jiang, K.; Meyers, S. T.; Anderson, M. D.; Johnson, D. C.; Keszler, D. A. Functional Ultrathin Films and Nanolaminates from Aqueous Solutions. *Chem. Mater.* **2013**, *25*, 210–214.

(48) Xu, W.; Wang, H.; Ye, L.; Xu, J. The Role of Solution-Processed High-κ Gate Dielectrics in Electrical Performance of Oxide Thin-Film Transistors. *J. Mater. Chem. C* **2014**, *2*, 5389–5396.

(49) Esro, M.; Vourlias, G.; Somerton, C.; Milne, W. I.; Adamopoulos, G. High-Mobility ZnO Thin Film Transistors Based on Solution-Processed Hafnium Oxide Gate Dielectrics. *Adv. Funct. Mater.* **2015**, *25*, 134–141.

(50) Xu, W.; Cao, H.; Liang, L.; Xu, J.-B. Aqueous Solution-Deposited Gallium Oxide Dielectric for Low-Temperature, Low-Operating-Voltage Indium Oxide Thin-Film Transistors: A Facile Route to Green Oxide Electronics. *ACS Appl. Mater. Interfaces* **2015**, *7*, 14720–14725.

(51) Liu, G.; Liu, A.; Zhu, H.; Shin, B.; Fortunato, E.; Martins, R.; Wang, Y.; Shan, F. Low-Temperature, Nontoxic Water-Induced Metal-Oxide Thin Films and Their Application in Thin-Film Transistors. *Adv. Funct. Mater.* **2015**, *25*, 2564–2572.

(52) Nadarajah, A.; Wu, M. Z. B.; Archila, K.; Kast, M. G.; Smith, A. M.; Chiang, T. H.; Keszler, D. A.; Wager, J. F.; Boettcher, S. W. Amorphous In–Ga–Zn Oxide Semiconducting Thin Films with High Mobility from Electrochemically Generated Aqueous Nanocluster Inks. *Chem. Mater.* **2015**, *27*, 5587–5596.

(53) Esro, M.; Mazzocco, R.; Vourlias, G.; Kolosov, O.; Krier, A.; Milne, W. I.; Adamopoulos, G. Solution Processed Lanthanum Aluminate Gate Dielectrics for Use in Metal Oxide-Based Thin Film Transistors. *Appl. Phys. Lett.* **2015**, *106*, 203507.

(54) Xu, W.; Wang, H.; Xie, F.; Chen, J.; Cao, H.; Xu, J.-B. Facile and Environmentally Friendly Solution-Processed Aluminum Oxide Dielectric for Low-Temperature, High-Performance Oxide Thin-Film Transistors. *ACS Appl. Mater. Interfaces* **2015**, *7*, 5803–5810.

(55) Liu, A.; Liu, G.; Zhu, H.; Song, H.; Shin, B.; Fortunato, E.; Martins, R.; Shan, F. Water-Induced Scandium Oxide Dielectric for Low-Operating Voltage n- and p-Type Metal-Oxide Thin-Film Transistors. *Adv. Funct. Mater.* **2015**, *25*, 7180–7188.

(56) Park, S.; Kim, C.-H.; Lee, W.-J.; Sung, S.; Yoon, M.-H. Sol-Gel Metal Oxide Dielectrics for All-Solution-Processed Electronics. *Mater. Sci. Eng., R* **2017**, *114*, 1–22.

(57) Brinker, C. J.; Scherer, G. W. *Sol-Gel Science: The Physics and Chemistry of Sol-Gel Processing*; Academic Press: San Diego, CA, USA, **1990**.

(58) Fan, Q.; McQuillin, B.; Ray, A. K.; Turner, M. L.; Seddon, A. B. High Density, Non-Porous Anatase Titania Thin Films for Device Applications. *J. Phys. D. Appl. Phys.* **2000**, *33*, 2683–2686.

(59) Wang, Z.; Helmersson, U.; Käll, P.-O. Optical Properties of Anatase TiO_2 Thin Films Prepared by Aqueous Sol–Gel Process at Low Temperature. *Thin Solid Films* **2002**, *405*, 50–54.

(60) Anderson, J. T.; Munsee, C. L.; Hung, C. M.; Phung, T. M.; Herman, G. S.; Johnson, D. C.; Wager, J. F.; Keszler, D. A. Solution-Processed HafSOx and ZircSOx Inorganic Thin-Film Dielectrics and Nanolaminates. *Adv. Funct. Mater.* **2007**, *17*, 2117–2124.

(61) Meyers, S. T.; Anderson, J. T.; Hong, D.; Hung, C. M.; Wager, J. F.; Keszler, D. A. Solution-Processed Aluminum Oxide Phosphate Thin-Film Dielectrics. *Chem. Mater.* **2007**, *19*, 4023–4029.

(62) Jiang, K.; Anderson, J. T.; Hoshino, K.; Li, D.; Wager, J. F.; Keszler, D. A. Low-Energy Path to Dense HfO_2 Thin Films with Aqueous Precursor. *Chem. Mater.* **2011**, *23*, 945–952.

(63) Alemayehu, M.; Davis, J. E.; Jackson, M.; Lessig, B.; Smith, L.; Sumega, J. D.; Knutson, C.; Beekman, M.; Johnson, D. C.; Keszler, D. A. Tunable Dielectric Thin Films by Aqueous, Inorganic Solution-Based Processing. *Solid State Sci.* **2011**, *13*, 2037–2040.

(64) Plassmeyer, P. N.; Archila, K.; Wager, J. F.; Page, C. J. Lanthanum Aluminum Oxide Thin-Film Dielectrics from Aqueous Solution. *ACS Appl. Mater. Interfaces* **2015**, *7*, 1678–1684.

(65) Norelli, K. M.; Plassmeyer, P. N.; Woods, K. N.; Glassy, B. A.; Knutson, C. C.; Beekman, M.; Page, C. J. Influence of Composition and Processing Parameters on the Properties of Solution-Processed Aluminum Phosphate Oxide (AlPO) Thin Films. *Solid State Sci.* **2016**, *55*, 8–12.

(66) Kim, K. M.; Kim, C. W.; Heo, J. S.; Na, H.; Lee, J. E.; Park, C. B.; Bae, J.-U.; Kim, C.-D.; Jun, M.; Hwang, Y. K.; Meyers, S. T.; Grenville, A.; Keszler, D. A. Competitive Device Performance of Low-Temperature and All-Solution-Processed Metal-Oxide Thin-Film Transistors. *Appl. Phys. Lett.* **2011**, *99*, 242109.

(67) Smith, S. W.; Wang, W.; Keszler, D. A.; Conley, J. F. Solution Based Prompt Inorganic Condensation and Atomic Layer Deposition of Al_2O_3 Films: A Side-by-Side Comparison. *J. Vac. Sci. Technol., A* **2014**, *32*, 41501.

(68) Wormington, M.; Panaccione, C.; Matney, K. M.; Bowen, D. K. Characterization of Structures from X-Ray Scattering Data Using Genetic Algorithms. *Philos. Trans. R. Soc., A* **1999**, *357*, 2827–2848.

(69) Kim, K. H.; Akase, Z.; Suzuki, T.; Shindo, D. Charging Effects on SEM/SIM Contrast of Metal/Insulator System in Various Metallic Coating Conditions. *Mater. Trans.* **2010**, *51*, 1080–1083.

(70) Al-Abadleh, H. A.; Grassian, V. H. FT-IR Study of Water Adsorption on Aluminum Oxide Surfaces. *Langmuir* **2003**, *19*, 341–347.

(71) Nyquist, R. A.; Putzig, C. L.; Leugers, M. A.; Kagel, R. O. *The Handbook of Infrared and Raman Spectra of Inorganic Compounds and Organic Salts*; Academic Press: San Diego, CA, USA, **1997**.

(72) Klingenberg, B.; Vannice, M. A. Influence of Pretreatment on Lanthanum Nitrate, Carbonate, and Oxide Powders. *Chem. Mater.* **1996**, *8*, 2755–2768.

(73) Martinet, C.; Devine, R. A. B. Analysis of the Vibrational Mode Spectra of Amorphous SiO_2 Films. *J. Appl. Phys.* **1995**, *77*, 4343–4348.

(74) Devine, R. A. B. Structural Nature of the Si/SiO_2 Interface Through Infrared Spectroscopy. *Appl. Phys. Lett.* **1996**, *68*, 3108–3110.

(75) Uno, M.; Kosuga, A.; Okui, M.; Horisaka, K.; Muta, H.; Kurosaki, K.; Yamanaka, S. Photoelectrochemical Study of Lanthanide Zirconium Oxides, $Ln_2Zr_2O_7$ (Ln = La, Ce, Nd and Sm). *J. Alloys Compd.* **2006**, *420*, 291–297.

(76) Fairley, K. C.; Merrill, D. R.; Woods, K. N.; Ditto, J.; Xu, C.; Oleksak, R. P.; Gustafsson, T.; Johnson, D. W.; Garfunkel, E. L.; Herman, G. S.; Johnson, D. C.; Page, C. J. Non-Uniform Composition Profiles in Inorganic Thin Films from Aqueous Solutions. *ACS Appl. Mater. Interfaces* **2016**, *8*, 667–672.

(77) Yugeswaran, S.; Selvarajan, V.; Ananthapadmanabhan, P. V.; Lusvarghi, L. Twin Step Synthesis of Lanthanum Zirconate through Transferred Arc Plasma Processing. *J. Phys. Conf. Ser.* **2010**, *208*, 12119.

(78) Kojima, I.; Li, B. Structural Characterization of Thin Films by X-Ray. *Rigaku J.* **1999**, *16*, 31–42.

(79) Jung, Y.; Kline, R. J.; Fischer, D. A.; Lin, E. K.; Heeney, M.; McCulloch, I.; DeLongchamp, D. M. The Effect of Interfacial Roughness on the Thin Film Morphology and Charge Transport of High-Performance Polythiophenes. *Adv. Funct. Mater.* **2008**, *18*, 742–750.

(80) Lee, J.-M.; Choi, B.-H.; Ji, M.-J.; Park, J.-H.; Kwon, J.-H.; Ju, B.-K. The Improved Performance of a Transparent ZnO Thin-Film Transistor with AlN/Al_2O_3 Double Gate Dielectrics. *Semicond. Sci. Technol.* **2009**, *24*, 55008.

(81) Alimardani, N.; Cowell III, E. W.; Wager, J. F.; Conley Jr., J. F.; Evans, D. R.; Chin, M.; Kilpatrick, S. J.; Dubey, M. Impact of Electrode Roughness on Metal-Insulator-Metal Tunnel Diodes with Atomic Layer Deposited Al_2O_3 Tunnel Barriers. *J. Vac. Sci. Technol., A* **2012**, *30*, 01A113.

Chapter IV

(1) Robertson, J. High Dielectric Constant Gate Oxides for Metal Oxide Si Transistors. *Rep. Prog. Phys.* **2006**, *69*, 327–396.

(2) Fortunato, E.; Barquinha, P.; Martins, R. Oxide Semiconductor Thin-Film Transistors: A Review of Recent Advances. *Adv. Mater.* **2012**, *24*, 2945–2986.

(3) Wilk, G. D.; Wallace, R. M.; Anthony, J. M. High-κ Gate Dielectrics: Current Status and Materials Properties Considerations. *J. Appl. Phys.* **2001**, *89*, 5243–5275.

(4) Maria, J. P.; Wicaksana, D.; Kingon, A. I.; Busch, B.; Schulte, H.; Garfunkel, E.; Gustafsson, T. High Temperature Stability in Lanthanum and Zirconia-Based Gate Dielectrics. *J. Appl. Phys.* **2001**, *90*, 3476–3482.

(5) Kukli, K.; Forsgren, K.; Ritala, M.; Leskelä, M.; Aarik, J.; Hårsta, A. Dielectric Properties of Zirconium Oxide Grown by Atomic Layer Deposition from Iodide Precursor. *J. Electrochem. Soc.* **2001**, *148*, F227–F232.

(6) Adamopoulos, G.; Thomas, S.; Wöbkenberg, P. H.; Bradley, D. D. C.; McLachlan, M. A.; Anthopoulos, T. D. High-Mobility Low-Voltage ZnO and Li-Doped ZnO Transistors Based on ZrO_2 High-κ Dielectric Grown by Spray Pyrolysis in Ambient Air. *Adv. Mater.* **2011**, *23*, 1894–1898.

(7) Xifeng, L.; Enlong, X.; Jianhua, Z. Low-Temperature Solution-Processed Zirconium Oxide Gate Insulators for Thin-Film Transistors. *IEEE Trans. Electron Devices* **2013**, *60*, 3413–3416.

(8) Park, J. H.; Yoo, Y. B.; Lee, K. H.; Jang, W. S.; Oh, J. Y.; Chae, S. S.; Baik, H. K. Low-Temperature, High-Performance Solution-Processed Thin-Film Transistors with Peroxo-Zirconium Oxide Dielectric. *ACS Appl. Mater. Interfaces* **2013**, *5*, 410–417.

(9) Park, Y. M.; Desai, A.; Salleo, A.; Jimison, L. Solution-Processable Zirconium Oxide Gate Dielectrics for Flexible Organic Field Effect Transistors Operated at Low Voltages. *Chem. Mater.* **2013**, *25*, 2571–2579.

(10) Jang, J.; Kitsomboonloha, R.; Swisher, S. L.; Park, E. S.; Kang, H.; Subramanian, V. Transparent High-Performance Thin Film Transistors from Solution-Processed SnO_2/ZrO_2 Gel-like Precursors. *Adv. Mater.* **2013**, *25*, 1042–1047.

(11) Liu, A.; Liu, G. X.; Zhu, H. H.; Xu, F.; Fortunato, E.; Martins, R.; Shan, F. K. Fully Solution-Processed Low-Voltage Aqueous In_2O_3 Thin-Film Transistors Using an Ultrathin ZrO_x Dielectric. *ACS Appl. Mater. Interfaces* **2014**, *6*, 17364–17369.

(12) Liu, G. X.; Liu, A.; Shan, F. K.; Meng, Y.; Shin, B. C.; Fortunato, E.; Martins, R. High-Performance Fully Amorphous Bilayer Metal-Oxide Thin Film Transistors Using Ultra-Thin Solution-Processed ZrO_x Dielectric. *Appl. Phys. Lett.* **2014**, *105*, 113509.

(13) Zhu, C.; Liu, A.; Liu, G.; Jiang, G.; Meng, Y.; Fortunato, E.; Martins, R.; Shan, F. Low-Temperature, Nontoxic Water-Induced High-κ Zirconium Oxide Dielectrics for Low-Voltage, High-Performance Oxide Thin-Film Transistors. *J. Mater. Chem. C* **2016**, *4*, 10715–10721.

(14) He, W.; Xu, W.; Peng, Q.; Liu, C.; Zhou, G.; Wu, S.; Zeng, M.; Zhang, Z.; Gao, J.; Gao, X.; Lu, X.; Liu, J.-M. Surface Modification on Solution Processable ZrO_2 High-κ Dielectrics for Low Voltage Operations of Organic Thin Film Transistors. *J. Phys. Chem. C* **2016**, *120*, 9949–9957.

(15) Avis, C.; Jang, J. High-Performance Solution Processed Oxide TFT with Aluminum Oxide Gate Dielectric Fabricated by a Sol–Gel Method. *J. Mater. Chem.* **2011**, *21*, 10649–10652.

(16) Lim, T.; Kim, D.; Ju, S. Direct Deposition of Aluminum Oxide Gate Dielectric on Graphene Channel Using Nitrogen Plasma Treatment. *Appl. Phys. Lett.* **2013**, *103*, 13107.

(17) Liu, Y.; Guan, P.; Zhang, B.; Falk, M. L.; Katz, H. E. Ion Dependence of Gate Dielectric Behavior of Alkali Metal Ion-Incorporated Aluminas in Oxide Field-Effect Transistors. *Chem. Mater.* **2013**, *25*, 3788–3796.

(18) Park, J. H.; Kim, K.; Yoo, Y. B.; Park, S. Y.; Lim, K.-H.; Lee, K. H.; Baik, H. K.; Kim, Y. S. Water Adsorption Effects of Nitrate Ion Coordinated Al_2O_3 Dielectric for High Performance Metal-Oxide Thin-Film Transistor. *J. Mater. Chem. C* **2013**, *1*, 7166–7174.

(19) Nayak, P. K.; Hedhili, M. N.; Cha, D.; Alshareef, H. N. High Performance In_2O_3 Thin Film Transistors Using Chemically Derived Aluminum Oxide Dielectric. *Appl. Phys. Lett.* **2013**, *103*, 33518.

(20) Ha, H. J.; Jeong, S. W.; Oh, T.-Y.; Kim, M.; Choi, K.; Park, J. H.; Ju, B.-K. Flexible Low-Voltage Pentacene Memory Thin-Film Transistors with Combustion-Processable Al_2O_3 Gate Dielectric and Au Nanoparticles. *J. Phys. D. Appl. Phys.* **2013**, *46*, 235102.

(21) Bae, E. J.; Kang, Y. H.; Han, M.; Lee, C.; Cho, S. Y. Soluble Oxide Gate Dielectrics Prepared Using the Self-Combustion Reaction for High-Performance Thin-Film Transistors. *J. Mater. Chem. C* **2014**, *2*, 5695–5703.

(22) Liang, L. Y.; Cao, H. T.; Liu, Q.; Jiang, K. M.; Liu, Z. M.; Zhuge, F.; Deng, F. L. Substrate Biasing Effect on the Physical Properties of Reactive RF-Magnetron-Sputtered Aluminum Oxide Dielectric Films on ITO Glasses. *ACS Appl. Mater. Interfaces* **2014**, *6*, 2255–2261.

(23) Huang, G.; Duan, L.; Dong, G.; Zhang, D.; Qiu, Y. High-Mobility Solution-Processed Tin Oxide Thin-Film Transistors with High-κ Alumina Dielectric Working in Enhancement Mode. *ACS Appl. Mater. Interfaces* **2014**, *6*, 20786–20794.

(24) Wang, H.; Sun, T.; Xu, W.; Xie, F.; Ye, L.; Xiao, Y.; Wang, Y.; Chen, J.; Xu, J. Low-Temperature Facile Solution-Processed Gate Dielectric for Combustion Derived Oxide Thin Film Transistors. *RSC Adv.* **2014**, *4*, 54729–54739.

(25) Rim, Y. S.; Chen, H.; Liu, Y.; Bae, S.-H.; Kim, H. J.; Yang, Y. Direct Light Pattern Integration of Low-Temperature Solution-Processed All-Oxide Flexible Electronics. *ACS Nano* **2014**, *8*, 9680–9686.

(26) Branquinho, R.; Salgueiro, D.; Santos, L.; Barquinha, P.; Pereira, L.; Martins, R.; Fortunato, E. Aqueous Combustion Synthesis of Aluminum Oxide Thin Films and Application as Gate Dielectric in GZTO Solution-Based TFTs. *ACS Appl. Mater. Interfaces* **2014**, *6*, 19592–19599.

(27) Park, H.; Nam, Y.; Jin, J.; Bae, B.-S. Space Charge-Induced Unusually-High Mobility of a Solution-Processed Indium Oxide Thin Film Transistor with an Ethylene Glycol Incorporated Aluminum Oxide Gate Dielectric. *RSC Adv.* **2015**, *5*, 102362–102366.

(28) Branquinho, R.; Salgueiro, D.; Santa, A.; Kiazadeh, A.; Barquinha, P.; Pereira, L.; Martins, R.; Fortunato, E. Towards Environmental Friendly Solution-Based ZTO/AlOx TFTs. *Semicond. Sci. Technol.* **2015**, *30*, 24007.

(29) Tan, H.; Liu, G.; Liu, A.; Shin, B.; Shan, F. The Annealing Effects on the Properties of Solution-Processed Alumina Thin Film and Its Application in TFTs. *Ceram. Int.* **2015**, *41*, S349–S355.

(30) Liu, A.; Liu, G.; Zhu, H.; Shin, B.; Fortunato, E.; Martins, R.; Shan, F. Eco-Friendly Water-Induced Aluminum Oxide Dielectrics and Their Applications in Hybrid Metal Oxide/Polymer TFT. *RSC Adv.* **2015**, *5*, 86606–86613.

(31) Xu, W.; Wang, H.; Xie, F.; Chen, J.; Cao, H.; Xu, J.-B. Facile and Environmentally Friendly Solution-Processed Aluminum Oxide Dielectric for Low-Temperature, High-Performance Oxide Thin-Film Transistors. *ACS Appl. Mater. Interfaces* **2015**, *7*, 5803–5810.

(32) Rim, Y. S.; Chen, H.; Song, T.-B.; Bae, S.-H.; Yang, Y. Hexaaqua Metal Complexes for Low-Temperature Formation of Fully Metal Oxide Thin-Film Transistors. *Chem. Mater.* **2015**, *27*, 5808–5812.

(33) Xu, W.; Long, M.; Zhang, T.; Liang, L.; Cao, H.; Zhu, D.; Xu, J.-B. Fully Solution-Processed Metal Oxide Thin-Film Transistors via a Low-Temperature Aqueous Route. *Ceram. Int.* **2017**, *43*, 6130–6137.

(34) Jiang, K.; Anderson, J. T.; Hoshino, K.; Li, D.; Wager, J. F.; Keszler, D. A. Low-Energy Path to Dense HfO_2 Thin Films with Aqueous Precursor. *Chem. Mater.* **2011**, *23*, 945–952.

(35) Zhu, J.; Liu, Z. G. Structure and Dielectric Properties of Zr–Al–O Thin Films Prepared by Pulsed Laser Deposition. *Microelectron. Eng.* **2003**, *66*, 849–854.

(36) Li, Y.; Zhu, J.; Liu, H.; Liu, Z. Fabrication and Characterization of Zr-Rich Zr-Aluminate Films for High-κ Gate Dielectric Applications. *Microelectron. Eng.* **2006**, *83*, 1905–1911.

(37) Zhou, D.; Schroeder, U.; Jegert, G.; Kerber, M.; Uppal, S.; Agaiby, R.; Reinicke, M.; Heitmann, J.; Oberbeck, L. Time Dependent Dielectric Breakdown of Amorphous $ZrAl_xO_y$ High-κ Dielectric Used in Dynamic Random Access Memory Metal-Insulator-Metal Capacitor. *J. Appl. Phys.* **2009**, *106*, 44104.

(38) Zhou, D.; Schroeder, U.; Xu, J.; Heitmann, J.; Jegert, G.; Weinreich, W.; Kerber, M.; Knebel, S.; Erben, E.; Mikolajick, T. Reliability of Al_2O_3-Doped ZrO_2 High-κ Dielectrics in Three-Dimensional Stacked Metal-Insulator-Metal Capacitors. *J. Appl. Phys.* **2010**, *108*, 124104.

(39) Bizarro, M.; Alonso, J. C.; Ortiz, A. The Effect of the Process Conditions on the Synthesis of Zirconium-Aluminum Oxide Thin Films Prepared by Ultrasonic Spray Pyrolysis. *J. Electrochem. Soc.* **2005**, *152*, F179–F184.

(40) Bizarro, M.; Alonso, J. C.; Ortiz, A. ZrAlO Ternary Oxide as a Candidate for High-κ Dielectrics. *Mater. Sci. Semicond. Process.* **2006**, *9*, 1090–1096.

(41) Vitanov, P.; Harizanova, A.; Ivanova, T.; Trapalis, C.; Todorova, N. Sol–Gel ZrO_2 and ZrO_2–Al_2O_3 Nanocrystalline Thin Films on Si as High-κ Dielectrics. *Mater. Sci. Eng., B* **2009**, *165*, 178–181.

(42) Yang, W.; Song, K.; Jung, Y.; Jeong, S.; Moon, J. Solution-Deposited Zr-Doped AlO_x Gate Dielectrics Enabling High-Performance Flexible Transparent Thin Film Transistors. *J. Mater. Chem. C* **2013**, *1*, 4275–4282.

(43) Thomas, S. R.; Pattanasattayavong, P.; Anthopoulos, T. D. Solution-Processable Metal Oxide Semiconductors for Thin-Film Transistor Applications. *Chem. Soc. Rev.* **2013**, *42*, 6910–6923.

(44) Park, S.; Kim, C.-H.; Lee, W.-J.; Sung, S.; Yoon, M.-H. Sol-Gel Metal Oxide Dielectrics for All-Solution-Processed Electronics. *Mater. Sci. Eng., R* **2017**, *114*, 1–22.

(45) Fan, Q.; McQuillin, B.; Ray, A. K.; Turner, M. L.; Seddon, A. B. High Density, Non-Porous Anatase Titania Thin Films for Device Applications. *J. Phys. D. Appl. Phys.* **2000**, *33*, 2683–2686.

(46) Wang, Z.; Helmersson, U.; Käll, P.-O. Optical Properties of Anatase TiO_2 Thin Films Prepared by Aqueous Sol–Gel Process at Low Temperature. *Thin Solid Films* **2002**, *405*, 50–54.

(47) Anderson, J. T.; Munsee, C. L.; Hung, C. M.; Phung, T. M.; Herman, G. S.; Johnson, D. C.; Wager, J. F.; Keszler, D. A. Solution-Processed HafSOx and ZircSOx Inorganic Thin-Film Dielectrics and Nanolaminates. *Adv. Funct. Mater.* **2007**, *17*, 2117–2124.

(48) Meyers, S. T.; Anderson, J. T.; Hong, D.; Hung, C. M.; Wager, J. F.; Keszler, D. A. Solution-Processed Aluminum Oxide Phosphate Thin-Film Dielectrics. *Chem. Mater.* **2007**, *19*, 4023–4029.

(49) Alemayehu, M.; Davis, J. E.; Jackson, M.; Lessig, B.; Smith, L.; Sumega, J. D.; Knutson, C.; Beekman, M.; Johnson, D. C.; Keszler, D. A. Tunable Dielectric Thin Films by Aqueous, Inorganic Solution-Based Processing. *Solid State Sci.* **2011**, *13*, 2037–2040.

(50) Jiang, K.; Meyers, S. T.; Anderson, M. D.; Johnson, D. C.; Keszler, D. A. Functional Ultrathin Films and Nanolaminates from Aqueous Solutions. *Chem. Mater.* **2013**, *25*, 210–214.

(51) Oleksak, R. P.; Stickle, W. F.; Herman, G. S. Aqueous-Based Synthesis of Gallium Tungsten Oxide Thin Film Dielectrics. *J. Mater. Chem. C* **2015**, *3*, 3114–3120.

(52) Nadarajah, A.; Wu, M. Z. B.; Archila, K.; Kast, M. G.; Smith, A. M.; Chiang, T. H.; Keszler, D. A.; Wager, J. F.; Boettcher, S. W. Amorphous In–Ga–Zn Oxide Semiconducting Thin Films with High Mobility from Electrochemically Generated Aqueous Nanocluster Inks. *Chem. Mater.* **2015**, *27*, 5587–5596.

(53) Plassmeyer, P. N.; Archila, K.; Wager, J. F.; Page, C. J. Lanthanum Aluminum Oxide Thin-Film Dielectrics from Aqueous Solution. *ACS Appl. Mater. Interfaces* **2015**, *7*, 1678–1684.

(54) Norelli, K. M.; Plassmeyer, P. N.; Woods, K. N.; Glassy, B. A.; Knutson, C. C.; Beekman, M.; Page, C. J. Influence of Composition and Processing Parameters on the Properties of Solution-Processed Aluminum Phosphate Oxide (AlPO) Thin Films. *Solid State Sci.* **2016**, *55*, 8–12.

(55) Woods, K. N.; Chiang, T.-H.; Plassmeyer, P. N.; Kast, M. G.; Lygo, A. C.; Grealish, A. K.; Boettcher, S. W.; Page, C. J. High-κ Lanthanum Zirconium Oxide Thin Film Dielectrics from Aqueous Solution Precursors. *ACS Appl. Mater. Interfaces* **2017**, *9*, 10897–10903.

(56) Kim, K. M.; Kim, C. W.; Heo, J. S.; Na, H.; Lee, J. E.; Park, C. B.; Bae, J.-U.; Kim, C.-D.; Jun, M.; Hwang, Y. K.; Meyers, S. T.; Grenville, A.; Keszler, D. A. Competitive Device Performance of Low-Temperature and All-Solution-Processed Metal-Oxide Thin-Film Transistors. *Appl. Phys. Lett.* **2011**, *99*, 242109.

(57) Smith, S. W.; Wang, W.; Keszler, D. A.; Conley, J. F. Solution Based Prompt Inorganic Condensation and Atomic Layer Deposition of Al_2O_3 Films: A Side-by-Side Comparison. *J. Vac. Sci. Technol., A* **2014**, *32*, 41501.

(58) Kast, M. G.; Cochran, E. A.; Enman, L. J.; Mitchson, G.; Ditto, J.; Siefe, C.; Plassmeyer, P. N.; Greenaway, A. L.; Johnson, D. C.; Page, C. J.; Boettcher, S. W. Amorphous Mixed-Metal Oxide Thin Films from Aqueous Solution Precursors with Near-Atomic Smoothness. *J. Am. Chem. Soc.* **2016**, *138*, 16800–16808.

(59) Wormington, M.; Panaccione, C.; Matney, K. M.; Bowen, D. K. Characterization of Structures from X-Ray Scattering Data Using Genetic Algorithms. *Philos. Trans. R. Soc., A* **1999**, *357*, 2827–2848.

(60) Kim, K. H.; Akase, Z.; Suzuki, T.; Shindo, D. Charging Effects on SEM/SIM Contrast of Metal/Insulator System in Various Metallic Coating Conditions. *Mater. Trans.* **2010**, *51*, 1080–1083.

(61) Yuvaraj, S.; Fan-Yuan, L.; Tsong-Huei, C.; Chuin-Tih, Y. Thermal Decomposition of Metal Nitrates in Air and Hydrogen Environments. *J. Phys. Chem. B* **2003**, *107*, 1044–1047.

(62) Roura, P.; Farjas, J.; Eloussifi, H.; Carreras, L.; Ricart, S.; Puig, T.; Obradors, X. Thermal Analysis of Metal Organic Precursors for Functional Oxide Preparation: Thin Films versus Powders. *Thermochim. Acta* **2015**, *601*, 1–8.

(63) Wood, S. R.; Woods, K. N.; Plassmeyer, P. N.; Marsh, D. A.; Johnson, D. W.; Page, C. J.; Jensen, K. M. Ø.; Johnson, D. C. Same Precursor, Two Different Products: Comparing the Structural Evolution of In–Ga–O "Gel-Derived" Powders and Solution-Cast Films Using Pair Distribution Function Analysis. *J. Am. Chem. Soc.* **2017**, *139*, 5607–5613.

(64) Al-Abadleh, H. A.; Grassian, V. H. FT-IR Study of Water Adsorption on Aluminum Oxide Surfaces. *Langmuir* **2003**, *19*, 341–347.

(65) Nyquist, R. A.; Putzig, C. L.; Leugers, M. A.; Kagel, R. O. *The Handbook of Infrared and Raman Spectra of Inorganic Compounds and Organic Salts*; Academic Press: San Diego, CA, USA, **1997**.

(66) Bondars, B.; Heidemane, G.; Grabis, J.; Laschke, K.; Boysen, H.; Schneider, J.; Frey, F. Powder Diffraction Investigations of Plasma Sprayed Zirconia. *J. Mater. Sci.* **1995**, *30*, 1621–1625.

(67) Jung, Y.; Kline, R. J.; Fischer, D. A.; Lin, E. K.; Heeney, M.; McCulloch, I.; DeLongchamp, D. M. The Effect of Interfacial Roughness on the Thin Film Morphology and Charge Transport of High-Performance Polythiophenes. *Adv. Funct. Mater.* **2008**, *18*, 742–750.

(68) Lee, J.-M.; Choi, B.-H.; Ji, M.-J.; Park, J.-H.; Kwon, J.-H.; Ju, B.-K. The Improved Performance of a Transparent ZnO Thin-Film Transistor with AlN/Al_2O_3 Double Gate Dielectrics. *Semicond. Sci. Technol.* **2009**, *24*, 55008.

(69) Alimardani, N.; Cowell III, E. W.; Wager, J. F.; Conley Jr., J. F.; Evans, D. R.; Chin, M.; Kilpatrick, S. J.; Dubey, M. Impact of Electrode Roughness on Metal-Insulator-Metal Tunnel Diodes with Atomic Layer Deposited Al_2O_3 Tunnel Barriers. *J. Vac. Sci. Technol., A* **2012**, *30*, 01A113.

Chapter V

(1) Takata, R.; Neumann, A.; Weber, D.; Pham, D.-V.; Anselmann, R.; Kitamura, Y.; Kakimura, T.; Suzuki, S.; Minami, S.; Kodama, M. Scalability and Homogeneity of Slot Die-Coated Metal Oxide Semiconductor for TFTs. *J. Soc. Inf. Disp.* **2016**, *24*, 381–385.

(2) Kast, M. G.; Cochran, E. A.; Enman, L. J.; Mitchson, G.; Ditto, J.; Siefe, C.; Plassmeyer, P. N.; Greenaway, A. L.; Johnson, D. C.; Page, C. J.; Boettcher, S. W. Amorphous Mixed-Metal Oxide Thin Films from Aqueous Solution Precursors with Near-Atomic Smoothness. *J. Am. Chem. Soc.* **2016**, *138*, 16800–16808.

(3) Thomas, S. R.; Pattanasattayavong, P.; Anthopoulos, T. D. Solution-Processable Metal Oxide Semiconductors for Thin-Film Transistor Applications. *Chem. Soc. Rev.* **2013**, *42*, 6910–6923.

(4) Kim, H. S.; Kim, M.-G.; Ha, Y.-G.; Kanatzidis, M. G.; Marks, T. J.; Facchetti, A. Low-Temperature Solution-Processed Amorphous Indium Tin Oxide Field-Effect Transistors. *J. Am. Chem. Soc.* **2009**, *131*, 10826–10827.

(5) Banger, K. K.; Yamashita, Y.; Mori, K.; Peterson, R. L.; Leedham, T.; Rickard, J.; Sirringhaus, H. Low-Temperature, High-Performance Solution-Processed Metal Oxide Thin-Film Transistors Formed by a "Sol–Gel on Chip" Process. *Nat. Mater.* **2011**, *10*, 45–50.

(6) Park, S.; Kim, C.-H.; Lee, W.-J.; Sung, S.; Yoon, M.-H. Sol-Gel Metal Oxide Dielectrics for All-Solution-Processed Electronics. *Mater. Sci. Eng., R* **2017**, *114*, 1–22.

(7) Jeong, S.; Moon, J. Low-Temperature, Solution-Processed Metal Oxide Thin Film Transistors. *J. Mater. Chem.* **2012**, *22*, 1243–1250.

(8) Aoki, Y.; Kunitake, T.; Nakao, A. Sol−Gel Fabrication of Dielectric HfO_2 Nano-Films; Formation of Uniform, Void-Free Layers and Their Superior Electrical Properties. *Chem. Mater.* **2005**, *17*, 450–458.

(9) Kim, B. S.; Taek Jeong, Y.; Lee, D.; Choi, T.; Jung, S. H.; Whan Choi, J.; Yang, C.; Jo, K.; Lee, B. J.; Park, E.; Na Kim, D.; Kim, Y.; Shin, S. Solution-Processed Zinc-Indium-Tin Oxide Thin-Film Transistors for Flat-Panel Displays. *Appl. Phys. Lett.* **2013**, *103*, 72110.

(10) Kim, H. S.; Byrne, P. D.; Facchetti, A.; Marks, T. J. High Performance Solution-Processed Indium Oxide Thin-Film Transistors. *J. Am. Chem. Soc.* **2008**, *130*, 12580–12581.

(11) Ong, B. S.; Li, C.; Li, Y.; Wu, Y.; Loutfy, R. Stable, Solution-Processed, High-Mobility ZnO Thin-Film Transistors. *J. Am. Chem. Soc.* **2007**, *129*, 2750–2751.

(12) Pal, B. N.; Dhar, B. M.; See, K. C.; Katz, H. E. Solution-Deposited Sodium Beta-Alumina Gate Dielectrics for Low-Voltage and Transparent Field-Effect Transistors. *Nat. Mater.* **2009**, *8*, 898–903.

(13) Zhu, L.; Gao, Y.; Li, X.; Sun, X. W.; Zhang, J. Development of High-κ Hafnium–Aluminum Oxide Dielectric Films Using Sol–gel Process. *J. Mater. Res.* **2014**, *29*, 1620–1625.

(14) Schwartz, R. W.; Schneller, T.; Waser, R. Chemical Solution Deposition of Electronic Oxide Films. *C. R. Chim.* **2004**, *7*, 433–461.

(15) Zhuang, J.; Sun, Q.-J.; Zhou, Y.; Han, S.-T.; Zhou, L.; Yan, Y.; Peng, H.; Venkatesh, S.; Wu, W.; Li, R. K. Y.; Roy, V. A. L. Solution-Processed Rare-Earth Oxide Thin Films for Alternative Gate Dielectric Application. *ACS Appl. Mater. Interfaces* **2016**, *8*, 31128–31135.

(16) Brinker, C. J.; Scherer, G. W. *Sol-Gel Science: The Physics and Chemistry of Sol-Gel Processing*; Academic Press: San Diego, CA, USA, **1990**.

(17) Lin, Y.-H.; Faber, H.; Zhao, K.; Wang, Q.; Amassian, A.; McLachlan, M.; Anthopoulos, T. D. High-Performance ZnO Transistors Processed Via an Aqueous Carbon-Free Metal Oxide Precursor Route at Temperatures Between 80-180 °C. *Adv. Mater.* **2013**, *25*, 4340–4346.

(18) Chang, J.; Chang, K. L.; Chi, C.; Zhang, J.; Wu, J. Water Induced Zinc Oxide Thin Film Formation and Its Transistor Performance. *J. Mater. Chem. C* **2014**, *2*, 5397–5403.

(19) Hwang, Y. H.; Seo, J.-S.; Yun, J. M.; Park, H.; Yang, S.; Park, S.-H. K.; Bae, B.-S. An "Aqueous Route" for the Fabrication of Low-Temperature-Processable Oxide Flexible Transparent Thin-Film Transistors on Plastic Substrates. *NPG Asia Mater.* **2013**, *5*, e45.

(20) Liu, A.; Liu, G. X.; Zhu, H. H.; Xu, F.; Fortunato, E.; Martins, R.; Shan, F. K. Fully Solution-Processed Low-Voltage Aqueous In_2O_3 Thin-Film Transistors Using an Ultrathin ZrO_x Dielectric. *ACS Appl. Mater. Interfaces* **2014**, *6*, 17364–17369.

(21) Liu, A.; Liu, G.; Zhu, H.; Meng, Y.; Song, H.; Shin, B.; Fortunato, E.; Martins, R.; Shan, F. A Water-Induced High-κ Yttrium Oxide Dielectric for Fully-Solution-Processed Oxide Thin-Film Transistors. *Curr. Appl. Phys.* **2015**, *15*, S75–S81.

(22) Liu, A.; Liu, G.; Zhu, H.; Shin, B.; Fortunato, E.; Martins, R.; Shan, F. Eco-Friendly Water-Induced Aluminum Oxide Dielectrics and Their Applications in Hybrid Metal Oxide/Polymer TFT. *RSC Adv.* **2015**, *5*, 86606–86613.

(23) Liu, A.; Liu, G.; Zhu, H.; Song, H.; Shin, B.; Fortunato, E.; Martins, R.; Shan, F. Water-Induced Scandium Oxide Dielectric for Low-Operating Voltage n- and p-Type Metal-Oxide Thin-Film Transistors. *Adv. Funct. Mater.* **2015**, *25*, 7180–7188.

(24) Liu, G.; Liu, A.; Zhu, H.; Shin, B.; Fortunato, E.; Martins, R.; Wang, Y.; Shan, F. Low-Temperature, Nontoxic Water-Induced Metal-Oxide Thin Films and Their Application in Thin-Film Transistors. *Adv. Funct. Mater.* **2015**, *25*, 2564–2572.

(25) Rim, Y. S.; Chen, H.; Song, T.-B.; Bae, S.-H.; Yang, Y. Hexaaqua Metal Complexes for Low-Temperature Formation of Fully Metal Oxide Thin-Film Transistors. *Chem. Mater.* **2015**, *27*, 5808–5812.

(26) Xu, W.; Cao, H.; Liang, L.; Xu, J.-B. Aqueous Solution-Deposited Gallium Oxide Dielectric for Low-Temperature, Low-Operating-Voltage Indium Oxide Thin-Film Transistors: A Facile Route to Green Oxide Electronics. *ACS Appl. Mater. Interfaces* **2015**, *7*, 14720–14725.

(27) Anderson, J. T.; Munsee, C. L.; Hung, C. M.; Phung, T. M.; Herman, G. S.; Johnson, D. C.; Wager, J. F.; Keszler, D. A. Solution-Processed HafSOx and ZircSOx Inorganic Thin-Film Dielectrics and Nanolaminates. *Adv. Funct. Mater.* **2007**, *17*, 2117–2124.

(28) Meyers, S. T.; Anderson, J. T.; Hong, D.; Hung, C. M.; Wager, J. F.; Keszler, D. A. Solution-Processed Aluminum Oxide Phosphate Thin-Film Dielectrics. *Chem. Mater.* **2007**, *19*, 4023–4029.

(29) Jiang, K.; Anderson, J. T.; Hoshino, K.; Li, D.; Wager, J. F.; Keszler, D. A. Low-Energy Path to Dense HfO_2 Thin Films with Aqueous Precursor. *Chem. Mater.* **2011**, *23*, 945–952.

(30) Alemayehu, M.; Davis, J. E.; Jackson, M.; Lessig, B.; Smith, L.; Sumega, J. D.; Knutson, C.; Beekman, M.; Johnson, D. C.; Keszler, D. A. Tunable Dielectric Thin Films by Aqueous, Inorganic Solution-Based Processing. *Solid State Sci.* **2011**, *13*, 2037–2040.

(31) Carnes, M. E.; Knutson, C. C.; Nadarajah, A.; Jackson Jr., M. N.; Oliveri, A. F.; Norelli, K. M.; Crockett, B. M.; Bauers, S. R.; Moreno-Luna, H. A.; Taber, B. N.; Pacheco, D. J.; Olson, J. Z.; Brevick, K. R.; Sheehan, C. E.; Johnson, D. W.; Boettcher, S. W. Electrochemical Synthesis of Flat-$[Ga_{13-x}In_x(\mu_3\text{-}OH)_6(\mu\text{-}OH)_{18}(H_2O)_{24}(NO_3)_{15}]$ Clusters as Aqueous Precursors for Solution-Processed Semiconductors. *J. Mater. Chem. C* **2014**, *2*, 8492–8496.

(32) Plassmeyer, P. N.; Archila, K.; Wager, J. F.; Page, C. J. Lanthanum Aluminum Oxide Thin-Film Dielectrics from Aqueous Solution. *ACS Appl. Mater. Interfaces* **2015**, *7*, 1678–1684.

(33) Nadarajah, A.; Wu, M. Z. B.; Archila, K.; Kast, M. G.; Smith, A. M.; Chiang, T. H.; Keszler, D. A.; Wager, J. F.; Boettcher, S. W. Amorphous In–Ga–Zn Oxide Semiconducting Thin Films with High Mobility from Electrochemically Generated Aqueous Nanocluster Inks. *Chem. Mater.* **2015**, *27*, 5587–5596.

(34) Mansergh, R. H.; Fullmer, L. B.; Park, D. H.; Nyman, M.; Keszler, D. A. Reaction Pathway: Aqueous Hexatantalate Clusters to High-Density Tantalum Oxide Nanofilms. *Chem. Mater.* **2016**, *28*, 1553–1558.

(35) Fullmer, L. B.; Mansergh, R. H.; Zakharov, L. N.; Keszler, D. A.; Nyman, M. Nb_2O_5 and Ta_2O_5 Thin Films from Polyoxometalate Precursors: A Single Proton Makes a Difference. *Cryst. Growth Des.* **2015**, *15*, 3885–3892.

(36) Richter, P.; Plassmeyer, P. N.; Harzdorf, J.; Rüffer, T.; Lang, H.; Kalbacova, J.; Jöhrmann, N.; Schulze, S.; Hietschold, M.; Arekapudi, S. S. P. K.; Albrecht, M.; Zahn, D. R. T.; Page, C. J.; Salvan, G. High Quality Magnetic Oxide Thin Films Prepared via Aqueous Solution Processing. *Chem. Mater.* **2016**, *28*, 4917–4927.

(37) Clayton, D. R.; Lepage, D.; Plassmeyer, P. N.; Page, C. J.; Lonergan, M. C. Low-Temperature Fabrication of Lithium Aluminum Oxide Phosphate Solid Electrolyte Thin Films from Aqueous Precursors. *RSC Adv.* **2017**, *7*, 7046–7051.

(38) Woods, K. N.; Waddington, E. C.; Crump, C. A.; Bryan, E. A.; Gleckler, T. S.; Nellist, M. R.; Duell, B. A.; Nguyen, D. P.; Boettcher, S. W.; Page, C. J. Tunable High-κ $Zr_xAl_{1-x}O_y$ Thin Film Dielectrics from All-Inorganic Aqueous Precursor Solutions. *RSC Adv.* **2017**, *7*, 39147–39152.

(39) Lee, D.-H.; Chang, Y.-J.; Herman, G. S.; Chang, C.-H. A General Route to Printable High-Mobility Transparent Amorphous Oxide Semiconductors. *Adv. Mater.* **2007**, *19*, 843–847.

(40) Jeong, S.; Lee, J.-Y.; Lee, S. S.; Oh, S.-W.; Lee, H. H.; Seo, Y.-H.; Ryu, B.-H.; Choi, Y. Chemically Improved High Performance Printed Indium Gallium Zinc Oxide Thin-Film Transistors. *J. Mater. Chem.* **2011**, *21*, 17066.

(41) Huang, G.; Duan, L.; Zhao, Y.; Dong, G.; Zhang, D.; Qiu, Y. Enhanced Mobility of Solution-Processed Polycrystalline Zinc Tin Oxide Thin-Film Transistors via Direct Incorporation of Water into Precursor Solution. *Appl. Phys. Lett.* **2014**, *105*, 122105.

(42) Yu, X.; Marks, T. J.; Facchetti, A. Metal Oxides for Optoelectronic Applications. *Nat. Mater.* **2016**, *15*, 383–396.

(43) Hwang, Y. H.; Jeon, J.-H.; Bae, B.-S. Post-Humid Annealing of Low-Temperature Solution-Processed Indium Based Metal Oxide TFTs. *Electrochem. Solid-State Lett.* **2011**, *14*, H303–H305.

(44) Park, W.-T.; Son, I.; Park, H.-W.; Chung, K.-B.; Xu, Y.; Lee, T.; Noh, Y.-Y. Facile Routes to Improve Performance of Solution-Processed Amorphous Metal Oxide Thin Film Transistors by Water Vapor Annealing. *ACS Appl. Mater. Interfaces* **2015**, *7*, 13289–13294.

(45) Arii, T.; Kishi, A. The Effect of Humidity on Thermal Process of Zinc Acetate. *Thermochim. Acta* **2003**, *400*, 175–185.

(46) Arii, T.; Kishi, A. Humidity Controlled Thermal Analysis. The Effect of Humidity on Thermal Decomposition of Zinc Acetylacetonate Monohydrate. *J. Therm. Anal. Calorim.* **2006**, *83*, 253–260.

(47) Plassmeyer, P. N.; Mitchson, G.; Woods, K. N.; Johnson, D. C.; Page, C. J. Impact of Relative Humidity during Spin-Deposition of Metal Oxide Thin Films from Aqueous Solution Precursors. *Chem. Mater.* **2017**, *29*, 2921–2926.

(48) Wang, W.; Chang, I.-Y.; Zakharov, L.; Cheong, P. H.-Y.; Keszler, D. A. $[Sc_2(\mu\text{-}OH)_2(H_2O)_6(NO_3)_2](NO_3)_2$: Aqueous Synthesis and Characterization. *Inorg. Chem.* **2013**, *52*, 1807–1811.

(49) Cong, C.; Li, K.; Zhang, X. X.; Yu, T. Visualization of Arrangements of Carbon Atoms in Graphene Layers by Raman Mapping and Atomic-Resolution TEM. *Sci. Rep.* **2013**, *3*, 1195.

(50) Kim, K. H.; Akase, Z.; Suzuki, T.; Shindo, D. Charging Effects on SEM/SIM Contrast of Metal/Insulator System in Various Metallic Coating Conditions. *Mater. Trans.* **2010**, *51*, 1080–1083.

(51) Nyquist, R. A.; Putzig, C. L.; Leugers, M. A.; Kagel, R. O. *The Handbook of Infrared and Raman Spectra of Inorganic Compounds and Organic Salts*; Academic Press: San Diego, CA, USA, **1997**.

(52) Klingenberg, B.; Vannice, M. A. Influence of Pretreatment on Lanthanum Nitrate, Carbonate, and Oxide Powders. *Chem. Mater.* **1996**, *8*, 2755–2768.

(53) Małecki, A.; Małecka, B. Formation of N_2O During Thermal Decomposition of D-Metal Hydrates Nitrates. *Thermochim. Acta* **2006**, *446*, 113–116.

(54) Zhang, X.; He, H.; Gao, H.; Yu, Y. Experimental and Theoretical Studies of Surface Nitrate Species on Ag/Al_2O_3 Using DRIFTS and DFT. *Spectrochim. Acta, Part A* **2008**, *71*, 1446–1451.

(55) Anderson, J. T.; Wang, W.; Jiang, K.; Gustafsson, T.; Xu, C.; Garfunkel, E. L.; Keszler, D. A. Chemically Amplified Dehydration of Thin Oxide Films. *ACS Sustain. Chem. Eng.* **2015**, *3*, 1081–1085.

(56) De Asha, A. M.; Critchley, J. T. S.; Nix, R. M. Molecular Adsorption Characteristics of Lanthanum Oxide Surfaces: The Interaction of Water with Oxide Overlayers Grown on Cu(111). *Surf. Sci.* **1998**, *405*, 201–214.

(57) Nieminen, M.; Putkonen, M.; Niinistö, L. Formation and Stability of Lanthanum Oxide Thin Films Deposited from β-Diketonate Precursor. *Appl. Surf. Sci.* **2001**, *174*, 155–165.

(58) Cheng, J.-B.; Li, A.-D.; Shao, Q.-Y.; Ling, H.-Q.; Wu, D.; Wang, Y.; Bao, Y.-J.; Wang, M.; Liu, Z.-G.; Ming, N.-B. Growth and Characteristics of La_2O_3 Gate Dielectric Prepared by Low Pressure Metalorganic Chemical Vapor Deposition. *Appl. Surf. Sci.* **2004**, *233*, 91–98.

(59) Perkins, C. K.; Mansergh, R. H.; Park, D.-H.; Nanayakkara, C. E.; Ramos, J. C.; Decker, S. R.; Huang, Y.; Chabal, Y. J.; Keszler, D. A. Aqueous Process to Limit Hydration of Thin-Film Inorganic Oxides. *Solid State Sci.* **2016**, *61*, 106–110.

(60) Gougousi, T.; Niu, D.; Ashcraft, R. W.; Parsons, G. N. Carbonate Formation During Post-Deposition Ambient Exposure of High-*κ* Dielectrics. *Appl. Phys. Lett.* **2003**, *83*, 3543–3545.

(61) Moulder, J. F.; Stickle, W. F.; Sobol, P. E.; Bomben, K. D. *Handbook of X-Ray Photoelectron Spectroscopy: A Reference Book of Standard Spectra for Identification and Interpretation of XPS Data*; Chastain, J., Ed.; Perkin-Elmer: Eden Prairie, MN, **1992**.

(62) Sunding, M. F.; Hadidi, K.; Diplas, S.; Løvvik, O. M.; Norby, T. E.; Gunnæs, A. E. XPS Characterisation of In Situ Treated Lanthanum Oxide and Hydroxide Using Tailored Charge Referencing and Peak Fitting Procedures. *J. Electron Spectrosc. Relat. Phenom.* **2011**, *184*, 399–409.

(63) Nagao, M.; Hamano, H.; Hirata, K.; Kumashiro, R.; Kuroda, Y. Hydration Process of Rare-Earth Sesquioxides Having Different Crystal Structures. *Langmuir* **2003**, *19*, 9201–9209.

(64) Norelli, K. M.; Plassmeyer, P. N.; Woods, K. N.; Glassy, B. A.; Knutson, C. C.; Beekman, M.; Page, C. J. Influence of Composition and Processing Parameters on the Properties of Solution-Processed Aluminum Phosphate Oxide (AlPO) Thin Films. *Solid State Sci.* **2016**, *55*, 8–12.

Chapter VI

(1) Brinker, C. J.; Scherer, G. W. *Sol-Gel Science: The Physics and Chemistry of Sol-Gel Processing;* Academic Press: San Diego, CA, USA, 1990.

(2) Scherer, G. W. Recent Progress in Drying of Gels. *J. Non-Cryst. Solids* 1992, *147-148*, 363–374.

(3) Meyers, S. T.; Anderson, J. T.; Hong, D.; Hung, C. M.; Wager, J. F.; Keszler, D. A. Solution-Processed Aluminum Oxide Phosphate Thin-Film Dielectrics. *Chem. Mater.* 2007, *19*, 4023–4029.

(4) Anderson, J. T.; Munsee, C. L.; Hung, C. M.; Phung, T. M.; Herman, G. S.; Johnson, D. C.; Wager, J. F.; Keszler, D. A. Solution-Processed HafSOx and ZircSOx Inorganic Thin-Film Dielectrics and Nanolaminates. *Adv. Funct. Mater.* 2007, *17*, 2117–2124.

(5) Meyers, S. T.; Anderson, J. T.; Hung, C. M.; Thompson, J.; Wager, J. F.; Keszler, D. A. Aqueous Inorganic Inks for Low-Temperature Fabrication of ZnO TFTs. *J. Am. Chem. Soc.* 2008, *130*, 17603–17609.

(6) Jiang, K.; Zakutayev, A.; Stowers, J.; Anderson, M. D.; Tate, J.; McIntyre, D. H.; Johnson, D. C.; Keszler, D. A. Low-Temperature, Solution Processing of TiO_2 Thin Films and Fabrication of Multilayer Dielectric Optical Elements. *Solid State Sci.* 2009, *11*, 1692–1699.

(7) Cowell, E. W., III; Knutson, C. C.; Wager, J. F.; Keszler, D. A. Amorphous Metal/Oxide Nanolaminate. *ACS Appl. Mater. Interfaces* 2010, *2*, 1811–1813.

(8) Alemayehu, M.; Davis, J. E.; Jackson, M.; Lessig, B.; Smith, L.; Sumega, J. D.; Knutson, C.; Beekman, M.; Johnson, D. C.; Keszler, D. A. Tunable Dielectric Thin Films by Aqueous, Inorganic Solution-Based Processing. *Solid State Sci.* 2011, *13*, 2037–2040.

(9) Jiang, K.; Anderson, J. T.; Hoshino, K.; Li, D.; Wager, J. F.; Keszler, D. A. Low-Energy Path to Dense HfO_2 Thin Films with Aqueous Precursor. *Chem. Mater.* 2011, *23*, 945–952.

(10) Jiang, K.; Meyers, S. T.; Anderson, M. D.; Johnson, D. C.; Keszler, D. A. Functional Ultrathin Films and Nanolaminates from Aqueous Solutions. *Chem. Mater.* 2013, *25*, 210–214.

(11) Kim, K. M.; Kim, C. W.; Heo, J. S.; Na, H.; Lee, J. E.; Park, C. B.; Bae, J.-U.; Kim, C.-D.; Jun, M.; Hwang, Y. K.; Meyers, S. T.; Grenville, A.; Keszler, D. A. Competitive Device Performance of Low-Temperature and All-Solution-Processed Metal-Oxide Thin-Film Transistors. *Appl. Phys. Lett.* 2011, *99*, 2013–2016.

(12) Smith, S. W.; Wang, W.; Keszler, D. A.; Conley, J. F. Solution Based Prompt Inorganic Condensation and Atomic Layer Deposition of Al_2O_3 Films: A Side-by-Side Comparison. *J. Vac. Sci. Technol., A* 2014, *32*, 041501.

(13) Plassmeyer, P. N.; Archila, K.; Wager, J. F.; Page, C. J. Lanthanum Aluminum Oxide Thin-Film Dielectrics from Aqueous Solution. *ACS Appl. Mater. Interfaces* 2015, *7*, 1678–1684.

(14) Keszler, D. A.; Anderson, J. T.; Meyers, S. T. Oxide Dielectric Films for Active Electronics, In *Solution Processing of Inorganic Materials*. Mitzi, D. B., Ed.; John Wiley & Sons: Hoboken, NJ, USA, 2008.

(15) Nadarajah, A.; Wu, M. Z. B.; Archila, K.; Kast, M. G.; Smith, A. M.; Chiang, T. H.; Keszler, D. A.; Wager, J. F.; Boettcher, S. W. Amorphous In–Ga–Zn Oxide Semiconducting Thin Films with High Mobility from Electrochemically Generated Aqueous Nanocluster Inks. *Chem. Mater.* 2015, *27*, 5587–5596.

(16) Telecky, A.; Xie, P.; Stowers, J.; Grenville, A.; Smith, B.; Keszler, D. A. Photopatternable Inorganic Hardmask. *J. Vac. Sci. Technol., B: Microelectron. Nanom. Struct.* 2010, *28*, C6S19.

(17) Oleksak, R. P.; Ruther, R. E.; Luo, F.; Fairley, K. C.; Decker, S. R.; Stickle, W. F.; Johnson, D. W.; Garfunkel, E. L.; Herman, G. S.; Keszler, D. A. Chemical and Structural Investigation of High-Resolution Patterning with HafSOx. *ACS Appl. Mater. Interfaces* 2014, *6*, 2917–2921.

(18) Ashby, P. D.; Olynick, D. L.; Ogletree, D. F.; Naulleau, P. P. Resist Materials for Extreme Ultraviolet Lithography: Toward Low-Cost Single-Digit-Nanometer Patterning. *Adv. Mater.* 2015, *27*, 5813-5819.

(19) Vieu, C.; Carcenac, F.; Pepin, A.; Chen, Y.; Mejias, M.; Lebib, A.; Manin-Ferlazzo, L.; Couraud, L.; Launois, H. Electron Beam Lithography: Resolution Limits and Applications. *Appl. Surf. Sci.* 2000, *164*, 111–117.

(20) Dobisz, E.; Brandow, S.; Bass, R.; Mitterender, J. Effects of Molecular Properties on Nanolithography in Polymethyl Methacrylate. *J. Vac. Sci Technol. B: Microelectron. Process. Phenom.* 2000, *18*, 107–111.

(21) Hasko, D.; Yasin, S.; Mumtaz, A. Influence of Developer and Development Conditions on the Behavior of High Molecular Weight Electron Beam Resists. *J. Vac. Sci. Technol., B: Microelectron. Process. Phenom.* 2000, *18*, 3441–3444.

(22) Sidorkin, V.; Grigorescu, A.; Salemink, H.; van der Drift, E. Resist Thickness Effects on Ultra Thin HSQ Patterning Capabilities. *Microelectron. Eng.* 2009, *86*, 749–751.

(23) Grigorescu, A. E.; Hagen, C. W. Resists for Sub-20-nm Electron Beam Lithography with a Focus on HSQ: State of the Art. *Nanotechnology* 2009, *20*, 292001.

(24) Cairncross, R. A.; Schunk, P.; Chen, K. S.; Prakash, S. S.; Samuel, J.; Hurd, A.; Brinker, C. J. Pore Evolution and Solvent Transport During Drying of Gelled Sol-Gel Coatings: Predicting "Springback." *Drying Technol.* 1997, *15*, 1815–1825.

(25) Teodorescu, V. S.; Blanchin, M. G. TEM Study of the Sol-Gel Oxide Thin Films, *Microscopy: Advances in Scientific Research and Education*; FORMATEX: Madrid, Spain, 2014.

(26) Gutmann, E.; Meyer, D. C.; Levin, A. A.; Paufler, P. Density-Modulated Alumina-Based Nanometre Films Prepared by Sol-Gel Technique. *Appl. Phys. A Mater. Sci. Process.* 2005, *81*, 249–259.

(27) Morelhao, S. L.; Brito, G. E. S.; Abramof, E. Nanostructure of Sol–Gel Films by X-Ray Specular Reflectivity. *Appl. Phys. Lett.* 2002, *80*, 407–409.

(28) Loke, V. L. Y.; Riefler, N.; Mehner, A.; Prenzel, T.; Hoja, T.; Wriedt, T.; Mädler, L. Multilayer Model for Determining the Thickness and Refractive Index of Sol-Gel Coatings via Laser Ellipsometry. *Thin Solid Films* 2013, *531*, 93–98.

(29) Anderson, J. T.; Wang, W.; Jiang, K.; Gustafsson, T.; Xu, C.; Garfunkel, E. L.; Keszler, D. A. Chemically Amplified Dehydration of Thin Oxide Films. *ACS Sustain. Chem. Eng.* 2015, *3*, 1081–1085.

(30) Carnes, M. E.; Knutson, C. C.; Nadarajah, A.; Jackson, M. N.; Oliveri, A. F.; Norelli, K. M.; Crockett, B. M.; Bauers, S. R.; Moreno-Luna, H. A.; Taber, B. N.; Pacheco, D. J.; Olson, J. Z.; Brevick, K. R.; Sheehan, C. E.; Johnson, D. W.; Boettcher, S. W. Electrochemical Synthesis of Flat-$[Ga_{13-x}In_x(\mu_3\text{-}OH)_6(\mu\text{-}OH)_{18}(H_2O)_{24}(NO_3)_{15}]$ Clusters as Aqueous Precursors for Solution-Processed Semiconductors. *J. Mater. Chem. C* 2014, *2*, 8492–8496.

(31) Wang, W.; Liu, W.; Chang, I.-Y.; Wills, L. A.; Zakharov, L. N.; Boettcher, S. W.; Cheong, P. H.-Y.; Fang, C.; Keszler, D. A. Electrolytic Synthesis of Aqueous Aluminum Nanoclusters and in Situ Characterization by Femtosecond Raman Spectroscopy and Computations. *Proc. Natl. Acad. Sci. U. S. A.* 2013, *110*, 18397–18401.

(32) Ruther, R. E.; Baker, B. M.; Son, J.-H.; Casey, W. H.; Nyman, M. Hafnium Sulfate Prenucleation Clusters and the Hf_{18} Polyoxometalate Red Herring. *Inorg. Chem.* 2014, *53*, 4234–4242.

(33) Phung, T. M.; Johnson, D. C.; Antonelli, G. A. A Detailed Experimental and Analytical Study of the Thermal Expansion of Dielectric Thin Films on Si by X-Ray Reflectivity. *J. Appl. Phys.* 2006, *100*, 064317.

(34) Wormington, M.; Panaccione, C.; Matney, K. M.; Bowen, K. Characterization of Structures from X-Ray Scattering Data Using Genetic Algorithms. *Phil. Trans. R. Soc., A* 1999, *357*, 2827–2848.

(35) Giannuzzi, L. A.; Stevie, F. A., Eds. *Introduction to Focused Ion Beams: Instrumentation, Theory, Techniques, and Practice*; Springer: New York, NY, USA, 2005.

(36) Gustafsson, T.; Garfunkel, E.; Goncharova, L.; Starodub, D.; Barnes, R.; Dalpontè, M.; Bersuker, G.; Foran, B.; Lysaght, P.; Schlom, D. G.; Vaithyanathan, V.; Hong, M.; Kwo, J. R. Structure, Composition and Order at Interfaces of Crystalline Oxides and Other High-κ Materials on Silicon. *NATO Sci. Ser. II Math. Phys. Chem.* 2006, *220*, 349–360.

Chapter VII

(1) Nomura, K.; Ohta, H.; Ueda, K.; Kamiya, T.; Hirano, M.; Hosono, H. Thin-Film Transistor Fabricated in Single-Crystalline Transparent Oxide Semiconductor. *Science* **2003**, *300*, 1269–1272.

(2) Nomura, K.; Ohta, H.; Takagi, A.; Kamiya, T.; Hirano, M.; Hosono, H. Room-Temperature Fabrication of Transparent Flexible Thin-Film Transistors Using Amorphous Oxide Semiconductors. *Nature* **2004**, *432*, 488–492.

(3) Banger, K. K.; Yamashita, Y.; Mori, K.; Peterson, R. L.; Leedham, T.; Rickard, J.; Sirringhaus, H. Low-Temperature, High-Performance Solution-Processed Metal Oxide Thin-Film Transistors Formed by a "Sol–Gel on Chip" Process. *Nat. Mater.* **2011**, *10*, 45–50.

(4) Kim, Y.-H.; Heo, J.-S.; Kim, T.-H.; Park, S.; Yoon, M.-H.; Kim, J.; Oh, M. S.; Yi, G.-R.; Noh, Y.-Y.; Park, S. K. Flexible Metal-Oxide Devices Made by Room-Temperature Photochemical Activation of Sol–Gel Films. *Nature* **2012**, *489*, 128–132.

(5) Catalan, G.; Scott, J. F. Physics and Applications of Bismuth Ferrite. *Adv. Mater.* **2009**, *21*, 2463–2485.

(6) Yang, S. Y.; Seidel, J.; Byrnes, S. J.; Shafer, P.; Yang, C.-H.; Rossell, M. D.; Yu, P.; Chu, Y.-H.; Scott, J. F.; Ager III, J. W.; Martin, L. W.; Ramesh, R. Above-Bandgap Voltages from Ferroelectric Photovoltaic Devices. *Nat. Nanotechnol.* **2010**, *5*, 143–147.

(7) Alexe, M.; Hesse, D. Tip-Enhanced Photovoltaic Effects in Bismuth Ferrite. *Nat. Commun.* **2011**, *2*, 256.

(8) Tiwari, D.; Fermin, D. J.; Chaudhuri, T. K.; Ray, A. Solution Processed Bismuth Ferrite Thin Films for All-Oxide Solar Photovoltaics. *J. Phys. Chem. C* **2015**, *119*, 5872–5877.

(9) Tsuchiya, M.; Lai, B.-K.; Ramanathan, S. Scalable Nanostructured Membranes for Solid-Oxide Fuel Cells. *Nat. Nanotechnol.* **2011**, *6*, 282–286.

(10) Marichy, C.; Bechelany, M.; Pinna, N. Atomic Layer Deposition of Nanostructured Materials for Energy and Environmental Applications. *Adv. Mater.* **2012**, *24*, 1017–1032.

(11) Chao, C.-C.; Park, J. S.; Tian, X.; Shim, J. H.; Gür, T. M.; Prinz, F. B. Enhanced Oxygen Exchange on Surface-Engineered Yttria-Stabilized Zirconia. *ACS Nano* **2013**, *7*, 2186–2191.

(12) Kast, M. G.; Cochran, E. A.; Enman, L. J.; Mitchson, G.; Ditto, J.; Siefe, C.; Plassmeyer, P. N.; Greenaway, A. L.; Johnson, D. C.; Page, C. J.; Boettcher, S. W. Amorphous Mixed-Metal Oxide Thin Films from Aqueous Solution Precursors with Near-Atomic Smoothness. *J. Am. Chem. Soc.* **2016**, *138*, 16800–16808.

(13) Lee, W.-J.; Park, W.-T.; Park, S.; Sung, S.; Noh, Y.-Y.; Yoon, M.-H. Large-Scale Precise Printing of Ultrathin Sol-Gel Oxide Dielectrics for Directly Patterned Solution-Processed Metal Oxide Transistor Arrays. *Adv. Mater.* **2015**, *27*, 5043–5048.

(14) Adamopoulos, G.; Bashir, A.; Gillin, W. P.; Georgakopoulos, S.; Shkunov, M.; Baklar, M. A.; Stingelin, N.; Bradley, D. D. C.; Anthopoulos, T. D. Structural and Electrical Characterization of ZnO Films Grown by Spray Pyrolysis and Their Application in Thin-Film Transistors. *Adv. Funct. Mater.* **2011**, *21*, 525–531.

(15) Takata, R.; Neumann, A.; Weber, D.; Pham, D.-V.; Anselmann, R.; Kitamura, Y.; Kakimura, T.; Suzuki, S.; Minami, S.; Kodama, M. Scalability and Homogeneity of Slot Die-Coated Metal Oxide Semiconductor for TFTs. *J. Soc. Inf. Disp.* **2016**, *24*, 381–385.

(16) Anderson, J. T.; Munsee, C. L.; Hung, C. M.; Phung, T. M.; Herman, G. S.; Johnson, D. C.; Wager, J. F.; Keszler, D. A. Solution-Processed HafSOx and ZircSOx Inorganic Thin-Film Dielectrics and Nanolaminates. *Adv. Funct. Mater.* **2007**, *17*, 2117–2124.

(17) Meyers, S. T.; Anderson, J. T.; Hong, D.; Hung, C. M.; Wager, J. F.; Keszler, D. A. Solution-Processed Aluminum Oxide Phosphate Thin-Film Dielectrics. *Chem. Mater.* **2007**, *19*, 4023–4029.

(18) Meyers, S. T.; Anderson, J. T.; Hung, C. M.; Thompson, J.; Wager, J. F.; Keszler, D. A. Aqueous Inorganic Inks for Low-Temperature Fabrication of ZnO TFTs. *J. Am. Chem. Soc.* **2008**, *130*, 17603–17609.

(19) Jiang, K.; Anderson, J. T.; Hoshino, K.; Li, D.; Wager, J. F.; Keszler, D. A. Low-Energy Path to Dense HfO_2 Thin Films with Aqueous Precursor. *Chem. Mater.* **2011**, *23*, 945–952.

(20) Plassmeyer, P. N.; Archila, K.; Wager, J. F.; Page, C. J. Lanthanum Aluminum Oxide Thin-Film Dielectrics from Aqueous Solution. *ACS Appl. Mater. Interfaces* **2015**, *7*, 1678–1684.

(21) Nadarajah, A.; Wu, M. Z. B.; Archila, K.; Kast, M. G.; Smith, A. M.; Chiang, T. H.; Keszler, D. A.; Wager, J. F.; Boettcher, S. W. Amorphous In–Ga–Zn Oxide Semiconducting Thin Films with High Mobility from Electrochemically Generated Aqueous Nanocluster Inks. *Chem. Mater.* **2015**, *27*, 5587–5596.

(22) Fullmer, L. B.; Mansergh, R. H.; Zakharov, L. N.; Keszler, D. A.; Nyman, M. Nb_2O_5 and Ta_2O_5 Thin Films from Polyoxometalate Precursors: A Single Proton Makes a Difference. *Cryst. Growth Des.* **2015**, *15*, 3885–3892.

(23) Mansergh, R. H.; Fullmer, L. B.; Park, D. H.; Nyman, M.; Keszler, D. A. Reaction Pathway: Aqueous Hexatantalate Clusters to High-Density Tantalum Oxide Nanofilms. *Chem. Mater.* **2016**, *28*, 1553–1558.

(24) Richter, P.; Plassmeyer, P. N.; Harzdorf, J.; Rüffer, T.; Lang, H.; Kalbacova, J.; Jöhrmann, N.; Schulze, S.; Hietschold, M.; Arekapudi, S. S. P. K.; Albrecht, M.; Zahn, D. R. T.; Page, C. J.; Salvan, G. High Quality Magnetic Oxide Thin Films Prepared via Aqueous Solution Processing. *Chem. Mater.* **2016**, *28*, 4917–4927.

(25) Clayton, D. R.; Lepage, D.; Plassmeyer, P. N.; Page, C. J.; Lonergan, M. C. Low-Temperature Fabrication of Lithium Aluminum Oxide Phosphate Solid Electrolyte Thin Films from Aqueous Precursors. *RSC Adv.* **2017**, *7*, 7046–7051.

(26) Woods, K. N.; Waddington, E. C.; Crump, C. A.; Bryan, E. A.; Gleckler, T. S.; Nellist, M. R.; Duell, B. A.; Nguyen, D. P.; Boettcher, S. W.; Page, C. J. Tunable High-κ $Zr_xAl_{1-x}O_y$ Thin Film Dielectrics from All-Inorganic Aqueous Precursor Solutions. *RSC Adv.* **2017**, *7*, 39147–39152.

(27) Kim, K. M.; Kim, C. W.; Heo, J. S.; Na, H.; Lee, J. E.; Park, C. B.; Bae, J.-U.; Kim, C.-D.; Jun, M.; Hwang, Y. K.; Meyers, S. T.; Grenville, A.; Keszler, D. A. Competitive Device Performance of Low-Temperature and All-Solution-Processed Metal-Oxide Thin-Film Transistors. *Appl. Phys. Lett.* **2011**, *99*, 242109.

(28) Smith, S. W.; Wang, W.; Keszler, D. A.; Conley, J. F. Solution Based Prompt Inorganic Condensation and Atomic Layer Deposition of Al_2O_3 Films: A Side-by-Side Comparison. *J. Vac. Sci. Technol., A* **2014**, *32*, 41501.

(29) Morelhão, S. L.; Brito, G. E. S.; Abramof, E. Nanostructure of Sol–Gel Films by X-Ray Specular Reflectivity. *Appl. Phys. Lett.* **2002**, *80*, 407–409.

(30) Gutmann, E.; Meyer, D. C.; Levin, A. A.; Paufler, P. Density-Modulated Alumina-Based Nanometre Films Prepared by Sol-Gel Technique. *Appl. Phys. A Mater. Sci. Process.* **2005**, *81*, 249–259.

(31) Loke, V. L. Y.; Riefler, N.; Mehner, A.; Prenzel, T.; Hoja, T.; Wriedt, T.; Mädler, L. Multilayer Model for Determining the Thickness and Refractive Index of Sol-Gel Coatings via Laser Ellipsometry. *Thin Solid Films* **2013**, *531*, 93–98.

(32) Teodorescu, V. S.; Blanchin, M.-G. In *Microscopy: Advances in Scientific Research and Education*; Méndez-Vilas, A., Ed.; FORMATEX: Badajoz, Spain, **2014**.

(33) Anderson, J. T.; Wang, W.; Jiang, K.; Gustafsson, T.; Xu, C.; Garfunkel, E. L.; Keszler, D. A. Chemically Amplified Dehydration of Thin Oxide Films. *ACS Sustain. Chem. Eng.* **2015**, *3*, 1081–1085.

(34) Fairley, K. C.; Merrill, D. R.; Woods, K. N.; Ditto, J.; Xu, C.; Oleksak, R. P.; Gustafsson, T.; Johnson, D. W.; Garfunkel, E. L.; Herman, G. S.; Johnson, D. C.; Page, C. J. Non-Uniform Composition Profiles in Inorganic Thin Films from Aqueous Solutions. *ACS Appl. Mater. Interfaces* **2016**, *8*, 667–672.

(35) Woods, K. N.; Chiang, T.-H.; Plassmeyer, P. N.; Kast, M. G.; Lygo, A. C.; Grealish, A. K.; Boettcher, S. W.; Page, C. J. High-κ Lanthanum Zirconium Oxide Thin Film Dielectrics from Aqueous Solution Precursors. *ACS Appl. Mater. Interfaces* **2017**, *9*, 10897–10903.

(36) Mitchson, G.; Ditto, J.; Woods, K. N.; Westover, R.; Page, C. J.; Johnson, D. C. Application of HAADF STEM Image Analysis to Structure Determination in Rotationally Disordered and Amorphous Multilayered Films. *Semicond. Sci. Technol.* **2016**, *31*, 84003.

(37) Gaskell, J. M.; Jones, A. C.; Chalker, P. R.; Werner, M.; Aspinall, H. C.; Taylor, S.; Taechakumput, P.; Heys, P. N. Deposition of Lanthanum Zirconium Oxide High-κ Films by Liquid Injection ALD and MOCVD. *Chem. Vap. Depos.* **2007**, *13*, 684–690.

(38) Gaskell, J. M.; Jones, A. C.; Aspinall, H. C.; Taylor, S.; Taechakumput, P.; Chalker, P. R.; Heys, P. N.; Odedra, R. Deposition of Lanthanum Zirconium Oxide High-κ Films by Liquid Injection Atomic Layer Deposition. *Appl. Phys. Lett.* **2007**, *91*, 112912.

(39) Alessandri, M.; Del Vitto, A.; Piagge, R.; Sebastiani, A.; Scozzari, C.; Wiemer, C.; Lamagna, L.; Perego, M.; Ghidini, G.; Fanciulli, M. Rare Earth-Based High-κ Materials for Non-Volatile Memory Applications. *Microelectron. Eng.* **2010**, *87*, 290–293.

(40) Tue, P. T.; Li, J.; Miyasako, T.; Inoue, S.; Shimoda, T. Low-Temperature All-Solution-Derived Amorphous Oxide Thin-Film Transistors. *IEEE Electron Device Lett.* **2013**, *34*, 1536–1538.

(41) Tue, P. T.; Miyasako, T.; Li, J.; Tu, H. T. C.; Inoue, S.; Tokumitsu, E.; Shimoda, T. High-Performance Solution-Processed ZrInZnO Thin-Film Transistors. *IEEE Trans. Electron Devices* **2013**, *60*, 320–326.

(42) Je, S. Y.; Son, B.-G.; Kim, H.-G.; Park, M.-Y.; Do, L.-M.; Choi, R.; Jeong, J. K. Solution-Processable $LaZrO_x/SiO_2$ Gate Dielectric at Low Temperature of 180 °C for High-Performance Metal Oxide Field-Effect Transistors. *ACS Appl. Mater. Interfaces* **2014**, *6*, 18693–18703.

(43) Li, J.; Zhu, P.; Hirose, D.; Kohara, S.; Shimoda, T. Hybrid Cluster Precursors of the LaZrO Insulator for Transistors: Properties of High-Temperature-Processed Films and Structures of Solutions, Gels, and Solids. *Sci. Rep.* **2016**, *6*, 29682.

(44) Knoth, K.; Hühne, R.; Oswald, S.; Schultz, L.; Holzapfel, B. Highly Textured $La_2Zr_2O_7$ Buffer Layers for YBCO-Coated Conductors Prepared by Chemical Solution Deposition. *Supercond. Sci. Technol.* **2005**, *18*, 334–339.

(45) Molina, L.; Knoth, K.; Engel, S.; Holzapfel, B.; Eibl, O. Chemically Deposited $La_2Zr_2O_7$ Buffer Layers for YBCO-Coated Conductors: Film Growth and Microstructure. *Supercond. Sci. Technol.* **2006**, *19*, 1200–1208.

(46) Paranthaman, M. P.; Sathyamurthy, S.; Bhuiyan, M. S.; Goyal, A.; Kodenkandath, T.; Li, X.; Zhang, W.; Thieme, C. L. H.; Schoop, U.; Verebelyi, D. T.; Rupich, M. W. Improved YBCO Coated Conductors Using Alternate Buffer Architectures. *IEEE Trans. Appl. Supercond.* **2005**, *15*, 2632–2634.

(47) Sathyamurthy, S.; Paranthaman, M.; Aytug, T.; Kang, B. W.; Martin, P. M.; Goyal, A.; Kroeger, D. M.; Christen, D. K. Chemical Solution Deposition of Lanthanum Zirconate Buffer Layers on Biaxially Textured Ni–1.7% Fe–3% W Alloy Substrates for Coated-Conductor Fabrication. *J. Mater. Res.* **2002**, *17*, 1543–1549.

(48) Sathyamurthy, S.; Paranthaman, M.; Heatherly, L.; Martin, P. M.; Specht, E. D.; Goyal, A.; Kodenkandath, T.; Li, X.; Rupich, M. W. Solution-Processed Lanthanum Zirconium Oxide as a Barrier Layer for High I_c-Coated Conductors. *J. Mater. Res.* **2006**, *21*, 910–914.

(49) Chen, H. S.; Kumar, R. V.; Glowacki, B. A. Chemical Solution Deposited Lanthanum Zirconium Oxide Thin Films: Synthesis and Chemistry. *Mater. Chem. Phys.* **2010**, *122*, 305–310.

(50) Jin, H.; Huang, D.; Gao, Q.; Li, L.; Wang, N.; Wang, Y.; Hou, S. Synthesis of Lanthanum Zirconium Oxide Nanomaterials through Composite-Hydroxide-Mediated Approach. *Mater. Res. Bull.* **2012**, *47*, 51–53.

(51) Wormington, M.; Panaccione, C.; Matney, K. M.; Bowen, D. K. Characterization of Structures from X-Ray Scattering Data Using Genetic Algorithms. *Philos. Trans. R. Soc., A* **1999**, *357*, 2827–2848.

(52) Perez, F.; Granger, B. E. IPython: A System for Interactive Scientific Computing. *Comput. Sci. Eng.* **2007**, *9*, 21–29.

(53) de la Peña, F.; Burdet, P.; Ostasevicius, T.; Sarahan, M.; Walls, M.; Sarahan, M.; Nord, M.; Fauske, V. T.; Taillon, J.; Zzucco, S.; Eljarrat, A.; Mazzucco, S.; Donval, G.; Zagonel, L. F.; Walls, M.; Iygr. *Hyperspy*, version 0.8.2, **2015**.

(54) Parish, C. M.; Brewer, L. N. Multivariate Statistics Applications in Phase Analysis of STEM-EDS Spectrum Images. *Ultramicroscopy* **2010**, *110*, 134–143.

(55) Phung, T. M.; Jensen, J. M.; Johnson, D. C.; Donovan, J. J.; McBurnett, B. G. Determination of the Composition of Ultra-Thin Ni-Si Films on Si: Constrained Modeling of Electron Probe Microanalysis and X-Ray Reflectivity Data. *X-Ray Spectrom.* **2008**, *37*, 608–614.

(56) Fenter, P.; Gustafsson, T. Structural Analysis of the Pt(110)-(1×2) Surface Using Medium-Energy Ion Scattering. *Phys. Rev. B* **1988**, *38*, 10197–10204.

(57) Norelli, K. M.; Plassmeyer, P. N.; Woods, K. N.; Glassy, B. A.; Knutson, C. C.; Beekman, M.; Page, C. J. Influence of Composition and Processing Parameters on the Properties of Solution-Processed Aluminum Phosphate Oxide (AlPO) Thin Films. *Solid State Sci.* **2016**, *55*, 8–12.

(58) Jiang, K.; Meyers, S. T.; Anderson, M. D.; Johnson, D. C.; Keszler, D. A. Functional Ultrathin Films and Nanolaminates from Aqueous Solutions. *Chem. Mater.* **2013**, *25*, 210–214.

(59) Plassmeyer, P. N.; Mitchson, G.; Woods, K. N.; Johnson, D. C.; Page, C. J. Impact of Relative Humidity during Spin-Deposition of Metal Oxide Thin Films from Aqueous Solution Precursors. *Chem. Mater.* **2017**, *29*, 2921–2926.

(60) Stevels, J. M. *Progress in the Theory of the Physical Properties of Glass*; Elsevier: New York, **1948**.

(61) Gobichon, A.-E.; Auffrédic, J.-P.; Louër, D. Thermal Decomposition of Neutral and Basic Lanthanum Nitrates Studied with Temperature-Dependent Powder Diffraction and Thermogravimetric Analysis. *Solid State Ionics* **1997**, *93*, 51–64.

(62) Gougousi, T.; Niu, D.; Ashcraft, R. W.; Parsons, G. N. Carbonate Formation during Post-Deposition Ambient Exposure of High-κ Dielectrics. *Appl. Phys. Lett.* **2003**, *83*, 3543–3545.

Appendix B

(1) Fairley, K. C.; Merrill, D. R.; Woods, K. N.; Ditto, J.; Xu, C.; Oleksak, R. P.; Gustafsson, T.; Johnson, D. W.; Garfunkel, E. L.; Herman, G. S.; Johnson, D. C.; Page, C. J. Non-Uniform Composition Profiles in Inorganic Thin Films from Aqueous Solutions. *ACS Appl. Mater. Interfaces* **2016**, *8*, 667–672.

(2) Woods, K. N.; Chiang, T.-H.; Plassmeyer, P. N.; Kast, M. G.; Lygo, A. C.; Grealish, A. K.; Boettcher, S. W.; Page, C. J. High-κ Lanthanum Zirconium Oxide Thin Film Dielectrics from Aqueous Solution Precursors. *ACS Appl. Mater. Interfaces* **2017**, *9*, 10897–10903.

(3) Plassmeyer, P. N.; Mitchson, G.; Woods, K. N.; Johnson, D. C.; Page, C. J. Impact of Relative Humidity during Spin-Deposition of Metal Oxide Thin Films from Aqueous Solution Precursors. *Chem. Mater.* **2017**, *29*, 2921–2926.

Appendix C

(1) Nyquist, R. A.; Putzig, C. L.; Leugers, M. A.; Kagel, R. O. *The Handbook of Infrared and Raman Spectra of Inorganic Compounds and Organic Salts*; Academic Press: San Diego, CA, USA, **1997**.

(2) Rao, N. S.; Rao, M. V. B. Structural and Optical Investigation of ZnO Nanopowders Synthesized from Zinc Chloride and Zinc Nitrate. *Am. J. Mater. Sci.* **2015**, *5*, 66–68.

(3) Park, J. H.; Kim, K.; Yoo, Y. B.; Park, S. Y.; Lim, K.-H.; Lee, K. H.; Baik, H. K.; Kim, Y. S. Water Adsorption Effects of Nitrate Ion Coordinated Al_2O_3 Dielectric for High Performance Metal-Oxide Thin-Film Transistor. *J. Mater. Chem. C* **2013**, *1*, 7166–7174.

(4) Klingenberg, B.; Vannice, M. A. Influence of Pretreatment on Lanthanum Nitrate, Carbonate, and Oxide Powders. *Chem. Mater.* **1996**, *8*, 2755–2768.

(5) Moulder, J. F.; Stickle, W. F.; Sobol, P. E.; Bomben, K. D. *Handbook of X-Ray Photoelectron Spectroscopy: A Reference Book of Standard Spectra for Identification and Interpretation of XPS Data*; Chastain, J., Ed.; Perkin-Elmer: Eden Prairie, MN, **1992**.

(6) Dementjev, A. P.; Ivanova, O. P.; Vasilyev, L. A.; Naumkin, A. V.; Nemirovsky, D. M.; Shalaev, D. Y. Altered Layer as Sensitive Initial Chemical State Indicator*. *J. Vac. Sci. Technol., A* **1994**, *12*, 423–427.

(7) Gunasekaran, N.; Rajadurai, S.; Carberry, J. J.; Bakshi, N.; Alcock, C. B. Surface Characterization and Catalytic Properties of $La_{1-x}A_xMO_3$ Perovskite Type Oxides. Part I. Studies on $La_{0.95}Ba_{0.05}MO_3$ (M=Mn, Fe or Co) Oxides. *Solid State Ionics* **1994**, *73*, 289–295.

(8) Howng, W.-Y.; Thorn, R. J. Investigation of the Electronic Structure of $La_{1-x}(M^{2+})_xCrO_3$, Cr_2O_3 and La_2O_3 by X-Ray Photoelectron Spectroscopy. *J. Phys. Chem. Solids* **1980**, *41*, 75–81.

(9) Majumdar, D.; Chatterjee, D. X-Ray Photoelectron Spectroscopic Studies on Yttria, Zirconia, and Yttria-Stabilized Zirconia. *J. Appl. Phys.* **1991**, *70*, 988–992.